https://doi.org/10.15388/vu.thesis.691
https://orcid.org/0009-0000-5999-6429

VILNIUS UNIVERSITY
CENTER FOR PHYSICAL SCIENCES AND TECHNOLOGY

Anastasija Afonina

Synthesis and Characterisation of Magnesium Whitlockite Powders *via* a Low-Temperature Dissolution-Precipitation Process

DOCTORAL DISSERTATION

Natural Sciences,
Chemistry (N 003)

VILNIUS 2024

The dissertation was prepared between 2018 and 2024 while studying at Vilnius University.

Academic supervisor – Assoc. Prof. Dr. Inga Grigoravičiūtė (Vilnius University, Natural Sciences, Chemistry – N 003).

This doctoral dissertation will be defended in a public meeting of the Dissertation Defence Panel:

Chairman – **Assoc. Prof. Dr. Justina Gaidukevič** (Vilnius University, Natural Sciences, Chemistry – N 003).
Members:
Dr. Olga Kizinievič (Vilnius Tech, Technological Sciences, Materials Engineering – T 008),
Dr. Germanas Peleckis (University of Wollongong, Australian Institute for Innovative Materials, Natural sciences, Chemistry – N 003),
Prof. Habil. Dr. Rimantas Ramanauskas (Center for Physical Sciences and Technology, Natural sciences, Chemistry – N 003),
Prof. Dr. Ramūnas Skaudžius (Vilnius University, Natural Sciences, Chemistry – N 003).

The dissertation shall be defended at a public meeting of the Dissertation Defence Panel at 14 pm on 22nd of November 2024 in Inorganic Chemistry auditorium (141) of the Institute of Chemistry, Faculty of Chemistry and Geoscience, Vilnius University.
Address: Naugarduko str. 24, LT-03225 Vilnius, Lithuania
Tel. +370 5 2193105; e-mail: info@chgf.vu.lt

The text of this dissertation can be accessed at the libraries of Vilnius University and Centre for Physical Sciences and Technology, as well as on the website of Vilnius University:
www.vu.lt/lt/naujienos/ivykiu-kalendorius

https://doi.org/10.15388/vu.thesis.691
https://orcid.org/0009-0000-5999-6429

VILNIAUS UNIVERSITETAS
FIZINIŲ IR TECHNOLOGIJOS MOKSLŲ CENTRAS

Anastasija Afonina

Žematemperatūrė magnio vitlokito miltelių tirpinimo-nusodinimo metodu sintezė ir apibūdinimas

DAKTARO DISERTACIJA

Gamtos mokslai,
Chemija (N 003)

VILNIUS 2024

Disertacija rengta 2018–2024 metais Vilniaus universitete.

Mokslinė vadovė – **Doc. dr. Inga Grigoravičiūtė** (Vilniaus universitetas, gamtos mokslai, chemija – N 003).

Gynimo taryba:
Pirmininkė – **Doc. dr. Justina Gaidukevič** (Vilniaus universitetas, gamtos mokslai, chemija – N 003).
Nariai:
Dr. Olga Kizinievič (Vilnius Tech, technologijos mokslai, medžiagų inžinerija – T 008),
Dr. Germanas Peleckis (Vollongongo universitetas, Australijos inovatyviųjų medžiagų institutas, gamtos mokslai, chemija – N 003),
Prof. habil. dr. Rimantas Ramanauskas (Fizinių ir technologijos mokslų centras, gamtos mokslai, chemija – N 003),
Prof. dr. Ramūnas Skaudžius (Vilniaus universitetas, gamtos mokslai, chemija – N 003).

Disertacija ginama viešame Gynimo tarybos posėdyje 2024 m. lapkričio mėn. 22 d. 14 val. Vilniaus universiteto Chemijos instituto Chemijos ir Geomokslų fakulteto Neorganinės chemijos auditorijoje, 141. Adresas: Naugarduko g. 24, LT-03225, Vilnius, Lietuva, tel. +370 5 2193105; el. pastas info@chgf.vu.lt.

Disertaciją galima peržiūrėti Vilniaus universiteto bei Fizinių ir technologijos mokslų centro bibliotekose ir VU interneto svetainėje adresu: *www.vu.lt/lt/naujienos/ivykiu-kalendorius*

TABLE OF CONTENTS

INTRODUCTION

Bones are constantly renewed during the lifetime of mammals [1]. It is a natural 3D organic-inorganic nanocomposite composed of collagen fibrils and low crystalline nanoparticles of inorganic materials [2–4]. The primary inorganic component in mineralized vertebrate osseous tissue consists mainly of calcium deficient hydroxyapatite ($Ca_{10-x}(HPO_4)_x(PO_4)_{6-x}(OH)_{2-x}$), partially enriched by substitutional CO_3^{2-}, Mg^{2+}, Sr^{2+}, F^-, HPO_4^{2-} ions [5,6]. Although natural bone has a significant capacity for self-healing, there are diseases and conditions, such as osteoporosis, tumours, injuries, and other factors, that can cause bone defects that exceed the natural remodelling capacity of the body [7]. For such patients, external intervention treatment is required to help bone healing and/or restoration. As an example, artificial implants with a structural and chemical composition similar to native osseous tissue could be promising in the restoration, replacement, support, or enrichment of the functions of hard tissues in mammals [8,9]. Nowadays, these artificial substitutes are prepared in a wide range of forms: powders, granules, dense or porous scaffolds, and bioactive coatings on metallic or polymeric implants. They have been used clinically as artificial bone substitutes due to their ability to promote the formation of new bone by gradually replacing implanted material within the bone defect [10]. Calcium phosphates (CPs) are known to be excellent grafts, considering their excellent biocompatibility to the human body, controllable biodegradability, osteoconductivity, bioactivity, and osseointegrativity [11]. Consequently, there is a significant demand for synthetic CPs in the field of biomedical care [12,13].

The biological behaviour (biodegradation rate, osteoconductivity, bioactivity) and mechanical properties of the CP ceramic depend greatly on the synthesis method, as it affects the phase composition, purity, crystallinity, size, and morphology of the particles obtained and therefore influences the biomedical performance of artificial implants [14,15]. Therefore, the selection of the synthesis method is very important in the preparation of materials used for biomedical applications [10]. Numerous preparative techniques have been discovered to synthetize substitute CP materials at high temperatures [16,17]. However, the resulting ceramics have an extremely high crystallinity, which deviates significantly from natural bone [18]. Moreover, some thermally unstable CP phases cannot be synthesized by conventional high temperature methods [19]. Biomaterials obtained under the low temperature regime could exhibit greater tissue compatibility than conventional bioceramics [20,21]. Wet-chemical synthesis methods, such as sol-gel, hydrothermal, microwave-

assisted, microemulsion, and co-precipitation, in which the precursor salts are in solution, allow for a homogeneous distribution of the starting components and therefore allow the synthesis of the end products at relatively low temperature [16]. A low-temperature synthesis method used to fabricate poorly crystalline CP materials through a phase transformation based on a dissolution-precipitation reaction is one of the techniques used to prepare bioceramics with physicochemical properties similar to those of bone apatite [22,23]. It is a technique used to create new materials by dissolving a precursor compounds and subsequently precipitating it in the desired composition and form. The dissolution-precipitation reaction is a highly reproducible, low-cost, and environmentally friendly synthesis method. It is possible to rigorously control the entire synthesis process and, if necessary, tune the desired physical and chemical properties of the materials obtained [22-24].

Magnesium whitlockite (Mg-WH: $Ca_{18}Mg_2(HPO_4)_2(PO_4)_{12}$) is a calcium orthophosphate in which magnesium ions partially substitute calcium ions. The ability of Mg-WH to precipitate in solutions containing magnesium, calcium, and phosphorus at a temperature that aligns with physiological conditions suggests its potential involvement in various biological and pathological processes [25]. Mg-WH has been described as one of the main inorganic components of mammalian hard tissue (along with the aforementioned CP apatite structure); however, this has been recently questioned [25,26]. In general, magnesium ions are essential elements with various functions in the human body. It is involved in muscle function, nervous system health, bone health, and numerous enzymatic processes [27]. Magnesium ions were found to promote bone formation while preventing activity of osteoclasts [28]. Magnesium-substituted CPs have been shown to increase the degradation rate of bioceramics, making them more suitable for applications requiring temporary support or gradual replacement by newly formed bone tissue [29]. Synthetic Mg-WH used as bone substitute material has been shown to promote bone formation, stimulate osteogenic differentiation, and prohibit osteoclast activity under physiological conditions [28]. Although the exact abundance and distribution of Mg-WH in bone are still subject to research and debate, interest in this magnesium-containing CP is still being observed.

WH structure compounds contain hydrogen in the form of HPO_4^{2-} group in their crystal structure. Dry synthesis methods require relatively high temperatures, which would cause decomposition of the phase; therefore, low-temperature wet synthesis methods are employed to prepare this material. WH structure compounds have been synthesized using hydrothermal [30-32],

precipitation [24,33–35], solvathermal [36] and dissolution-precipitation [37] methods. It was demonstrated that pH, temperature, heating time, aging time, and the rate at which starting materials are added to the reaction simultaneously affect the precipitation of the pure Mg-WH phase. A subtle change in any of these parameters could lead to the formation of undesired stable secondary CP phase [37].

The aim of the research is to investigate the formation of Mg-WH from brushite (dicalcium phosphate dihydrate, $CaHPO_4 \cdot 2H_2O$, DCPD) and gypsum (calcium sulphate dihydrate, $CaSO_4 \cdot 2H_2O$) as starting materials *via* a low temperature dissolution-precipitation process, to explore Mg-WH phase formation and to control the synthesis conditions to influence the chemical composition, crystallinity and morphology of the resulting powder for potential applications in bone tissue regeneration.

The tasks of the research are the following:

- to determine Mg-WH phase purity, Ca/Mg molar ratio, crystallographic parameters, functional groups, and morphology under altered nominal Ca to Mg molar ratios;
- to investigate the formation of Mg-WH in an aqueous medium from gypsum in the presence of magnesium and phosphate ions under static and rotating conditions.

KEY DEFENESE STATEMENTS

1. The chemical composition, morphology and particle size of Mg-WH can be adjusted by varying the Ca/Mg molar ratio in the initial synthesis solution. Single-phase samples can be synthesised with a nominal Ca/Mg ratio from 4 to 12 *via* the dissolution-precipitation method from brushite. As the nominal Ca/Mg molar ratio increases, the magnesium content in the WH structure decreases, while the lattice parameters *a* and *c* of the synthesised compounds increase.
2. The formation of Mg-WH powder during dissolution-precipitation synthesis at 80 °C under static and rotating conditions from an initial powder of gypsum as a result of the formation of several intermediate products occurs within 12 h. The synthesis under rotating conditions favours the formation of smaller Mg-WH crystals with respect to the sample synthesized under static conditions. Following a synthesis period of up to 24 hours, the samples exhibit some alterations in their lattice parameters, magnesium occupancy, and lattice volume. The synthesis conditions (static *vs*. rotating) influences the structural parameters, as well as the crystallite size and crystallinity of the Mg-WH samples.

LIST OF ABBREVIATIONS

ACP	Amorphous calcium phosphate
β-TCP	β-tricalcium phosphate
BCPs	Biphasic calcium phosphates
CDHA	Calcium-deficient hydroxyapatite
CO_3Ap	Carbonate apatite
CO_3Ap-DP	Carbonate apatite fabricated by dissolution-precipitation method
CP	Calcium phosphate
CPC	Calcium phosphate cement
CSH	Calcium sulphate hemihydrate
CS	Chitosan
DCPD	Dicalcium phosphate dihydrate
DCPA	Dicalcium phosphate anhydrous
DSC	Differential scanning calorimetry
FBP	Fructose 1,6-bisphosphate
FT-IR	Fourier transform infrared spectroscopy
HAp	Hydroxyapatite
Hb	Haemoglobin
ICDD	International Centre for Diffraction Data
ICP-OES	Inductively coupled plasma optical emission spectrometry
MP	Dimagnesium phosphate
Mg-WH	Magnesium whitlockite
OCP	Octacalcium phosphate
PEG	Polyethylene glycol
PGA	Polyglycolic acid
PLA	Polylactic acid
PLGA	Poly(lactic-co-glycolic) acid
SEM	Scanning electron microscopy
TCP	Tricalcium phosphate
TEM	Transmission electron microscopy
WH	Whitlockite
WHHMs	Magnesium whitlockite hollow microspheres
XRD	X-ray diffraction

1. LITERATURE OVERVIEW

1.1. Bones

Bone, an extraordinary tissue, plays a vital role in the human body. It serves as the structural framework, providing support, protection, and mobility while participating in various physiological processes. At a macroscopic level, bone appears as a dense and rigid structure. Bone is classified into two main types: compact (cortical) bone and cancellous (trabecular or spongy) bone (see Figure 1) [38]. Compact bone forms the dense outer layer of bones and provides strength and protection. Cancellous bone, found in the inner regions, consists of a network of interconnected trabeculae that create a porous structure. The bone matrix consists of an inorganic (60 %) and an organic (40 %) component that provides mechanical support and plays an essential role in bone homeostasis. The hardness and strength of bone can be attributed to the presence of inorganic minerals, primarily calcium phosphates, which form a crystalline mineralized matrix (see Figure 1) [39,40]. This mineralized matrix is interspersed with collagen fibers, offering resilience and flexibility to withstand mechanical stress and impacts [40].

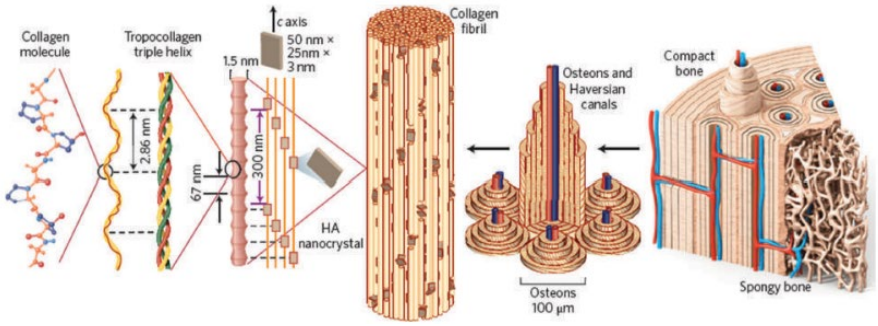

Figure 1. Scheme showing the hierarchical organization of bone from the macro- to the nanoscale [38].

The organic matrix gives bone its tensile strength. Collagen, particularly type I, comprises the majority (about 90 %) of the organic matrix and provides bone with its tensile strength. The remaining 10 % of the organic matrix consists of bone-specific proteoglycans, non-collagenous matrix proteins, growth factors, and cytokines, all of which contribute to bone's intricate composition [40]. The basic unit of bone collagen fiber combined with noncollagenous proteins and water, create a highly organized and hierarchical structure within the bone matrix [40].

Bone serves as a reservoir for 99 % of body calcium, 85 % of body phosphate, and 40–60 % of total sodium and potassium [40]. The inorganic part of the hard tissue consists of a significant amount of sodium, potassium, pyrophosphate, magnesium, carbonate, fluoride, chloride and others (see Table 1) [41].

Table 1. Typical compositional values of the inorganic phase of adult human calcified tissues [41].

Composition	**Enamel**	**Dentin**	**Bone**
Calcium [wt. %]	36.5	35.1	34.8
Phosphorus [wt. %]	17.7	16.9	15.2
Sodium [wt. %]	0.50	0.60	0.90
Magnesium [wt. %]	0.44	1.3	0.72
Potassium [wt. %]	0.080	0.050	0.030
Carbonate [wt. %]	3.5	5.6	7.4
Fluoride [wt. %]	0.010	0.060	0.030
Chloride [wt. %]	0.30	0.010	0.13
Pyrophosphate [wt. %]	0.022	0.10	0.070
Total inorganic [wt. %]	97	70	65
Total organic [wt. %]	1.5	20	25
Water [wt. %]	1.5	10	10

Moving to the microscopic level, bones reveal a hierarchical structure that is composed of specialized cells and distinct components. At the microscopic scale, bones are composed of units known as osteons or Haversian systems (see Figure 1). Each osteon consists of concentric layers of mineralized bone matrix called lamellae, which surround a central canal containing blood vessels and nerves. The Haversian systems, or osteons, are arranged parallel to the long axis of the bone, allowing for effective load-bearing capabilities and resistance to mechanical stress, therefore are responsible for the strength and integrity of bone tissue (see Figure 1) [40]. According to its structure bone is classified into woven and lamellar. Whereas lamellar bones are divided into cortical and cancellous. The classification of bones helps us understand the structural and functional diversity of bone tissue. This knowledge is crucial for various fields, including orthopedics, biomechanics, and bone research, as it allows for a better understanding of bone development, healing processes, and the mechanical properties of different bone types.

Skeletal animals are classified as invertebrates or vertebrates. The skeleton of invertebrates consists of calcium carbonate ($CaCO_3$) and may come from elements found in marine waters. On the contrary, vertebrates, including humans, have mainly a carbonate apatite consisting of a skeleton [CO_3-Ap: $Ca_{10-a}(PO_4)_{6-b}(CO_3)_c$], which is responsible for the strength of bone compression [42-45]. Recent advancements in technology and scientific research have deepened our understanding of the complex structure and composition of vertebrates' bone tissue [43,45]. Advanced microscopic analysis has uncovered additional components within the inorganic part of bone, namely, magnesium-containing CP with whitlockite crystalline structure [35,46]. However, the composition of inorganic components in bone tissue has been a subject of debate among researchers, leading to varying opinions on their constituents. While CO_3-Ap is widely accepted as the primary inorganic phase in human bone, the role and significance of Mg-WH in bone composition are still under discussion [47]. Some studies propose that Mg-WH is a major inorganic component of bone tissue, comprising approximately 25 % to 35 % by weight of the hard tissue in human bones [25]. However, contrasting opinions propose that Mg-WH is primarily associated with calcifications rather than being an essential component of bone tissue [25]. According to these perspectives, Mg-WH may form as a result of pathological processes or mineralization.

1.1.1. Bone remodeling

Bone cells are specialized cells that are responsible for the formation, maintenance, and remodeling of bone tissue. They play crucial roles in bone development, repair, and overall bone health. There are several types of bone cells, each with distinct functions [48,49]. *Osteoblasts* are bone-forming cells. They are responsible for synthesizing and depositing the organic matrix of bone tissue, creating the framework for mineral deposition. *Osteocytes* are mature osteoblasts that have become embedded within the mineralized bone matrix. They are the most abundant cells in mature bone tissue, make up 90 % of mature skeleton calls. Osteocytes also play a critical role in maintaining bone homeostasis by sensing mechanical strain and orchestrating bone remodelling in response to mechanical and biochemical signals. *Osteoclasts* are responsible for bone resorption, which is the process of breaking down and removing old or damaged bone tissue. Osteoclasts secrete enzymes and acids that dissolve the mineralized matrix to release calcium and phosphate ions into

the bloodstream. This process is important for bone remodelling, calcium homeostasis, and the repair of microdamage in bone tissue [40].

Together with bone cells, magnesium plays an equally important role in the integration and regeneration of bone tissues among all inorganic species [50]. It plays an important role in maintaining bone nucleation kinetics [51], metabolism, formation and crystallization [52]. Compared to calcium, the affinity of magnesium allows him to improve the integration of bone-implant [53,54]. In the natural mineralization process, magnesium assists the transportation of calcium ions to the active areas and plays a role in calcification. In synthetic systems, magnesium-containing CP produces a layer of hydroxyapatite (HAp) on the surface similar to the natural bone healing process [55]. These properties encouraged scientists to focus on incorporating magnesium into different CP systems [56].

Bone is a dynamic and metabolically active tissue, that undergoes remodelling throughout life. Continuous cycle of resorption and formation helps maintain bone integrity, repair micro-damage, and adapt to changing mechanical demands or physiological needs. Different events, such as development, ageing, and function, play a critical role in bone remodelling and metabolism. In 1990 Frost defined this phenomenon as bone remodelling [57]. Bone remodelling involves bone cells. The remodelling cycle consists of three phases: resorption, reversal, and formation (see Figure 2).

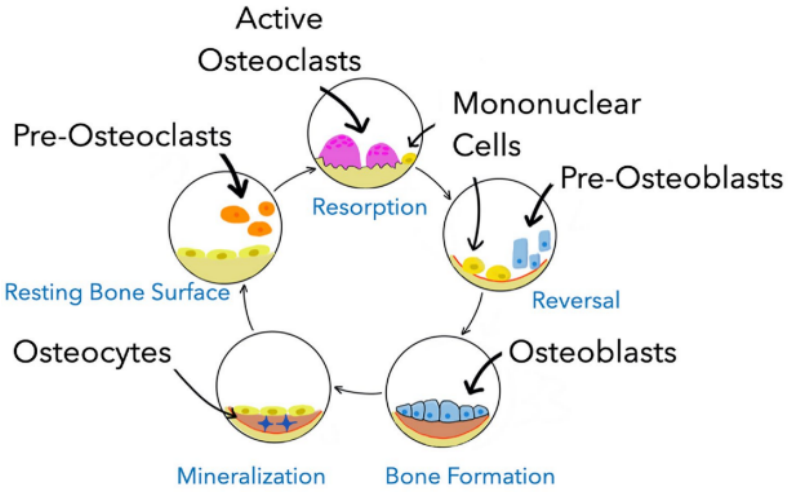

Figure 2. Stages of the bone remodeling cycle [58].

During resorption, partially differentiated pre-osteoclasts migrate to the bone surface and form multinucleated osteoclasts. After resorption, the reversal phase occurs, where mononuclear cells appear on the bone surface and prepare it for new bone formation. These cells also provide signals for osteoblast differentiation and migration. The formation phase follows, with osteoblasts laying down new bone until the resorbed bone is completely replaced. After this phase, a resting period begins until a new remodelling cycle is initiated. The stages of the remodelling cycle have different durations. Resorption lasts approximately 2 weeks, the reversal phase can extend up to 4 or 5 weeks, and formation may continue for 4 months until the new bone structural unit is fully formed [49].

1.2. Biomaterials

Biomaterials are specially designed and developed materials that interact with biological systems for medical or health care applications. These materials are used in a wide range of fields, including regenerative medicine, drug delivery, implantology, tissue engineering and medical equipment. Biomaterials are used to mimic or improve the functions of natural tissues or organs, provide support, promote healing, or deliver therapeutic substances. They are carefully selected and designed, not causing harmful reactions in the body, and can easily integrate with living tissues.

As an alternative to biological tissues, many other materials can be used. The most important properties of bone substitute is that: it should be biocompatible with the host and not cause an inflammatory process; it should be easily incorporated into the place of the bone defect place; the durability of the implant is important to keep its form and capacity over time, and it should also be bioactive, with the possibility of sterilisation and easily available at an acceptable cost [59].

Polymers have emerged as versatile biomaterials with a wide range of applications in various fields of medicine. Biocompatible polymers are extensively used in fields such as medicine, tissue engineering, drug delivery, and medical devices. They offer several advantages, including their tuneable properties, versatility, and ability to degrade or be resorbed in the body over time. Polyethylene glycol (PEG) is a widely used biocompatible polymer that is water-soluble and has a low toxicity profile. Poly(lactic-co-glycolic) acid (PLGA) is a biodegradable and biocompatible copolymer. It is commonly used in drug delivery systems and tissue engineering scaffolds. Chitosan is a naturally derived biocompatible polymer, that has antimicrobial properties

and promotes tissue regeneration. It is used in drug delivery systems, and tissue engineering scaffolds [60]. These are just a few examples of biocompatible polymers, and there are many more being developed and studied for specific applications. The main advantage of polymeric materials in the bone replacement process is that the physical characteristics of polymers can be configured according to their application because of the easy change of their properties. However, they have poor mechanical properties and a lack of grip on the natural bone [59].

Hydrogels, a fascinating application of polymers as biomaterials, represent a specialized network of interconnected hydrophilic polymers characterized by micropores that efficiently trap significant amounts of water. Among the widely acknowledged hydrogels, those based on polyethylene glycol and alginate have gained considerable attention. Their popularity stems from their unique ability to be delivered through minimally invasive methods and to undergo in-situ gelation, forming a three-dimensional cell microenvironment enriched with a high water content. These hydrogels possess distinctive viscoelastic properties, making them particularly well-suited for applications in cartilage regeneration. The versatility of hydrogels, however, extends beyond cartilage, as ongoing research explores their potential in various bone-related uses [61-63]. Their advantageous characteristics include simplicity in chemical biofunctionalization, as well as ease of cell encapsulation and delivery [64-66].

Composites formed by combining polymers and calcium phosphate represent a cutting-edge class of materials that synergistically leverage the unique properties of both constituents [67-70]. This innovative approach results in a material with enhanced characteristics, making it exceptionally well-suited for diverse biomedical applications. Primarily utilized in bone tissue engineering, drug delivery systems, and dental applications, these composites offer a versatile solution for addressing various challenges in the field [71].

Typically, these composites exhibit a well-defined structure, comprising a polymer matrix and calcium phosphate particles. The polymer matrix, often derived from biodegradable polymers, plays a pivotal role by providing essential attributes such as flexibility, processability, and biocompatibility. This renders the composite adaptable to a broad spectrum of medical applications [71]. Widely employed polymers in this context include polylactic acid (PLA), polyglycolic acid (PGA), and their copolymers (poly lactic-co-glycolic acid (PLGA)), alongside naturally occurring polymers like chitosan and gelatine.

The integration of calcium phosphate, notably hydroxyapatite (HAp) or tricalcium phosphate (TCP), further enhances the composite's performance. Calcium phosphate brings biocompatibility, bioactivity, and osteoconductivity to the table, significantly impacting the material's overall efficacy in medical applications. Moreover, the incorporation of calcium phosphate contributes to the mechanical reinforcement of the polymer matrix, elevating crucial properties such as strength and stiffness. This reinforcement makes the composite particularly suitable for applications requiring load-bearing capabilities. A notable advantage of these composites lies in their ability to biodegrade, ensuring compatibility with the body's natural processes. The inherent biocompatibility of the materials promotes a favourable environment for tissue regeneration, adding a regenerative dimension to their application profile. The properties of these composites can be tailored by adjusting the composition, ratio of polymer to CP, and processing techniques, to meet specific requirements for different applications in the field of regenerative medicine [71].

Bioglass, also recognized as bioactive glass, stands out as a synthetic glass endowed with the exceptional property of forming a bond with living tissues. It is composed primarily of silicon dioxide (SiO_2), calcium oxide (CaO), sodium oxide (Na_2O), and phosphorus pentoxide (P_2O_5) [72,73]. Originating from the pioneering work of scientists at the University of Sheffield in the 1960s, bioglass has evolved into a material of significant interest in the biomedical field, finding diverse applications over the years. The key characteristic of bioglass is its bioactivity, which refers to its ability to form a strong and stable bond with living tissues [73]. When bioglass comes into contact with body fluids, it activates a series of reactions that ultimately lead to the formation of a layer of HA on its surface, making it biocompatible and capable of integrating with the surrounding biological structures [64,73]. Bioglass has excellent osteogenic and gene expression characteristics, however due to slow decomposition rates their decomposition by-products are not bioresorbable and might be toxic to the body [35,74]. This consideration underscores the need for thorough exploration and refinement of bioglass compositions and decomposition processes to address these challenges.

Bioceramics are a class of ceramic materials that are extensively used in biomedical applications due to their favourable properties and biocompatibility. Bioceramics have witnessed a growing demand in recent years due to their use in medical devices and implants. The global market for bioceramics estimated at 21.6 billion of US $ in the year 2022, is projected to reach a revised size of 31.4 Billion by 2030 [75]. Bioceramics have emerged

as a valuable solution for the treatment of bone defects, offering a long history of utilization in the field of regenerative medicine. The ability of bioceramics to mimic the mineral composition of natural bone and support the regeneration of new tissue has positioned them as valuable tools in bone defect repair and reconstruction. The origins of bioceramics in bone defect treatment can be traced back to 975 AD, where calcium sulphates were employed as bone cement to promote bone healing [76,77]. A significant milestone occurred in 1769 with the discovery of CP in bones, unveiling the natural presence of this essential mineral in skeletal structures. The 1800s marked a period of extensive compositional analysis of calcified tissues, leading to the classification of CP into distinct subgroups based on their unique properties and crystal structures [76,78]. In the 1900s, extensive research efforts were dedicated to investigating the clinical applications of bioceramics for the treatment of bone defects [35,79]. These studies aimed to assess the biocompatibility, bioactivity, and osteoconductivity of various bioceramics materials, paving the way for their utilization in surgical procedures and implantology. The combination of bioceramics with other biomaterials, such as polymers, metals, or growth factors, has further expanded their capabilities, enabling tailored approaches for specific clinical scenarios.

Throughout history, advancements in bioceramics research have led to the development of diverse materials such as HAp and TCP, each with its own set of unique properties and applications. These bioceramics materials have demonstrated remarkable potential in facilitating bone healing, improving implant stability, and promoting integration with surrounding tissues, and some have been commercialized [80]. Figure 3 shows some of the current products on market.

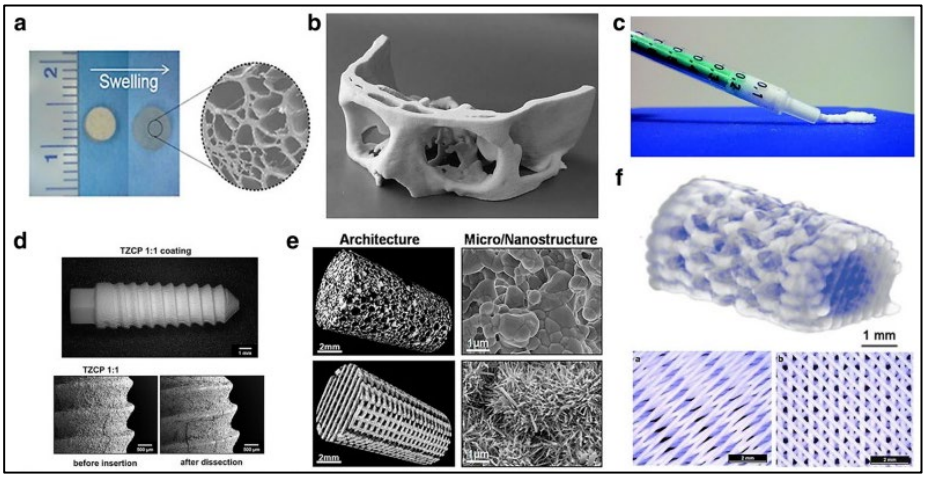

Figure 3. CP-based applications: **a)** Mg-WH incorporated hydrogel scaffold; **b)** Cranial segment made of tetracalcium phosphate and β-TCP; **c)** The injectable paste included calcium phosphate nanoparticles; **d)** Mixed zirconia calcium phosphate deposited on a dental implant; **e)** 3D printed CDHA scaffolds. **f)** 3D printed CPC [41].

HAp closely resembles the bone mineral composition of natural bone and exhibits excellent biocompatibility and bioactivity [81]. It can support cell adhesion, proliferation, and differentiation, making it an ideal material for promoting bone regeneration. Another prominent bioceramic is TCP, specifically β-TCP, which possesses similar chemical composition to the mineral phase of bone. TCP has good biocompatibility and can undergo gradual resorption in the body, allowing for new bone formation to take place [82]. Apart from HAp and TCP, there are other calcium phosphates used in biomaterial applications. Biphasic calcium phosphates (BCPs) combine HAp and TCP in varying ratios, allowing for a tailored balance between bioactivity and resorbability [83]. Octacalcium phosphate (OCP), another calcium phosphate, acts as a precursor to HAp and TCP and exhibits high solubility [84]. It has a unique crystalline structure and can undergo dissolution and transformation into other calcium phosphate phases. OCP-based biomaterials have shown promise in bone tissue engineering applications. Amorphous calcium phosphate (ACP) is a non-crystalline form of calcium phosphate with high solubility [85]. It can rapidly dissolve, releasing calcium and phosphate ions important for bone formation. ACP-based biomaterials have been investigated for bone regeneration and as carriers for controlled drug delivery. Calcium phosphate cements (CPCs) are

injectable biomaterials composed of powdered CP and a liquid component [86]. They can fill bone defects and set in situ. CPCs offer advantages such as moldability and biocompatibility. They are suitable for minimally invasive procedures and can conform to complex shapes. The choice of CP biomaterial depends on specific requirements, such as degradation rate, mechanical properties, and bioactivity.

1.2.1. Magnesium whitlockite

Magnesium whitlockite (Mg-WH: $Ca_{18}Mg_2(HPO_4)_2(PO_4)_{12}$) is a calcium orthophosphate in which calcium ions are partially substituted by magnesium ions. Recently, it has been shown that synthetic Mg-WH stimulates cellular proliferation, osteogenic differentiation, and consequent bone ingrowth [36,87]. It was found that magnesium ions promote bone formation while preventing the activity of osteoclasts [28]. Moreover, magnesium ions in CP biomaterials utilized in maxillofacial bone regeneration therapy stimulated its biodegradation and improved osteoconductivity, which might be attributed to its Ca^{2+} and Mg^{2+} ions stoichiometry [88]. Generally, whitlockite ($Ca_{18}(Mg_{1-x}Fe_x)_2(HPO_4)_2(PO_4)_{12}$) is a CP that was first identified in minerals collected from the Palermo Quarry, New Hampshire. It was discovered by Charles A. Whitlock in the early 20th century and is named in his honour. [76,88]. It is a rare mineral present in the crust of the earth and asteroids, found in granitic pegmatites, phosphate rock deposits, guano caves and in chondrite meteorites. In biological systems, magnesium-substituted whitlockite has been detected in various tissues and calcifications [89]. Notably, it has been observed in human tooth enamel, playing a crucial role in the mineralization process and contributing to the enamel's hardness. Beyond dental applications, Mg-WH has been identified in pathological calcifications associated with a range of conditions, including arthritic joint calcifications, supragingival calculus, dental plaque, calcified deposits in the pulmonary system, aortic calcifications, prostate calculi, urinary tract stones, and salivary gland stones [35].

Mg-WH structure is closely related to β-TCP crystal structure. The terms Mg-WH and β-TCP (Mg-WH's Ca/P ratio is 1.43, while β-TCP is 1.50) are frequently used interchangeably due to the difficulty of distinguishing them based solely on XRD analysis, despite their significant differences in crystalline structures [35]. Notably, β-TCP solely consists of calcium cations within its crystal lattice. On the other hand, Mg-WH contains both Ca^{2+} and

Mg^{2+} cations. Another notable distinction is the absence of hydrogen phosphate ions (HPO_4^{2-}) in β-TCP.

The crystal structure of synthetic Mg-WH has been extensively studied, and its characteristics were described by Gopal *et al*. in 1973 [35]. Through their research, it was determined that the crystals of whitlockite have a space group of R3c (#161) with lattice parameters of a = 10.350(5) Å and c = 37.085(12) Å. Recently, the crystal structure investigation of a natural specimen of whitlockite from Palermo was achieved by means of single-crystal X-ray diffraction by Capitelli *et al.* Crystal structure refinement from XRD, in the space group R3c, revealed unit cell parameters of a = 10.3685(4) Å, c = 37.1444(13) Å [90]. The crystal structure of Mg-WH reveals an arrangement of two distinct types of columns, denoted as A and B (Figure 4), which are organized in a periodic manner along the c-axis. The unit cell of Mg-WH consists of three A columns and nine B columns. Column A consists of alternating Mg^{2+} and HPO_4^{2-} units, with empty spaces interspersed between them. Column B is more densely packed and exhibits a sequence of Ca(1)–$P(3)O_4$–$P(2)O_4$–Ca(2)–Ca(3) units. These columns can be further classified into three subtypes each, characterized by identical atomic arrangements but shifted relative to each other along the c-axis (Figure 4b). Each A column is surrounded by six B columns belonging to two different subtypes, while each B column is flanked by two A columns of different subtypes on opposite sides and four B columns of two different subtypes (Figure 4d). Within the crystal structure of WH, there are three distinct sites for calcium ions and three sites for phosphorus ions. Among them, Ca^{2+}(1) and Ca^{2+}(2) ions are directly bonded to five PO_4^{3-} groups and one HPO_4^{2-} group, whereas the Ca^{2+}(3) site is surrounded by four neighbouring PO_4^{3-} groups. In column A, the x and y atomic coordinates of Mg^{2+} and P(1) are both set to zero, indicating that these atoms are aligned along a straight line. On the other hand, in column B, the x and y atomic coordinates of Ca(1), Ca(2), Ca(3), P(2), and P(3) have different values, suggesting a distortion in column B compared to column A. In the WH structure, Mg^{2+} ions substitute the energetically favourable octahedrally coordinated Ca(5) site, while Ca(4) is more stable as a vacancy. The locations of protons are known to be in proximity to the Ca(4) sites [32].

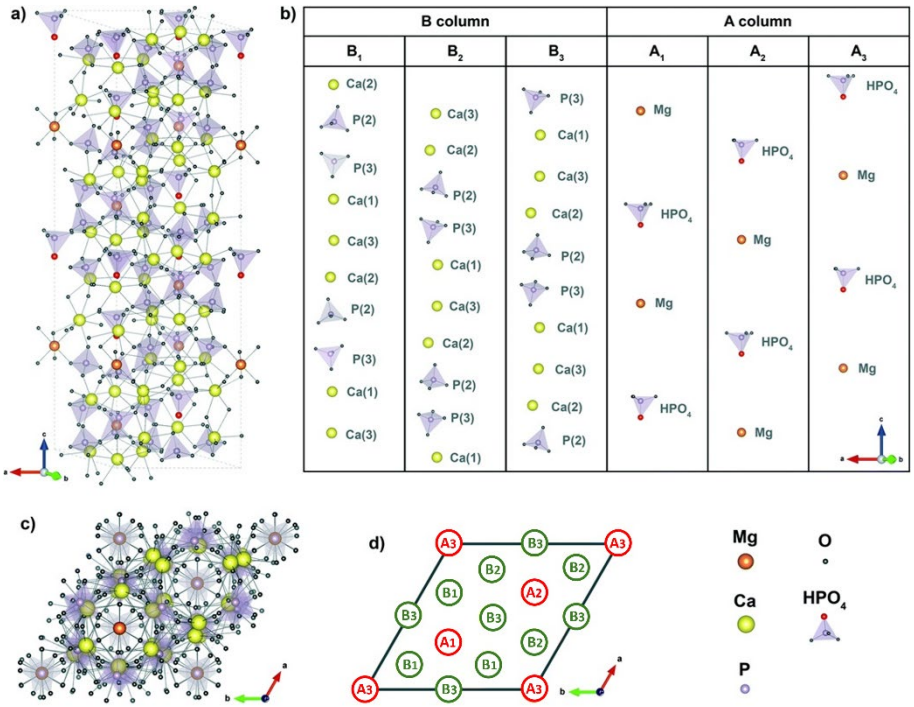

Figure 4. Unit cell of Mg-WH (a and c); the arrangement of atoms in structural columns (b); arrangement of columns in the unit cell (d). Adopted from [32].

Mg-WH is stable at acidic pH, and soluble in physiological solvents. It is highly biocompatible [91], biodegradable, bioresorbable [92] and bioactive, with compatible mechanical properties [93]. Compared to HAP, Mg-WH possesses better mechanical properties, faster resorbability, and promotion behaviour on osteogenesis [94]. Recent study by Lee et al. [94] presented a histological, radiological, and immunohistochemical evaluation of the bone healing potential of Mg-WH granules in a 5 mm diameter calvarial bone defect in rats. The histological evaluation revealed no inflammatory reaction, with newly formed bone exhibiting the same thickness as the original bone. Besides, immunohistochemistry confirmed that Mg-WH granules promoted bone regeneration with the significantly higher expression of bone morphogenetic proteins-2, alkaline phosphatase, osteopontin, and osteocalcin compared to the nontreated group without the addition of exogenous cells or growth factors. These results suggest that WH has excellent potential for application in bone tissue regeneration [94]. It was demonstrated by Kim *et al.* demonstrated that Mg-WH nanoparticles can recapitulate the early stage of bone regeneration by stimulating osteogenic differentiation, prohibiting

osteoclastic activity, and transforming into mechanically enhanced hydroxyapatite-neo bone tissues by a continuous supply of PO_4^{3-} and Mg^{2+} under physiological conditions [95]. Despite its excellent properties, Mg-WH material has always been dominated by other CPs, which may be related to its difficulty in synthesis [35].

1.3. Synthesis of calcium phosphates

The ceramics synthesized at high temperatures exhibit an extremely high crystallinity, which deviates significantly from natural bone [18]. Moreover, some thermally unstable CP phases cannot be synthesized by conventional high-temperature methods [19]. Biomaterials obtained under the low-temperature regime could exhibit greater tissue compatibility than conventional bioceramics [20,21]. Wet-chemical synthesis methods, such as sol-gel, hydrothermal, microwave-assisted, microemulsion, and co-precipitation, in which the precursor salts are in solution, allow a homogeneous distribution of the starting components, and, therefore, allow the synthesis of the end products at relatively low temperature [16].

1.3.1. Dissolution-precipitation synthesis of calcium phosphates

A low-temperature synthesis method, based on phase transformation through a ***dissolution-precipitation reaction***, is employed for synthesizing poorly crystalline CP materials. This method is utilized to prepare bioceramics, aiming to achieve physicochemical properties similar to those found in bone apatite [22,23]. The dissolution-precipitation reaction is a highly reproducible synthesis method. It is possible to rigorously control the entire synthesis process and, if necessary, tune the desired physical and chemical properties of the obtained materials [22-24].

There are three major requirements for the compositional transformation through the dissolution-precipitation reaction. Firstly, the solubility of the precursor material must be higher than that of the final product. Secondly, any missing components must be supplied from the aqueous solution. Thirdly, precipitates or crystals of the final product should have the ability to connect to maintain the shape of the block (note the third requirement is not important for powdered samples) [43].

Dissolution-precipitation synthesis method was successfully utilized by K. Ishikawa and K. Hayashi to obtain carbonate apatite (CO_3Ap) from calcite ($CaCO_3$) precursor [43]. Calcite was chosen as the starting material due to its advantageous combination of low solubility in neutral pH aqueous solutions

and the presence of both calcium and carbonate ions. Chemically pure calcite blocks were easily fabricated by simply exposing calcium hydroxide ($Ca(OH)_2$) compact to carbon dioxide (CO_2) (see eq. 1):

$$Ca(OH)_2 + CO_2 \rightarrow CaCO_3 + H_2O \quad (1)$$

Transformation from calcite to CO_3Ap requires phosphate ions to be present in the reaction solution. The $CaCO_3$ block was immersed in a phosphate salt solution for this compositional transformation. When $CaCO_3$ is immersed in an aqueous solution, it dissolves and supplies Ca^{2+} and CO_3^{2-} (see eq. 2). If other ions are absent, water becomes saturated with $CaCO_3$. However, when water contains PO_4^{3-}, the phosphate salt aqueous solution can be supersaturated with respect to CO_3Ap when both Ca^{2+} and CO_3^{2-} are supplied by the dissolution of $CaCO_3$. Thus, Ca^{2+}, PO_4^{3-}, and CO_3^{2-} precipitate as CO_3Ap (see eq. 3), and the precipitated CO_3Ap crystals interlock with one another. Continuous dissolution-precipitation reactions lead to the compositional transformation from $CaCO_3$ to CO_3Ap, maintaining the macroscopic structure of the precursor.

$$CaCO_3 \rightarrow Ca^{2+} + CO_3^{2-} \quad (2)$$

$$Ca^{2+} + PO_4^{3-} + CO_3^{2-} \rightarrow Ca_{10-a}(PO_4)_{6-b}(CO_3)_c \quad (3)$$

Another example of a successful synthesis is carbonate apatite which was fabricated by a dissolution-precipitation method (CO_3Ap-DP). Granules of this material were fabricated by compositional transformation via the dissolution-precipitation reaction using calcite granules as a precursor. These granules were published in several independent papers [22,96-99]. Study [100] aimed to compare tissue response of CO_3Ap fabricated by the dissolution-precipitation reaction using calcite as a precursor and Bio-Oss®, which is widely used in orthopedic and dental fields as a synthetic bone substitute. In [100] first, $Ca(OH)_2$ powder was pressed uniaxially using a press machine, and then the compacted $Ca(OH)_2$ discs were placed in a carbon dioxide reaction vessel saturated with water vapor for carbonation. The prepared $CaCO_3$ blocks were then crushed into granules and were immersed in 1 mol/L Na_2HPO_4 at 80 °C for 14 days to allow compositional transformation. XRD and FT-IR analysis revealed that CO_3Ap-DP and Bio-Oss® were both B-type carbonate apatite with low crystallinity. When a bone defect made at the femur of rabbits was restored with CO_3Ap-DP and Bio-Oss®, CO_3Ap-DP granules were partially replaced with newly formed bone, however, Bio-Oss® remained even at 8 weeks after implantation. At four weeks post-implantation, the CO_3Ap-DP granules yielded a significantly

larger amount of new bone than the Bio-Oss® material (see Figure 5). The results obtained in the present study demonstrated that CO_3Ap-DP and Bio-Oss® showed different behaviour even though they were both classified as CO_3Ap. The CO_3Ap-DP granules fabricated by the dissolution-precipitation method showed good biocompatibility in bony defects of rabbit femur. This finding suggested that CO_3Ap-DP could be useful as a bone substitute and biodegradative scaffold for bone regeneration [100].

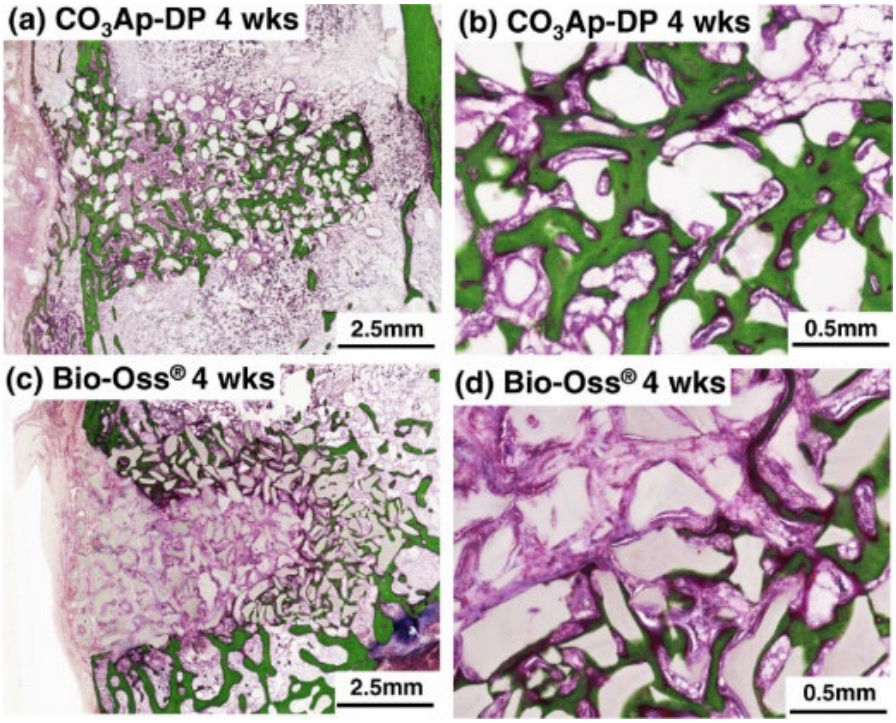

Figure 5. Histological views of the CO_3Ap-DP and Bio-Oss® at 4 weeks after surgery: **a)** new bone (green colour) formed on the granule without interposition of the soft tissue between CO_3Ap-DP granules and bone; **b)** new bone formed at the periphery of the bone defect; continuity of the cortical bone was not restored in the part **c)** and **d)** [100].

Octacalcium phosphate (OCP) has attracted much attention as an artificial bone substitute because of its excellent osteoconductive and bone replacement properties. In [101] study, OCP foam with an interconnected porous structure was fabricated through a dissolution–precipitation reaction using calcium sulfate hemihydrate ($CaSO_4 \cdot 0.5\ H_2O$, CSH) granules as precursors in a NaH_2PO_4 (NaDP) solution (see Figure 6). When synthesized OCP foam was implanted into bone defects in a rabbit femur, the OCP foam

showed an excellent tissue response, and the newly formed bone penetrated into the porous structure. The osteoconductivity and bone-replacement rate were significantly higher than those of an OCP compact.

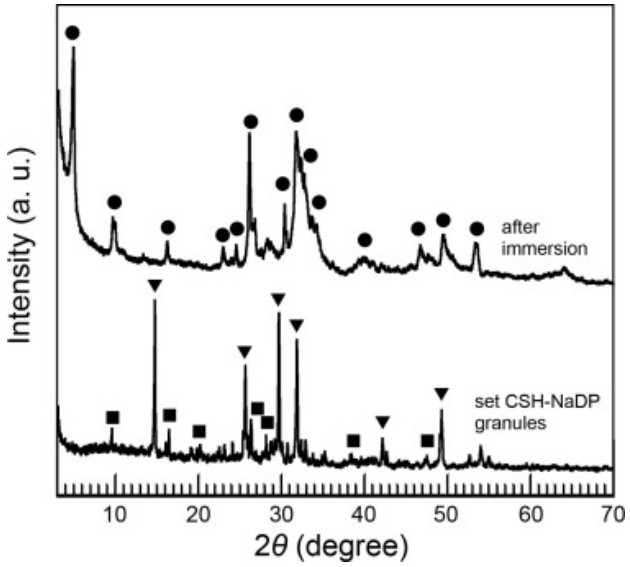

Figure 6. XRD patterns of the set CSH-NaDP (CSH marked as triangles, NaDP marked as squares) granules before and after their immersion. OCP (marked as a circle) references are shown to facilitate comparison [101].

1.3.2. Synthesis of Mg-WH

The biological performance of CP ceramics, encompassing biodegradation rate, osteoconductivity, bioactivity, and mechanical properties, is heavily influenced by the synthesis method. Synthesis method affects the phase composition, purity, crystallinity, size, morphology of the particles obtained and therefore influences the biomedical performance of artificial implants [14,15]. Therefore, the selection of the synthesis method is very important in the preparation of materials used for biomedical applications [10]. For bioceramics intended for health-related applications, there is a preference for materials with lower crystallinity and a larger specific surface area. This choice is driven by the aim to enhance tissue compatibility and potentially incorporate other biological functionalities.

1.3.2.1. Precipitation synthesis of Mg-WH

In 2014 Jang *et al.* reported a ***precipitation synthesis*** of pure Mg-WH nanoparticles with limited excess Mg^{2+} ions under an acidic condition in a simple ternary $Ca(OH)_2$–$Mg(OH)_2$–H_3PO_4 aqueous system [89]. Initially, $Ca(OH)_2$ and $Mg(OH)_2$ were mixed at various molar ratios, and heated between 60 and 90 °C. Then, an appropriate amount of H_3PO_4 was added dropwise into the $Ca(OH)_2$ and $Mg(OH)_2$ mixed solution while vigorously stirring. The precipitates were aged for more than 9 h and then filter-pressed and dried using a lyophilizer. Their synthesized Mg-WH nanopowder showed excellent biocompatibility, which was comparable with HAP and much better than previous bulk TCP.

Later, in 2015 by Jang *et al.* [34] studied the precipitation pathway of Mg-WH dividing the process into sequential stages. In their work, Mg-WH was synthesized by precipitation with $Ca(OH)_2$, $Mg(OH)_2$, and H_3PO_4. First, 0.77 M of $Ca(OH)_2$ and 0.23 M of $Mg(OH)_2$ were mixed in 500 mL of distilled water at 70 °C using a stirrer. After 1 hour of stirring, 500 mL of 0.95 M H_3PO_4(aq) was added to the above solution dropwise and while vigorously stirring. Stages from I to III were assigned to the conditions where 0 – 305 mL, 305 – 390 mL and 390 – 500 mL of H_3PO_4 were added into the system. During these stages, the pH of the system changed from 11.2 to 5.8, from 5.8 to 4.5 and from 4.5 to 3.5, respectively. After the addition of H_3PO_4 was complete, the pH of the system was approximately 3.3 (stage IV) and 3.7 (stage V) with aging times of 5 hours and 24 hours, respectively. At stage I, HAP and $Mg(OH)_2$ were the major phases of the precipitant (see Figure 7). At stage II, when the $Ca(OH)_2$ was almost consumed, $Mg(OH)_2$ began to react with H_3PO_4 and the XRD peaks of dimagnesium phosphate (MP: $MgHPO_4{\cdot}xH_2O$) appeared. Then, as the system became more acidic at stage III, HAP became unstable and partially changed into DCPD. Immediately after the complete addition of the total amount of H_3PO_4, HAP, DCPD and MP phases were found. At stage IV, during ageing in the acidic system of pH 3.3, HAP, DCPD and MP gradually dissolved. In contrast, within the ageing time of 5 hours, the XRD peak intensities of the WH phase increased. Finally, at stage V when the aging time was 24 hours, only a pure phase of WH was observed.

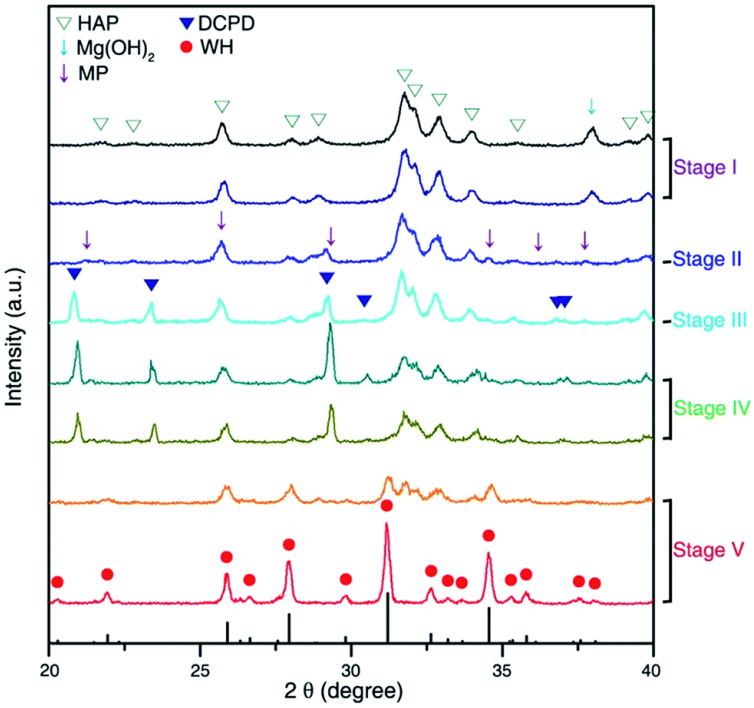

Figure 7. XRD analysis of intermediate precipitants collected during the synthesis of Mg-WH. Peaks corresponding to phase of HAP, $Mg(OH)_2$, MP, DCPD and Mg-WH in the XRD data are marked as the green triangle, cyan arrow, purple arrow, navy triangle and red circle, respectively. Reference peaks of Mg-WH from JCPDS no. 70-2064 are shown at the bottom [34].

Recently, piezoelectric biomaterials have gained increased attention in the field of generating bioelectricity, which is an integral part of all living systems. Another interesting study was conducted by V. K. Kaliannagounder *et al.* [102], where, for the first time in the literature, they explored the piezoelectric properties of WH nanoparticles due to their non-centrosymmetric structural presentation. They reported the feasibility of these piezoelectric nanoparticles to generate bioelectric signals similar to native tissues for enhanced non-invasive bone tissue regeneration. The authors synthesized Mg-WH nanoparticles through precipitation synthesis. To enhance the piezoelectricity in synthesized WH nanoparticles, a portion of the products was mixed with a binder solution, and the granulated powder was then hydraulically pressed into pellets. These pellets were subsequently annealed at different temperatures (500 °C, 750 °C, and 1000 °C) for 3 hours. The *in vitro* cell proliferation and osteogenic differentiation studies revealed that the piezoelectric WH NPs demonstrated enhanced cell proliferation

compared to control nanoparticles. This is the first report on piezoelectric Mg-WH nanoparticles that offers the great potential of piezoelectric Mg-WH nanoparticles in the field of regenerative medicine, especially in the field of bone tissue engineering.

1.3.2.2. Solid-liquid-solution synthesis of Mg-WH

Mg-WH samples were synthesized by C. Wang *et al.* employing a ***solid-liquid-solution process*** within a tri-solvent system. This process hinges upon phase transfer and separation mechanisms occurring across liquid, solid, and solution interfaces [36]. Main synthesis factors, including the ratio of precursor and reaction solvent composition optimized to generate Mg-WH nanocrystals with tunable size, morphology (nanoplates, nanospheres), and surface properties (hydrophobic, hydrophilic) were optimized. It was found that the morphology and surface properties of Mg-WH can be controlled by the ratio between the precursors, and ethanol affects the crystallinity and the morphology of nanocrystals by controlling the diffusion rate of the precursors. Furthermore, molecular dynamics simulations have shown that the growth direction of nano-plates is closely related to the surfactant used in the synthesis process and its binding affinity. Finite element method simulations have demonstrated that ethanol/water ratio plays an important role in determining Mg-WH crystallinity and morphology [36].

1.3.2.3. Solid-state synthesis of Mg-WH

Recently S. Batool et al. reported on a synthesis method for Mg-WH using a ***solid-state reaction***. [103] Through the number of experiments, optimized parameters such as precursor type, temperature and reaction time have been optimized and reported in [103]. The synthesis was carried out by mixing, grinding, and heat-treating the precursors at high temperatures without any medium under the ambient environment. In brief, 1.0 g of monetite, 0.625 g of magnesium hydroxide, and 1.135 g of tricalcium phosphate were mixed, crushed and heated at 1100 °C for 6 h in a furnace. XRD analysis confirmed that the synthesized material has a Mg-WH phase (see figure 8) while FT-IR and Raman spectroscopy analysis confirmed the presence of a peak of HPO_4^{2-} that is a characteristic of Mg-WH [103].

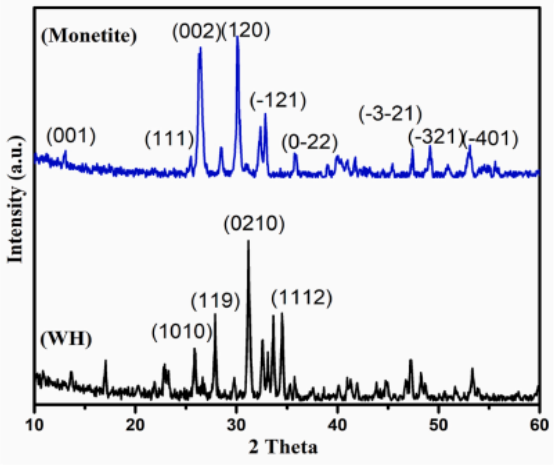

Figure 8. XRD of synthesized Mg-WH [103].

1.3.2.4. Hydrothermal and microwave-assisted synthesis of Mg-WH

The ***hydrothermal synthesis*** is known as a promising method to synthesize new Mg-WH and other structure-type CPs. Hydrothermal synthesis of Mg-WH hollow microspheres (WHHMs) was performed by dissolving 0.110 g of fructose 1,6-bisphosphate (FBP), 0.070 g of $CaCl_2$ and 0.055 g of $MgCl_2{\cdot}6H_2O$ in 36 mL of deionized water under magnetic stirring at room temperature [31]. The pH of the resulting solution was maintained at 9 using NaOH solution. Then, the resulting solution was transferred into a steel autoclave, sealed, heated in an oven to 180 °C and maintained for different times [31]. The effects of the synthesis methods and experimental conditions on the crystal phase, morphology, stability, and cytotoxicity of the products were investigated. It was found that the as-prepared WHHMs exhibit high biocompatibility. Moreover, the potential application of the as-synthesized WHHMs in protein adsorption was explored, with haemoglobin (Hb) used as a model protein, revealing a relatively high protein adsorption capacity [31]. Successful ***microwave-assisted hydrothermal synthesis*** of WHHMs, which were made for drug delivery systems, described by Qi C. *et al.* [31]. For the synthesis FBP, $CaCl_2$, $MgCl_2{\cdot}6H_2O$ were weighted and dissolved in deionized water under stirring at room temperature. The pH of the resultant solution was maintained at 9. The mixture then was loaded into a cylindrical autoclave, sealed, placed in a high-strength outer container and heated at different temperatures and a variety of times in a microwave oven. It was demonstrated that the different synthesis methods and experimental conditions have significant effects on the crystal phase and morphology of the product. In addition, the as-prepared WHHMs demonstrated high biocompatibility and

showed a relatively high protein (haemoglobin, Hb) adsorption capacity, thus, they are promising for applications in various biomedical fields (see Figure 9).

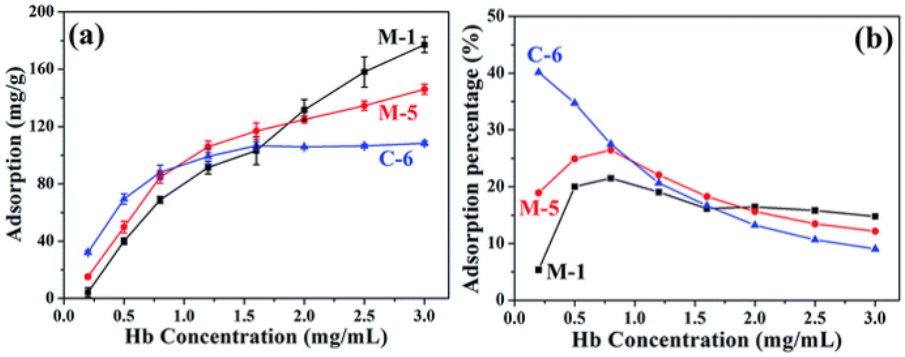

Figure 9. Hb adsorption capacity (a) and adsorption percentage (b) of the samples M-1, M-5 and C-6 as a function of initial Hb concentration. [31]. The M-1 sample was prepared at 120 °C for 10 minutes, the M-5 sample at 180 °C for 10 minutes using the microwave-assisted hydrothermal method, while the C-6 sample was prepared at 180 °C for 24 hours using the conventional hydrothermal method [31].

Another example of microwave-assisted hydrothermal synthesis was shown by Zhou *et al.* [104]. They synthesized HAp and Mg-WH hollow microspheres using creatine phosphate disodium salt tetrahydrate (creatinine phosphate) as a source of phosphate ions, which is a biocompatible organic compound naturally occurring in our liver. WH hollow microspheres were prepared by mixing 0.389 g of $CaCl_2$, 0.305 g of $MgCl_2 \cdot 6H_2O$, and 0.981 g of creatinine phosphate in 200 mL of deionized water with magnetic stirring at room temperature. Then, 40 ml of the acquired solution was poured into a cylindrical autoclave, tightly closed, placed in a high-strength outer container, and heated in a microwave oven to a temperature of 120 °C for 10 min. To achieve relatively uniform heating, the autoclave was rotated continuously. After the product cooled to room temperature, it was centrifuged, washed several times with deionized water and ethanol, and finally freeze-dried. Later, from prepared hollow microspheres were synthesized HAp/chitosan and WH/chitosan composite membranes or porous scaffolds. Later, the authors conducted a comparative investigation of their effects on bone regeneration in calvarial defects. It was demonstrated that magnesium incorporation facilitated better bone formation in WH/chitosan scaffolds than in HAp/chitosan scaffolds. In vitro studies showed that WH/chitosan membranes possess good biocompatibility and improved osteoinductivity. Compared to the HAp/chitosan scaffold, the WH/chitosan scaffold significantly enhanced new bone formation in rat calvarial defects [104].

1.3.2.5. Dissolution-precipitation synthesis of Mg-WH under hydrothermal conditions

Crystals of synthetic Mg-WH have been grown for the first time by heating an amorphous phosphate under hydrothermal synthesis conditions at 300 °C, for 2 weeks by Ito *et al.* in 1974. In 2016, Tas demonstrated transformation of synthetic brushite crystals by the hydrothermal synthesis into single-phase Mg-WH over the time period of 1 to 21 days and at 37 °C, 70 °C, and 115 °C in nonstirred physiologically relevant solutions [37]. The Mg^{2+} concentration of 1.5 mM was selected since it matches its concentration of human blood plasma. Confirmation of Mg-WH crystal formation at a final solution pH of 4.5 after 24 hours at 70 °C was achieved through XRD analysis. However, SEM images revealed the presence of two types of particles: hexahedral crystals (approximately 200 nm in their largest dimension) and flat plates resembling brushite crystals. Experimentally, it was concluded that Mg-WH formation proceeds in 1.5 mM Mg^{2+} solutions *via* a dissolution-precipitation process, the kinetics of which are enhanced by an increase in aging temperature from 37 °C to 70 °C. Further elevation to 115 °C resulted in the formation of single-phase Mg-WH.

Stefanovich *et al.* published a synthesis of single crystals of Mg-WH (alongside zinc, and cobalt WH) which was carried out by recrystallization of $CaHPO_4 \cdot 2H_2O$ in 1 M NaCl solution with the addition of $Mg(NO_3)_2 \cdot 6H_2O$ [105]. The mass ratio of the components in the system was 4:1:1. Experiments were performed for three days at T = 270 °C, and 5 MPa in a standard 30 ml steel autoclave. Crystallization products were colourless 50 – 100 μm trigonal crystals (see Figure 8). The presence of hydrogen and HPO_4^{2-} ions was proved by FT-IR spectroscopy, differential scanning calorimetry and structural data analysis. This research provides new data on the possibility of using hydrothermal techniques for obtaining doped bone WHs.

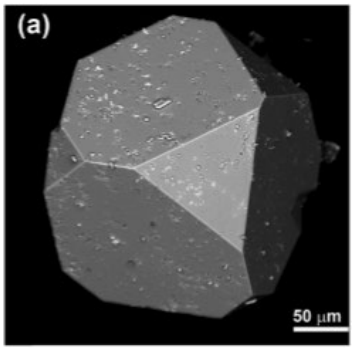

Figure 10. SEM image of obtained Mg-WH single crystal [105].

2. EXPERIMENTAL PART

2.1. Materials and reagents

1. Dicalcium phosphate dihydrate ($CaHPO_4 \cdot 2H_2O$, 99.1%, Eurochemicals).
2. Magnesium acetate tetrahydrate ($Mg(CH_3COO)_2 \cdot 4H_2O$, 98%, Roth).
3. 1 M aqueous solution of phosphoric acid (H_3PO_4(aq), 75%, Roth).
4. Ammonia aqueous solution (NH_3(aq), 25%, Roth).
5. Calcium sulfate dihydrate (gypsum, $CaSO_4 \cdot 2H_2O$, 98%, Merck).
6. Sodium dihydrogen phosphate (NaH_2PO_4, 99%, Merck).
7. Disodium hydrogen phosphate (Na_2HPO_4, 98%, Merck).
8. 5 % Nitric acid (HNO_3, Rotipuran® Supra 69 %, Carl Roth).
9. Deionized water.

2.2. Synthesis methodology

2.2.1. Synthesis of magnesium whitlockite powders with different magnesium content from brushite

Mg-WH nanopowders with variable magnesium content were prepared by a dissolution-precipitation synthesis method. $CaHPO_4 \cdot 2H_2O$ (mineral name brushite) and $Mg(CH_3COO)_2 \cdot 4H_2O$ were selected as the sources of calcium, phosphorous, and magnesium. The metal salts were taken in appropriate weights to achieve Ca/Mg molar ratio equal to 4, 6, 8, 10, 12, and 15 in the initial synthesis mixture. Subsequently, weighted precursors were placed in a 400 mL beaker and 100 mL of deionized water was added. The mixture was magnetically stirred (400 rpm) and heated. The reaction was carried out at 65 °C with continuous stirring throughout the synthesis. To initiate the dissolution of the precursors, 11 mL of 1 M H_3PO_4(aq) was added into the above mixture, and stirred for 30 min to obtain a clear homogeneous solution. The precipitation reaction was initialized upon drop-by-drop addition of NH_3(aq) resulting in immediate precipitation of white solid. During the experiment, the pH value of the reaction medium was maintained at 5.6. The final product obtained after 24 h of persisting synthesis was vacuum filtered, thoroughly washed numerous times with deionized water, and oven-dried overnight under a constant temperature of 60 °C. Finally, the samples were ground in an agate mortar to obtain fine powders for further studies. The prepared samples were abbreviated corresponding to the molar Ca/Mg ratio in

the initial synthesis mixture. The schematic representation of the synthesis of WH nanopowders with different magnesium content is shown in Figure 11.

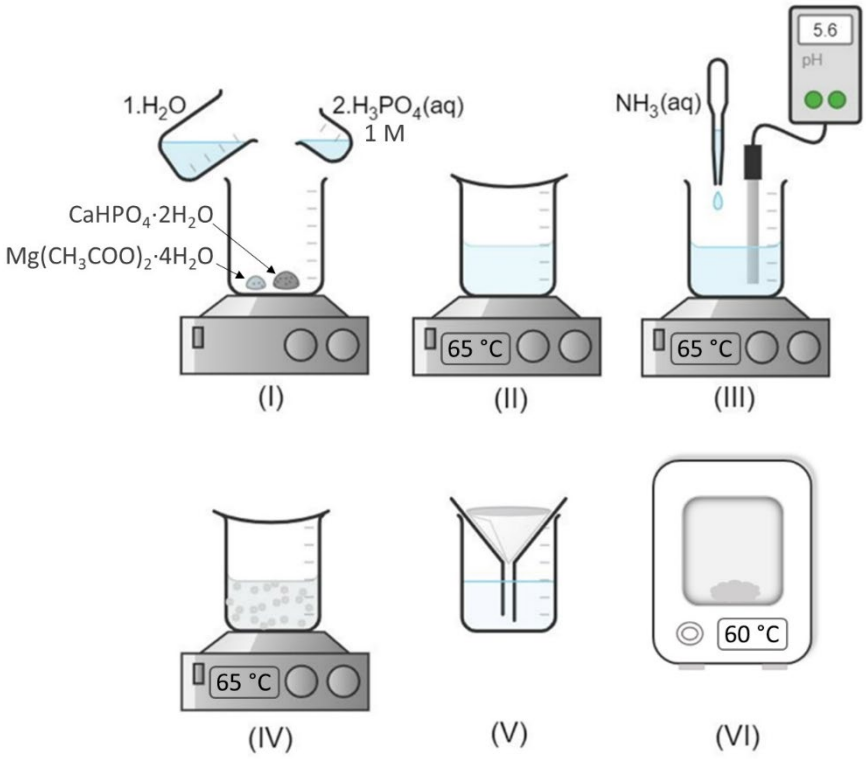

Figure 11. The schematic representation of the synthesis of WH nanopowders containing various magnesium amounts: the starting materials are dissolved in stages (I) and (II); precipitation of the reaction product was performed during stages (III) and (IV); resulting powders were filtered and dried during stages (V) and (VI), respectively.

2.2.2. Synthesis of magnesium whitlockite powders from gypsum

$CaSO_4 \cdot 2H_2O$ (gypsum), $Mg(CH_3COO)_2 \cdot 4H_2O$ (Ca/Mg molar ratio ~4), NaH_2PO_4, and Na_2HPO_4 were chosen as starting materials to investigate the phase transformations in the low-temperature synthesis of Mg-WH nanopowder under static and rotating conditions. The schematic representation of the synthesis is shown in Figure 12.

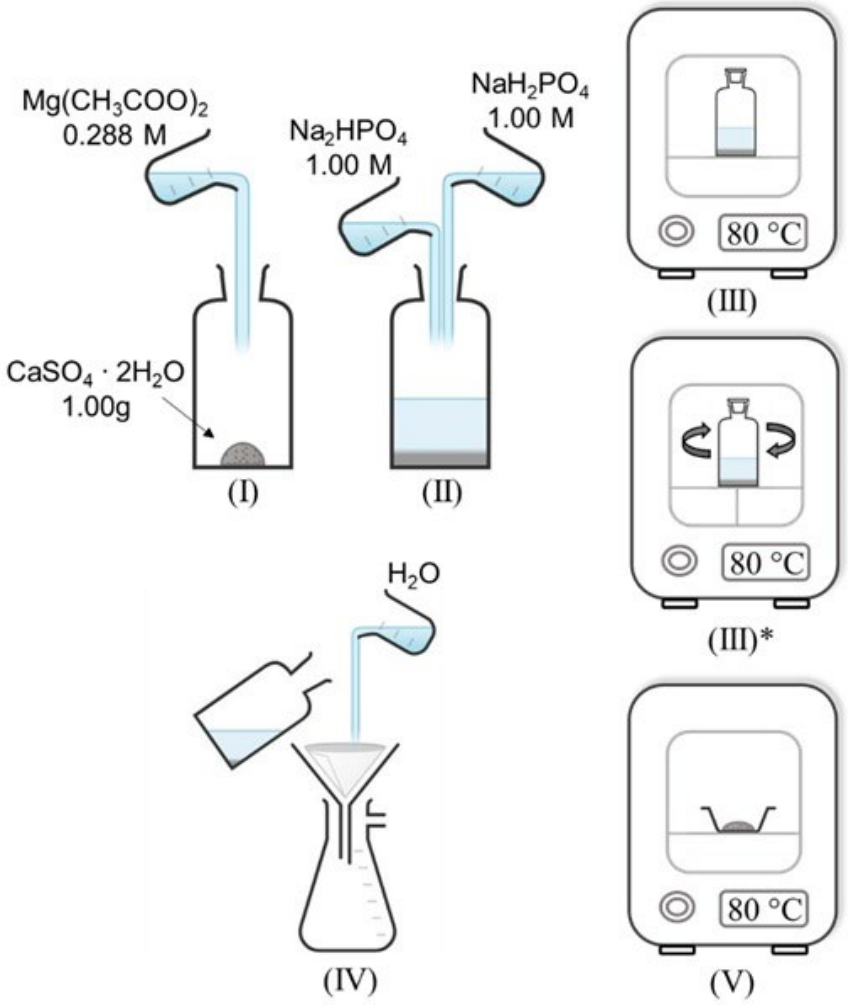

Figure 12. Schematic representation of the phase transformation investigation in the synthesis of Mg-WH nanopowder. In stage (I), the gypsum was mixed with the $Mg(CH_3COO)_2$ solution. In addition, Na_2HPO_4 and NaH_2PO_4 solutions were added (stage (II)). The reaction vessel was optionally placed in an oven or in a shaker incubator for the selected period of time (stage (III) or (III*), respectively). After being reacted, the synthesis products were vacuum filtered, thoroughly washed with deionised water (stage IV), and subsequently oven dried (stage V).

Briefly, 1.00 g of gypsum powder was kept in an aqueous solution made up of 5.00 mL of $Mg(CH_3COO)_2$ (0.288 M), 50 mL of NaH_2PO_4 (1.00 M), and 50 mL of Na_2HPO_4 (1.00 M) in a 250 mL bottle. Subsequently, the suspensions were optionally placed in an oven (static condition) or a shaker

incubator (rotating condition; Biosan, ES-20/80, with constant shaking at 120 rpm) both at 80 °C for the selected period of time. After being reacted for 4 h, 6 h, 12 h and 24 h, the synthesis products were vacuum filtered, thoroughly washed with deionized water (400 mL), and finally oven dried overnight at 80 °C. The samples were ground in an agate mortar to obtain fine powders for further studies. Materials synthesized under static conditions in this work were marked with the letter S, and those synthesized under rotational conditions were marked with the letter R, adding to each letter the duration of synthesis.

2.3 Characterization

Powder X-ray diffraction (XRD) analysis was accomplished with a Rigaku MiniFlex II diffractometer working in Bragg-Brentano (θ/2θ) geometry and using Ni-monochromatized CuKα radiation. The diffraction intensity data were obtained by scanning in the 2θ range of 10° – 60° with a step size of 0.02° at a scan speed of 2°/min. Identification of crystalline phases was attained by comparing the diffraction patterns obtained to the database standards provided by the International Centre for Diffraction Data (ICDD). For lattice parameter refinement, diffraction data were collected in an angular range of 10° – 100° in steps of 0.02° at a scan speed of 2°/min. Semi-quantitative analysis of the obtained phases was performed using the normalized corundum reference intensity ratio (RIR) method using Match! (version 3.13, Dr. Holger Putz, Crystal Impact, Bonn, Germany) software. Structural parameters of single-phase Mg-WH samples were extracted from XRD data with the help of the *FullProf* software (J. Rodriguez-Caravajal, Sep. 20, 2019, JGP-JRC [106]) employing Rietveld refinement (in the 2θ range of 10 – 70°). The initial model and the atomic coordinates were taken from the literature [90]. A common strategy was applied to all refinements in the following order: scale factors, background, lattice parameters, profile shape and width parameters, asymmetry, atomic coordinates, and site occupancies were refined. The quality of the refinement was evaluated according to computed agreement factors: the "goodness of fit" χ^2, profile residual R_p, and weighted profile residual R_{wp}. When these factors reached the lowest value (with only a small visible difference between the calculated/experimental patterns), the fit suggested the best refinement results, and the crystal structure was regarded as reasonable. To evaluate the crystallite size of single-phase samples Scherrer's formula using the *Rigaku PDXL* software (used in part 3.1) and the Le Bail method (used in part 3.2) were utilized. The Le Bail method performed using the *Fullprof* software. It is worth mentioning that a standard

lanthanum hexaborate (LaB_6) was measured to obtain instrumental broadening of the diffractometer and to subsequently remove its contribution from the experimental diffraction peak width [107]. To calculate the crystallinity of single-phase Mg-WH samples, while considering the experimental XRD patterns as a mixture of a crystalline and an amorphous phase of the analysed materials, the samples were measured (in the 2θ range of 10 – 70°) on a zero-background Si holder with the help of the aforementioned XRD apparatus and the *Match!* software. Note that, the air scatter was removed prior to profile fitting of detected XRD peaks.

For functional group investigation, the infrared spectra of the synthesized samples were collected by Fourier-transform infrared spectrometer (FT-IR, Alpha, Bruker Inc., Germany) in the 1550 – 450 cm^{-1} (or 1300 – 450 cm^{-1}) range, with a 2 cm^{-1} resolution as an average of 24 scans. A background measurement of 30 scans was executed before each analysis. The amount of elements (Ca, Mg and P) in the synthesized samples was estimated using an inductively coupled plasma optical emission spectrometer (ICP-OES, Perkin-Elmer Optima 7000DV). For the analysis, 20 mg of each sample was dissolved in 5 % HNO_3 and diluted with deionized water to obtain an appropriate volume of the analysed solution. The surface morphologies of the final powders were investigated using scanning electron microscopy (SEM) performed with a Hitachi SU-70 field-emission SEM and Tecnai F20 X-TWIN (FEIcompany) transmission electron microscopy (TEM) with an accelerating voltage of 200 kV equipped with EDX (EDAX) spectrometer, Gatan Orius CCD, was also used for additional morphological characterization (analysis was carried out using a bright field regime).

3. RESULTS AND DISCUSSION

The first part of the research will focus on the preparation of Mg-WH powders from brushite with varying magnesium content to potentially influence the biological properties of the synthesized CP. The second part of the research will focus on the synthesis and evaluation of the Mg-WH phase formation from gypsum under static and rotating conditions.

Both selected starting materials are nontoxic and cost-effective, while the synthesis procedure is characterized by simplicity, environmental friendliness, and efficiency. This study is crucial to advance our understanding of the underlying chemical processes and improve control over the chemical composition, crystallinity, and microstructure of the calcium phosphate product through customized synthesis approaches.

3.1. Synthesis and characterization of magnesium whitlockite powders with different magnesium content

Figure 13a shows the XRD patterns of synthesized Mg-WH nanopowders having variable magnesium content. WH exhibits R3c (#161) space group, and a rhombohedral lattice is used for the Miller indexation (ICDD #00-070-2064). The diffraction peaks at 2θ = 10.98°; 13.73°; 17.20°; 28.02°; 31.28° and 34.66° (for the sample with the highest magnesium content, namely Ca/Mg = 4) can be assigned to (0 1 2), (1 0 4), (1 1 0), (0 2 10) and (2 2 0) crystallographic planes of target $Ca_{18}Mg_2(HPO_4)_2(PO_4)_{12}$ phase, respectively. The characteristic diffraction peaks of the WH crystal structure were preserved throughout all obtained samples. No other secondary phases due to a varied amount of the Ca^{2+} and Mg^{2+} ions were observed in the XRD patterns of samples with Ca/Mg ratio from 12 to 4. However, the XRD pattern of Ca/Mg = 15 specimen possessed the additional broad peaks at 2θ ≈ 31.73° and 32.20°. Additional reflections in the XRD pattern of Ca/Mg = 15 sample have originated due to the presence of CDHA (ICDD #00-046-0905) [108]. It is important to note, that the increase of magnesium concentration in the initial synthesis mixture persuades a shift in the diffraction peaks of analysed samples towards higher diffraction angles, possibly indicating a shrinkage of the crystal lattice of the obtained phases. Figure 13b shows a representative (0 2 10) diffraction peak near 31° which undergoes a clear shift. Since the ionic radius of six-fold coordinated Ca^{2+} is 1.00 Å and the ionic radius of six-fold coordinated Mg^{2+} ion is 0.72 Å, thereby increased magnesium concentration results in a decrease of the interplanar spacing between the lattice planes of

WH crystal and consequently leads to the shift in the diffraction peaks from $2\theta = 31.30°$ (for Ca/Mg = 4) to $2\theta = 31.11°$ (for Ca/Mg = 15) [109].

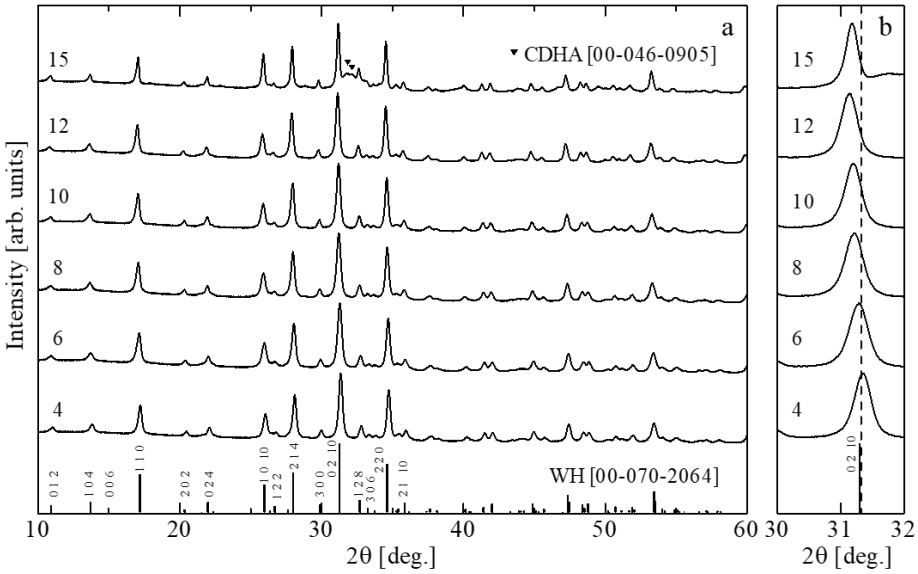

Figure 13. a) XRD patterns of synthesized Ca/Mg = 4, 6, 8, 10, 12, and 15 samples; b) enlarged view of (0 2 10) diffraction peak.

In order to determine the structural parameters more accurately, the Rietveld refinement of XRD data of the single-phase Mg-WH samples (Ca/Mg = 4, 6, 8, 10, and 12) was performed using *FullProf* program, in which rhombohedral $Ca_{18}Mg_2(HPO_4)_2(PO_4)_{12}$ with R3c space group (#161) was taken as a starting model [36]. Figure 14 a and b depict the graphical representation of the lattice parameters plotted against the Ca to Mg molar ratio in the initial reaction solution, and of Mg/(Mg + Ca) in the synthesized samples as calculated from occupancy sites, respectively [110]. Obviously, as the concentration of magnesium in the initial synthesis mixture increased the a and c lattice parameters decreased, thus confirming higher magnesium content within WH structure [110,111]. The cell parameters revealed a monotonous increase along with an increase of Ca/Mg ratio indicating that lattice expands without influencing the symmetry of the crystal. The evaluated Ca/Mg molar ratio in the synthesized Mg-WH powders as well as lattice parameters are summarized in Table 2.

According to the obtained results, it is evident, that magnesium added to the initial synthesis mixture is not fully incorporated within the synthesized structure. Excessive magnesium probably was washed out during the sample

preparation as the determined Ca/Mg molar ratios were found to be higher than the initial ones. The results show that Ca/Mg ratio within the synthesized WH structure decreased from 17.6 (Ca/Mg = 12 sample) to 9.0 (Ca/Mg = 4), and at the same time molar percentage of magnesium increased from 5.3 (Ca/Mg = 12) to 10 (Ca/Mg = 4) for the same samples.

The crystallite sizes of the synthesized phases were calculated from the broadening of the well-resolved (0 2 10) diffraction peak by Scherrer's formula, $d = 0.9\,\lambda/(B\cdot\cos\theta)$, where λ is the X-ray wavelength, B is defined as the full width of the peak from the intensity distribution pattern measured at half of the maximum intensity value and θ is the Bragg angle [112]. The crystallite sizes of the samples, as determined from x-ray line broadening, ranged from 29 nm for Ca/Mg = 15 sample to 25 nm for Ca/Mg = 4 sample. These results confirm our assumption that WH nanocrystallites were synthesized by the proposed dissolution-precipitation synthesis method.

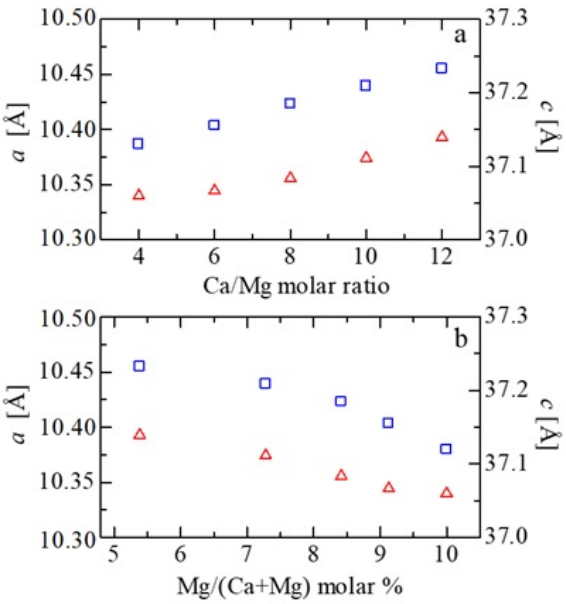

Figure 14. a) Lattice parameters *a* (red triangles) and *c* (blue squares) extracted from XRD pattern refinements versus the Ca to Mg molar ratio in the initial reaction solution; b) lattice parameters *a* (red triangles) and *c* (blue squares) extracted from XRD pattern refinements versus the Mg/(Mg + Ca) molar % in the synthesized samples.

Table 2. The results of structural refinement of Ca/Mg = 12, 10, 8, 6 and 4 samples.

Initial Ca/Mg molar ratio	Determined Ca/Mg molar ratio	Determined Mg/(Ca+Mg) molar %	*a*, Å	*c*, Å
4	9.00(0)	9.99(9)	10.3401(1)	37.1301(1)
6	9.95(5)	9.12(9)	10.3445(8)	37.1554(3)
8	10.8(8)	8.41(6)	10.3558(6)	37.1847(1)
10	12.7(4)	7.27(9)	10.3743(2)	37.2090(4)
12	17.5(7)	5.38(4)	10.3930(8)	37.2326(7)

The Ca/Mg molar ratio in the synthesized WH powders as well as the magnesium molar percentage calculated from the results of ICP-OES analysis are summarized in Table 3. According to the chemical analysis of the single-phase samples WH (Ca/Mg = 4, 6, 8, 10, and 12) it is evident, that magnesium added to the initial synthesis mixture is not fully incorporated within the synthesized structure. The results of the analysis show that the amount of Mg^{2+} ions within the synthesized samples increases from 8.74 (Ca/Mg = 12 sample) to 15.8 (Ca/Mg = 4 sample) molar percent even though the XRD data indicate that the samples synthesized are phase-pure. It suggests that some secondary magnesium-containing CP phase might be present, however, it is amorphous, or its amount is insignificant, below the level of detection by XRD.

Table 3. The results of ICP-OES analysis of Ca/Mg = 4, 6, 8, 10, and 12 samples.

Initial Ca/Mg molar ratio	Determined Ca/Mg molar ratio	Determined Mg/(Ca+Mg) molar %
4	5.33	15.8
6	6.06	14.2
8	6.53	13.3
10	7.82	11.3
12	10.4	8.74

FT-IR spectroscopy is a widely used technique, as it provides information on the presence of particular phases or structural groups within inorganic materials [113]. The FT-IR spectra of synthesized Ca/Mg = 4, 6, 8, 10, 12, and 15 samples are shown in Figure 15. The broad absorption band in the region of 1200 – 800 cm^{-1} is composed of several overlapping peaks. To find an exact peak position, FT-IR spectra have been deconvoluted into distinct peaks using

Gaussian distribution. The spectra in the $\nu_{3,1}$ PO_4^{3-} stretching domains have no obvious difference between all the measured samples and exhibit bands at 1135, 1097, 1066, 1011, 987 and 960 cm^{-1}, which are consistent with the ones detected by Jang *et al*. [114]. The 930 – 800 cm^{-1} region was resolved to three components at 913, 884 and 860 cm^{-1} for Ca/Mg = 10, 12, 15 samples, and two components at 919 and 891 cm^{-1} for Ca/Mg = 4, 6, 8 samples.

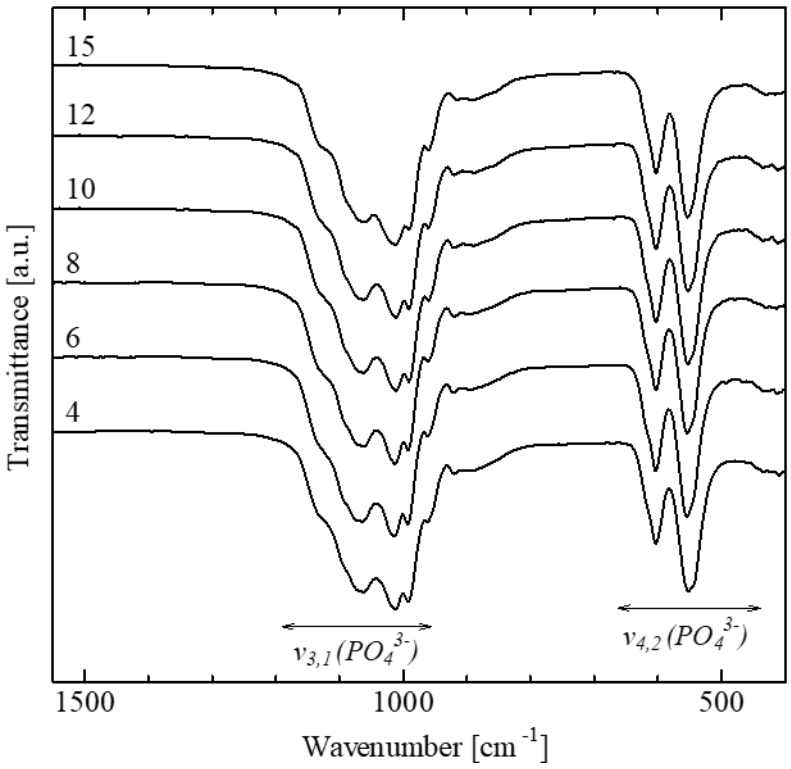

Figure 15. FT-IR spectra of synthesized Ca/Mg = 4 – 15 samples.

The aforementioned bands are assigned to the vibrations of P–O–H bond in the protonated phosphate group. A peak at 919 cm^{-1} is a typical stretching mode of P–O–H bond in the WH structure [36,114,115]. It is interesting to note, that for Ca/Mg = 15 sample this band is shifted to lower wavenumbers, namely to 913 cm^{-1}, due to the presence of CDHA phase, clearly detected by XRD analysis for Ca/Mg = 15 sample, and suggested by the appearance of a band at 860 cm^{-1} (Figure 16). Moreover, Ca/Mg = 15 sample has an additional component at 1175 cm^{-1} which also confirms the presence of CDHA [116]. In the FT-IR spectrum of carbonated hydroxyapatite, the carbonate peaks at 880 – 870 cm^{-1} are assigned to the A- (879 cm^{-1}) and B- (873 cm^{-1}) types

carbonated hydroxyapatite [5,113]. The absence of any bands in the range of 1400 – 1550 cm^{-1} indicates that our synthesized samples do not contain any carbonated hydroxyapatite and the peaks observed around 884 cm^{-1} (for Ca/Mg = 10, 12, 15 samples) and at 891 cm^{-1} (for Ca/Mg = 4, 6, 8 samples) could be assigned to the P–O–H bond of HPO_4^{2-} rather than to the carbonate vibration. It is worth mentioning that the bands (884 cm^{-1} and 891 cm^{-1}) might be related to monetite [117], however, XRD did not show any signs of this phase. The absorbances at low wavenumbers 640 – 500 cm^{-1} and 430 cm^{-1} correspond well to the phosphate $\nu_4(PO_4^{3-})$ and $\nu_2(PO_4^{3-})$ bending modes, respectively [118].

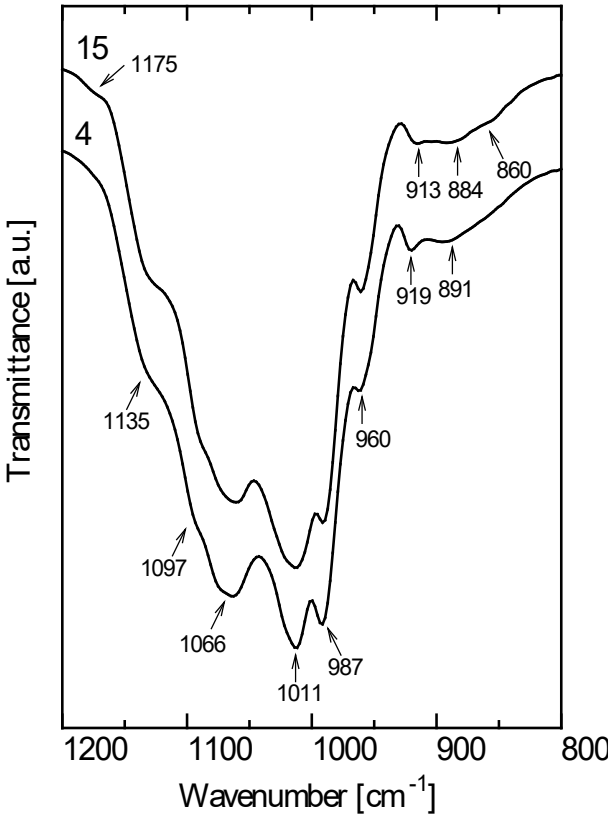

Figure 16. FT-IR spectra in the 1200 – 800 cm^{-1} spectral region for the synthesized Ca/Mg = 4 and 15 samples, enlarged for visual clarity.

The SEM micrographs of synthesized whitlockite samples having various Ca to Mg molar ratios are presented in Figure 17. As was expected, the surface morphology of the end products depends on the magnesium

content in synthesized Mg-WH [30]. In general, Figure 17 shows the appearance of rhombohedral, hexagonal, and spherical nanoparticles with particle sizes of 10 – 100 nm. These results are remarkably similar to the results obtained recently by Konishi and Watanabe [119]. The surface of Ca/Mg = 15 sample also contains the particles which exhibit a rod-like morphology, which also confirms the presence of CDHA (Figure 17 a, and e). The formation of monodisperse rhombohedral WH particles with a size of about 150 nm is evident for the sample Ca/Mg = 12 (Figure 17 b, and f). However, rhombohedral nanoparticles (less than 20 nm) have formed in the case of the Ca/Mg = 4 specimen (Figure 17 d, and h). So, with an increasing amount of Mg, the monotonous decrease in particle size can be observed. These results appear contradict to the ones obtained by the XRD analysis method. However, it is very well known that XRD shows the crystallite size, but SEM shows the particle size, making the size comparison problematic [120]. Such difference could be also caused by the fact that some fields of the micrographs contain freely associated aggregates which are covered by a thin layer of amorphous material (Figure 17 d, and h). The SEM images of Mg-WH nanoparticles with different amounts of magnesium given in Figure 17 (a-h), also show more irregular structures with various levels of agglomeration. And the level of agglomeration with increasing amount of magnesium in the structure increases significantly. In addition, the porous structure was observed in the SEM images depending on the amount of magnesium, causing the grain growth due to diffusion of grain boundaries and Ostwald ripening [33]. The larger aggregates of tiny particles and the aggregates did not possess any definite shape. The formation of porous agglomerates (or mixtures of particles of varied sizes), where each agglomerate is an assembly of numerous distinguishable particles makes the SEM results slightly different from XRD measurements as well [121]. Finally, Scherrer equation is a rough approximation. The Guinier model deviated slightly from Scherrer's formula and analytical models including a size-dependent term [122,123].

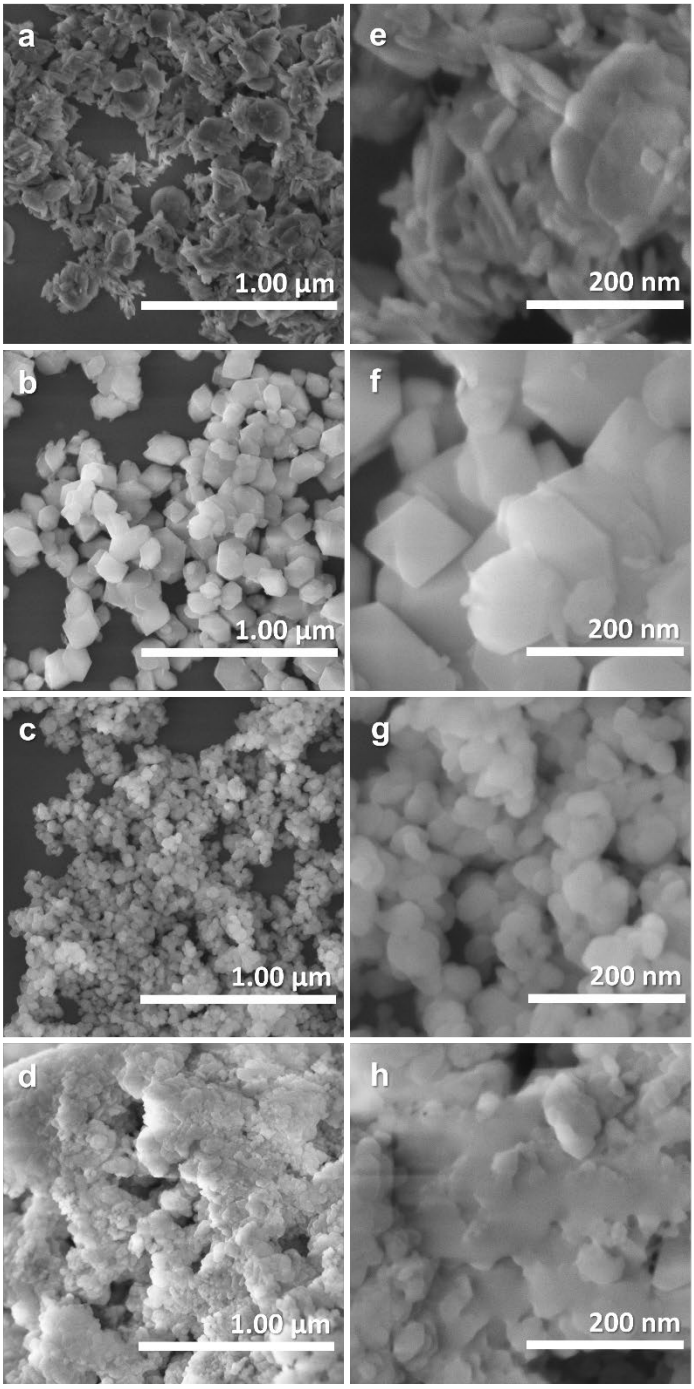

Figure 17. SEM images of the synthesized powders prepared at various Ca to Mg molar ratio in the initial reaction solution: (a), (e) Ca/Mg = 15; (b), (f) Ca/Mg = 12; (c), (g) Ca/Mg = 8; and (d), (h) Ca/Mg = 4.

The more accurate size of individual particles was determined using TEM. The TEM images of synthesized whitlockite samples having various Ca to Mg molar ratios are presented in Figure 18. From the micrograph presented in Figure 18a it is obvious that Ca/Mg = 15 sample consists of two phases as already has been confirmed by XRD and SEM results. The size of hexagonal whitlockite particles varies in the range of 30 – 230 nm (the average size is 120 nm), in contrast, CDHA showed rod-like particles of the mean value of 45 nm. The formation of hexagonal and rhombohedral particles with a size of approximately 110 nm (the size of individual particles varies in the range of approximately 22 – 230 nm) is evident for the sample Ca/Mg = 12 (Figure 18b). As was expected, the shape and the size of the particles of the end products depend on the magnesium content in synthesized WH. With increasing of the amount of magnesium added to the initial synthesis mixture the resultant particles of irregular, undefined shape became smaller, and their size distribution appeared narrower (see Figure 18 c and d for Ca/Mg = 8, Ca/Mg = 4 samples, respectively). TEM micrograph of Ca/Mg = 8 sample (Figure 18c) reveals the formation of particles of the mean value of 40 nm (the size of individual particles varies in the range of 10 – 70 nm), while for Ca/Mg = 4 sample (Figure 18d) discloses particles of approximately 30 nm (the size of individual particles varies in the range of 15 – 60 nm).

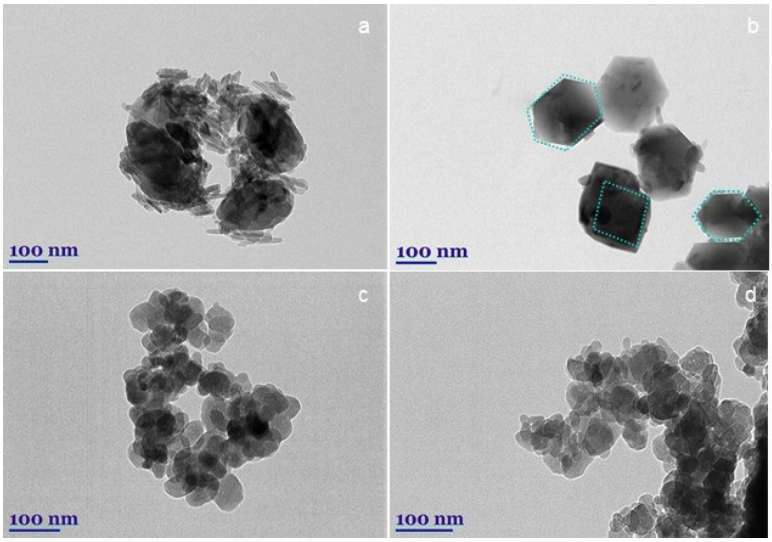

Figure 18. TEM images of the synthesized powders prepared at various Ca to Mg molar ratio in the initial reaction solution: (a) Ca/Mg = 15; (b) Ca/Mg = 12; (c) Ca/Mg = 8; and (d) Ca/Mg = 4.

3.2. Phase transformations during the synthesis of magnesium whitlockite from gypsum under static and rotating conditions

To verify the formation of the Mg-WH phase under static and rotating conditions in time, we gradually increased the reaction time while keeping the synthesis temperature constant at 80 °C. The phase formation was monitored by comparing powder XRD patterns obtained for samples synthesized for 4 h, 6 h, 12 h, and 24 h (Figure 19 represents Mg-WH phase formation under static conditions and Figure 20 under rotating conditions).

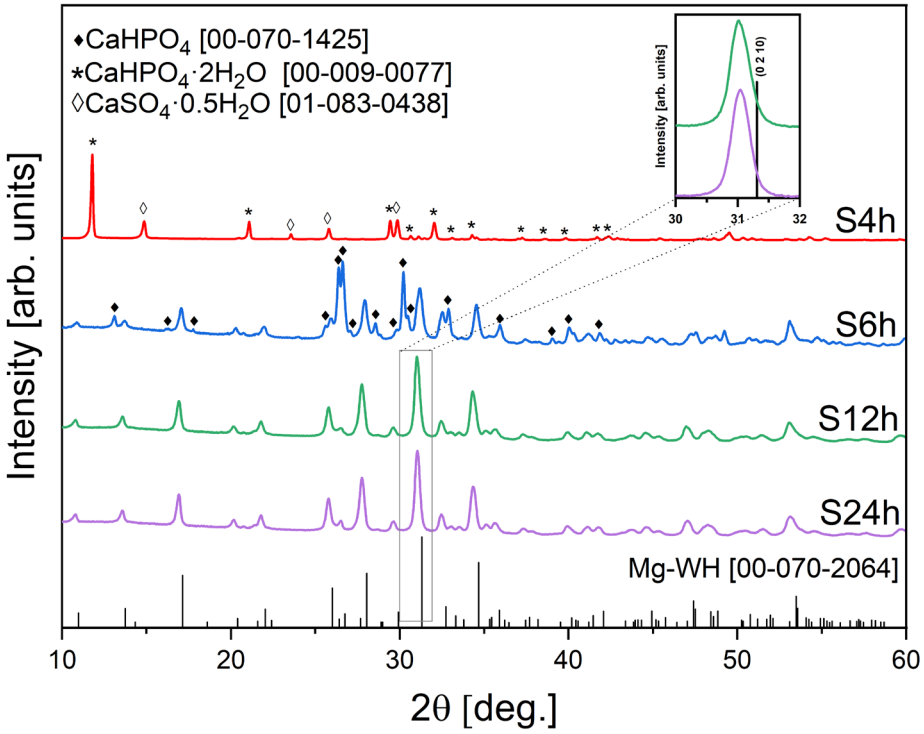

Figure 19. XRD patterns of samples synthesized with different reaction times under static conditions. The vertical lines at the bottom represent reflections of the standard XRD pattern of Mg-WH according to ICDD #00-070-2064. The insets show enlarged views of the (0 2 10) diffraction peak of the S12h and S24h samples.

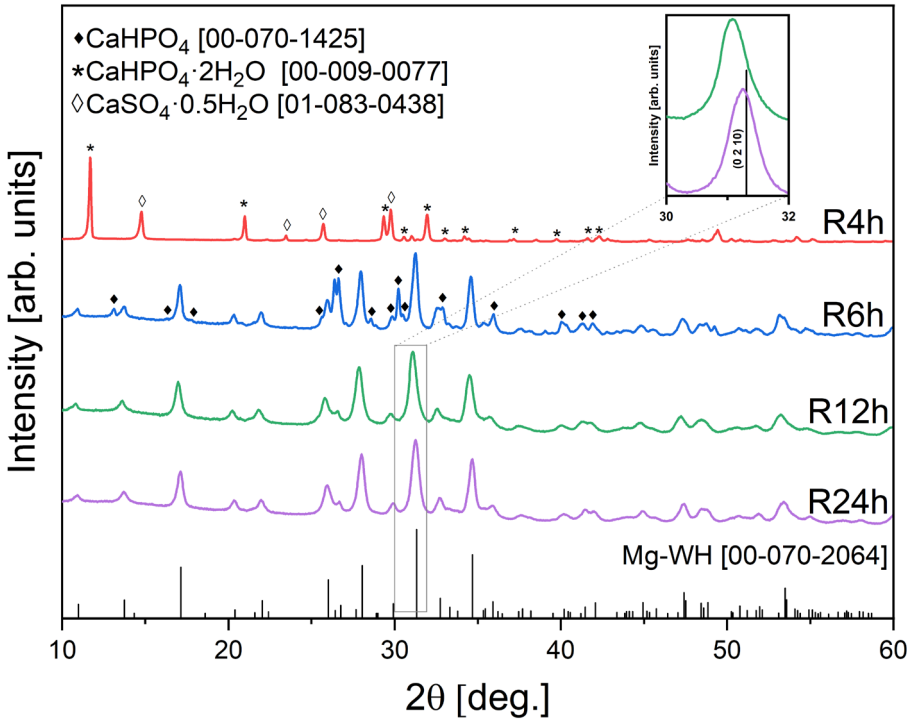

Figure 20. XRD patterns of samples synthesized with different reaction times under rotrating conditions. The vertical lines at the bottom represent reflections of the standard XRD pattern of Mg-WH according to ICDD #00-070-2064. The insets show enlarged views of the (0 2 10) diffraction peak of the R12h and R24h samples.

The XRD patterns of the samples synthesized for 4 h independently of static and rotating conditions correspond to a mixture of CSH (ICDD #01-083-0438) and $CaHPO_4 \cdot 2H_2O$ (ICDD #00-009-0077). The formation of CSH is related to the dehydration of gypsum rather than its dissolution, since gypsum is less soluble than CSH even at elevated temperatures (the solubility of the precursor should be higher than that of the precipitated product) [30]. Meanwhile, the precipitation of DCPD occurs at the expense of the dissolution of CSH (for the Ca^{2+} ions to be supplied) and the hydrogen phosphate ions already present in the reaction solution. DCPD, which is an acidic CP, is often used as a starting material in the preparation of CP-based materials [124,125]. At around neutral pH it is a metastable phase. According to Ostwald's rule of stages, the first crystallises the least stable phase, which then transforms to a more stable one [126]. Consequently, in aqueous medium DCPD usually transforms stable CP, that is HAp, OCP or a mixture of these, and therefore it

must also be additionally stabilized to prevent crystallization of unwanted phases. Here, we should emphasise that the presence of magnesium ions in the reaction solution prevents DCPD from transforming into those thermodynamically stable undesirable CPs even when exposed to elevated pH conditions [127].

As the reaction progressed further, the second significant change in the product composition was observed after 6 h, both for static and rotating synthesis conditions. The XRD peaks corresponding to the anhydrous form of calcium hydrogen phosphate (DCPA, $CaHPO_4$; ICDD #00-070-1425) and to the WH phase (ICDD #00-070-2064) were detected in the resulting sample. Highly soluble DCPD was transformed into DCPA, which, in turn, was partially converted into the WH [128]. The formation of an acidic DCPA phase in the sample treated for 6 h probably caused a decrease in the pH of the reaction solution ($Ca^{2+}(aq) + H_2PO_4^-(aq) \rightarrow CaHPO_4(s) + H^+(aq)$ [129,130]) and it became suitable for the precipitation of the Mg-WH phase, as it is well known that the Mg-WH phase precipitates under magnesium-rich and acidic pH conditions [89]. The percentages of the DCPA and Mg-WH phases identified in the XRD pattern in sample synthesized for 6 h were determined using the RIR method. The S6h sample consisted of 60 wt.% DCPA along with 40 wt.% WH. The R6h sample qualitatively comprises the same constituents; however, the Mg-WH phase was the main (55 wt.%) along with the DCPA component (45 wt.%). Thus, rotation accompanied by mixing the reaction suspension facilitated the solubility of the starting and intermediate products. The rotating conditions probably influenced the crystal size of the obtained materials, resulting in more reactive intermediate products, which caused different rates of Mg-WH phase formation.

Eventually, when the reaction time was extended to 12 h, according to the XRD patterns the DCPA phase disappeared from both analysed samples and the peaks attributable to Mg-WH became dominant. As Gopal *et al.* first deduced, Mg-WH crystallises in a rhombohedral crystal lattice that adopts the symmetry of R3c (# 161) (Z=6), with lattice parameters of $a = b = 10.350(5)$ Å, $c = 37.085(12)$ Å and $\alpha = \beta = 90°$, $\gamma = 120°$ [40,131]. All experimental XRD peaks shown in Figure 19 for the sample S12h and in Figure 20 for R12h were allowed Bragg 2θ positions for the mentioned above space group, suggesting that the samples possess WH structure. Therefore, using the described synthesis procedure, single-phase WH structure samples S12h and R12h were attained. It should be noted here that a careful inspection of the XRD pattern revealed some 2θ mismatch between the observed peaks of the S12h and R12h samples and the standard. All peaks of synthetized powders

are shifted to the lower 2θ angles. The expanded view of the XRD patterns with reflection from the most intense (0 2 10) plane is shown as insets in Figures 19 and 20. For the S12h sample, the aforementioned reflection emerged at 2θ = 31.01°, for R12h at 2θ = 31.07°, while the strongest line of the standard appears at 2θ = 31.31°. The shift of the diffraction peak toward the lower angle implies a difference in the crystal interplanar spacing of prepared samples from those of the standard, indicating the possibility of the cation distribution in the crystal lattice of the measured samples being different from that of the standard.

To see whatever ageing affects the purity, morphology and structural parameters of the obtained Mg-WH phase, we prolonged the synthesis time for additional 12 h. The diffraction patterns of the 24 h samples did not present any peaks, which could be ascribed to other than the Mg-WH crystalline phases. The expanded view of the XRD patterns with reflection from the most intense crystallographic plane (0 2 10) is shown in the insets in Figure 19 and 20. For the sample S24h, the aforementioned diffraction line emerged at 2θ = 31.04°, for R24h at 2θ = 31.26°. It should be noted that the diffraction peaks in the XRD patterns of all single-phase Mg-WH samples are broadened, indicating the nanocrystalline nature of the prepared materials.

The structure of WH was shown to allow for some variations in the Ca to Mg ratios. Therefore, solid solutions with some degree of substitution are possible for this CP material [132]. In [132], it was shown that the *a* and *c* lattice parameters of the prepared Mg-WH samples increased with an increase in the molar Ca to Mg ratio in the initial reaction solution or with a decrease in the magnesium content in the structure of the WH. Therefore, the substitution of Ca by Mg causes lattice contraction of the synthesized CP material. This result is reasonable since the ionic radius of Mg^{2+} (0.72 Å) is smaller than that of Ca^{2+} (1.00 Å) in the same six-fold coordination. In the present work, to confirm the purity of the synthesized samples, and to assess their structural parameters more closely, Rietveld refinement of the S12h, R12h, S24h, and R24h samples was carried out using the *FullProf* software (Figure 21 illustrates the refinement pattern of S12h sample).

A successful structure refinement was achieved by setting additional Ca^{2+} at the magnesium octahedral *6a* Wyckoff position [90]. During refinement, Ca and Mg were allowed to vary at the co-occupied site, with the restriction of producing a stoichiometric composition of the sample (the sum occupancy of Ca and Mg at the shared site was set equal to 0.33334). The deduced structural and microstructural data are summarized in Table 4 (the refined atomic positions, site occupancies for S12h sample are listed in Table 5).

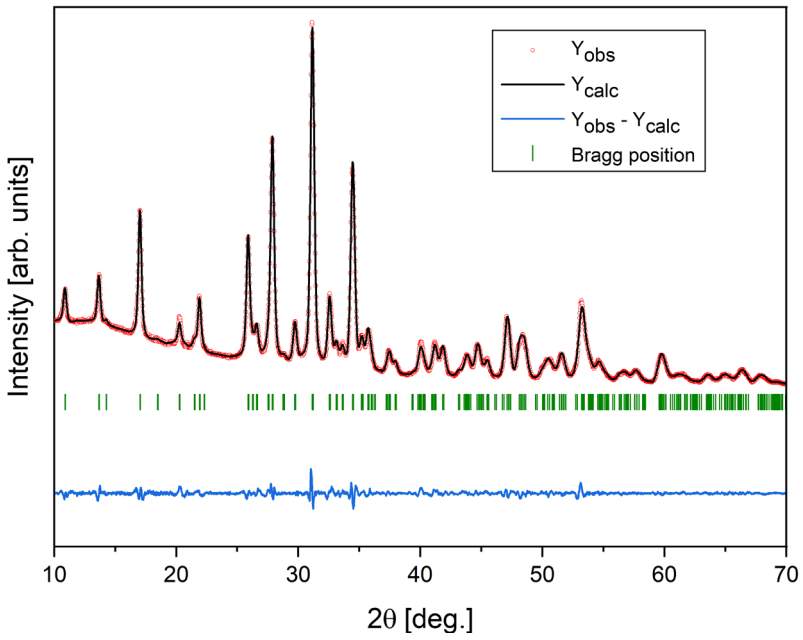

Figure 21. The Rietveld refinement plot of the S12h sample.

Table 4. Structural, R-values, χ^2 and microstructural data elucidated from XRD for S12h, S24h, R12h and R24h samples.

Sample	**S12h**	**S24h**	**R12h**	**R24h**
a, Å	10.406(7)	10.397(2)	10.352(6)	10.351(9)
c, Å	37.216(9)	37.178(8)	37.170(7)	37.151(2)
Cell volume, Å^3	3490.5(6)	3480.5(9)	3450.1(1)	3447.7(9)
Occ (Ca)	0.167(3)	0.138(4)	0.037(7)	0.021(4)
Occ (Mg)	0.166(3)	0.195(4)	0.295(7)	0.312(4)
R_p	2.61	2.38	2.05	2.45
R_{wp}	3.42	3.16	2.64	3.20
χ^2	2.84	2.40	1.71	2.54
Cristalite size, nm	30	30	16	22
Cristallinity (amorphisity), %	61 (39)	67 (33)	54 (46)	58 (42)

Table 5. Rietveld refinement data of the S12h sample: crystallographic site, Wyckoff position (W.p.), atom coordinates (*x*, *y*, *z*), site occupancy (s.o.).

Atom	W.p.	*x*	*y*	*z*	s.o.
Ca1	*18b*	0.38036(7)	0.18316(9)	0.00223(3)	1
Ca2	*18b*	0.81718(9)	0.20312(6)	0.89728(2)	1
Ca3	*18b*	0.60995(5)	0.78361(9)	0.96871(4)	1
Ca4	*6a*	0	0	0.92495(15)	0.019
Ca5	*6a*	1/3	2/3	0.90217(5)	0.167(3)
Mg6	*6a*	1/3	2/3	0.90217(5)	0.166(3)
P7	*6a*	0	0	0.97969(4)	0.281
P8	*6a*	0	0	0.0025*	0.052
P9	*18b*	0.68522(3)	0.83640(7)	0.86759(1)	1
P10	*18b*	0.53211(4)	0.01990(5)	0.93212(2)	1
O11	*6a*	0	0	0.92970(9)	0.281
O12	*6a*	2/3	1/3	0.87488(15)	0.052
O13	*18b*	0.72472(19)	0.82503(18)	0.91191(7)	1
O14	*18b*	0.72540(25)	0.73849(26)	0.84955(5)	1
O15	*18b*	0.75276(26)	0.98177(25)	0.85848(5)	1
O16	*18b*	0.52094(13)	0.75121(34)	0.86985(4)	1
O17	*18b*	0.43808(24)	0.85440(15)	0.94517(4)	1
O18	*18b*	0.44360(27)	0.09405(22)	0.95336(5)	1
O19	*18b*	0.67129(26)	0.06290(20)	0.94558(7)	1
O20	*18b*	0.54139(27)	0.07761(17)	0.98703(4)	1
O21	*18b*	0.12573(14)	0.99081(16)	0.99450(4)	1

* restrained value

The analysis of the data indicates that the lattice parameters, magnesium site occupancy (theoretically it is 0.33334 for $Ca_{18}Mg_2(HPO_4)_2(PO_4)_{12}$, as Z = 6), and lattice volume changed only marginally, while the synthesis time was extended to 24 h. Both synthesis methods resulted in some extraction of Ca atoms from the WH structure when synthesis time was prolonged as evidenced by the reduction in unit cell volumes and the decreased refined Ca occupancies

at the Mg site. It is important to note that these parameters exhibit significant differences when samples synthesized under disparate conditions are being compared, those synthesized under static *vs.* rotating conditions. Notably, rotating synthesis conditions were more effective in producing Mg-rich samples (compare S12h and R12h). As can be seen from the results presented in Table 4, the single-phase Mg-WH samples prepared using static conditions for 12 h and 24 h composed of 30 nm crystallites (Figure 22 illustrates the Le Bail refinement pattern of S12h sample), the degrees of crystallinity of which are 61 % and 67 %, respectively. Regarding the size of crystallites, the increased size should be the result of the longer processing time that allows continuous growth of nanocrystals [133]. However, the kinetics of the dissolution-precipitation reaction on the surface of small particles is rather complicated [134]. Depending on the coverage of the particle surface by the new phase, the reaction kinetics could exhibit high- and low-rate regimes. This probably could be the reason for the absence of an apparent grow of crystallites by increasing the reaction time using the static synthesis regime. Synthesis under static conditions (apparently occurring without mixing) resulted in a larger particle size and higher crystallinity (see Table 4) because the growth rate of these particles exceeded their nucleation rate [135]. Although the reaction rate under static conditions was found to be lower compared to those prepared under rotating conditions (see Figure 19 for S6h and Figure 20 for R6h), the samples prepared under rotating conditions were made of smaller crystallites, namely 16 nm (12 h synthesis) and 22 nm (24 h synthesis), whose degree of crystallinities is 54 % and 58 %, respectively. No definitive correlation could be established between the magnesium content, the crystallite size, and the crystallinity of the synthetized Mg-WH samples [132]. The difference in crystallite size and crystallinity among the samples is obviously dependent on the synthesis conditions, which gave rise to different rates of the formation of Mg-WH. Meanwhile, nucleation under rotating conditions occurred at a rate higher than that of crystal growth. Consequently, it led to crystallites to become smaller, the order of atomic arrangement, and, therefore, the crystallinity to become lower in both samples synthesized under rotating synthesis conditions. Here, it should be emphasized, that the variation and control of crystallinity might be achieved by selecting a synthesis setup.

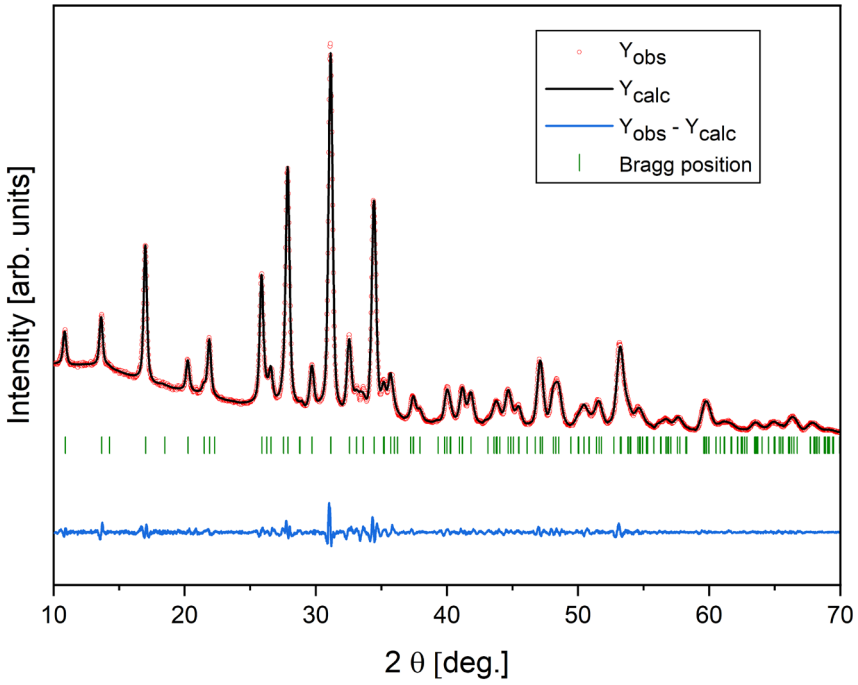

Figure 22. The Le Bail refinement plot of the S12h sample. Vertical green bars represent the peak positions of Mg-WH phase.

For functional group investigation, FT-IR spectroscopy was used as a complementary technique to XRD. FT-IR spectra show that samples S4h and R4h contain sulphate (SO_4^{2-}), phosphate (PO_4^{3-}), and hydrogen phosphate (HPO_4^{2-}) ions (see Figure 23 for the samples obtained under static conditions, and Figure 24 for the samples obtained under rotating conditions) [136–138]. The bands located at approximately 1150 – 1090 cm^{-1} belong to ν_3 stretching modes of the SO_4^{2-} and PO_4^{3-} groups present in the crystal structure of the CSH and DCPD phases. The bands at 1006 cm^{-1} and 985 cm^{-1} correspond to ν_1 of the S–O and P–O bands of the aforementioned groups. Meanwhile, absorptions centred at 872 cm^{-1} and 789 cm^{-1} could be assigned to the stretching vibration of the P–O(H) and P–O–H out-of-plane bending modes of the HPO_4^{2-} group present in the structure of DCPD, respectively [139]. Bands in low wavenumbers of 660 – 595 cm^{-1} and 463 cm^{-1} correspond well to the ν_4 and ν_2 modes of the S–O bond of the SO_4^{2-}, respectively, while a shoulder at 574 cm^{-1}, and a band at 522 cm^{-1} are associated with the bending mode of the HPO_4^{2-} group in the structure of DCPD [140].

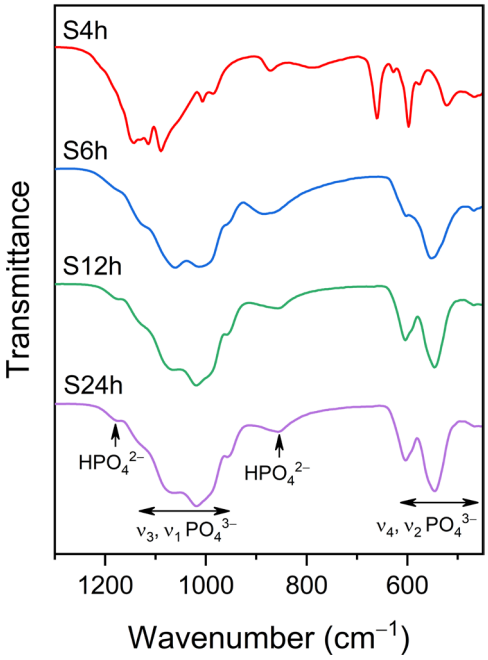

Figure 23. FT-IR spectra of samples synthesized with different reaction time under static synthesis conditions.

The FT-IR spectra of the samples prepared for 6 h regardless of synthesis conditions contain only absorption band characteristic of the PO_4^{3-} and HPO_4^{2-} groups. There is no sign of a sulphate group anymore in the samples obtained. It is apparent from the spectra that as a result of prolonged synthesis time, the phase composition of obtained samples was changed to possess clearly distinct absorption. It complements the evidence on the presence of two crystalline CP phases, namely DCPA and Mg-WH, detected by XRD analysis (see Figure 19, and Figure 20). The peaks at 1130 cm^{-1}, 1068 cm^{-1}, 1015 cm^{-1}, and a shoulder at 1010 cm^{-1} represent ν_3, while the band at 954 cm^{-1} corresponds to ν_1 vibrations of the PO_4^{3-} group in the crystal structure of the DCPA and Mg-WH [141,142]. The band at 1190 cm^{-1} could be related to the bending mode of P–O(H) originating from the HPO_4^{2-} group present in Mg-WH [141]. It is interesting to note that the FT-IR spectrum of S6h sample has a rather broad band with the two maxima at 887 cm^{-1} and 866 cm^{-1} attributable to the stretching vibration of the P–O(H) bond of the HPO_4^{2-} group [128,143]. This is because there are two different crystallographic environments of hydrogen phosphate ion within the biphasic sample (the S6h sample consisted of 60 wt. % of DCPA along with 40 wt.% of Mg-WH phase, while the R6h sample consisted of 45 wt.% of DCPA and 55 wt.% of Mg-WH

component) of the higher crystallinity than the one obtained under rotating conditions. The absorbances at 602 cm^{-1}, 550 cm^{-1} and 465 cm^{-1} correspond to the ν_4 (P–O) and ν_2 (O–P–O), of the PO_4^{3-} and HPO_4^{2-} groups, respectively [128,141].

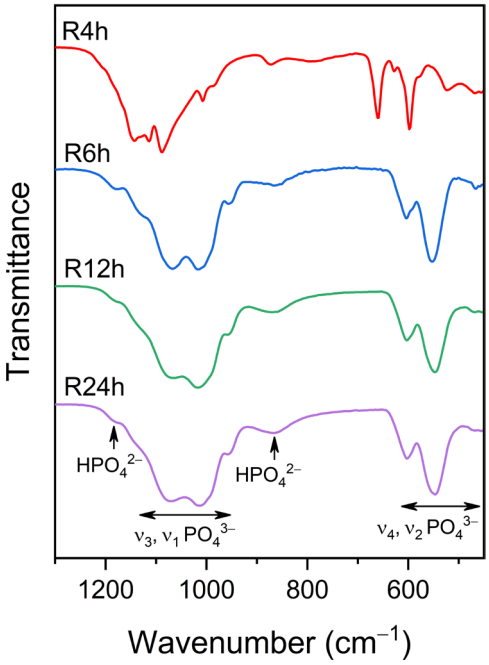

Figure 24. FT-IR spectra of samples synthesized with different reaction time under rotating synthesis conditions.

The formation of single-phase Mg-WH in the samples synthesized for 12 h and 24 h is further supported by FT-IR spectra showing that samples contain only the PO_4^{3-}, and HPO_4^{2-} groups. The band at 1190 cm^{-1} could be related to the bending mode of the P–O(H) bond present in the structure of Mg-WH [141,142]. Peaks at 1130 cm^{-1}, 1068 cm^{-1}, 1015 cm^{-1}, 1010 cm^{-1} (a shoulder) and 954 cm^{-1} arise from the various stretching vibrations of the P–O bonds (ν_3 and ν_1, respectively). Bands at 604 cm^{-1}, 550 cm^{-1} and 465 cm^{-1} are due to bending ν_4 of the P–O bond and ν_2 (O–P–O) vibration, respectively, present in the PO_4^{3-}, and HPO_4^{2-} groups [128,141,142]. The broad band centred at 868 cm^{-1} represents the stretching of the P–O(H) bond present in the crystal structure of Mg-WH [128]. It can be observed that the spectra of the samples obtained under static conditions are more expressed, representing a higher crystallinity of the samples [144,145]. In contrast, the rounded bands of the samples obtained under rotating conditions may be attributed to a decrease in

the crystallite size and an enhancement of the crystal structure disorder, in agreement with the results of the powder XRD.

The SEM micrographs of S4h − S24h and R4h − R24h samples obtained during the low-temperature synthesis of Mg-WH nanopowders under different conditions are presented in Figure 25.

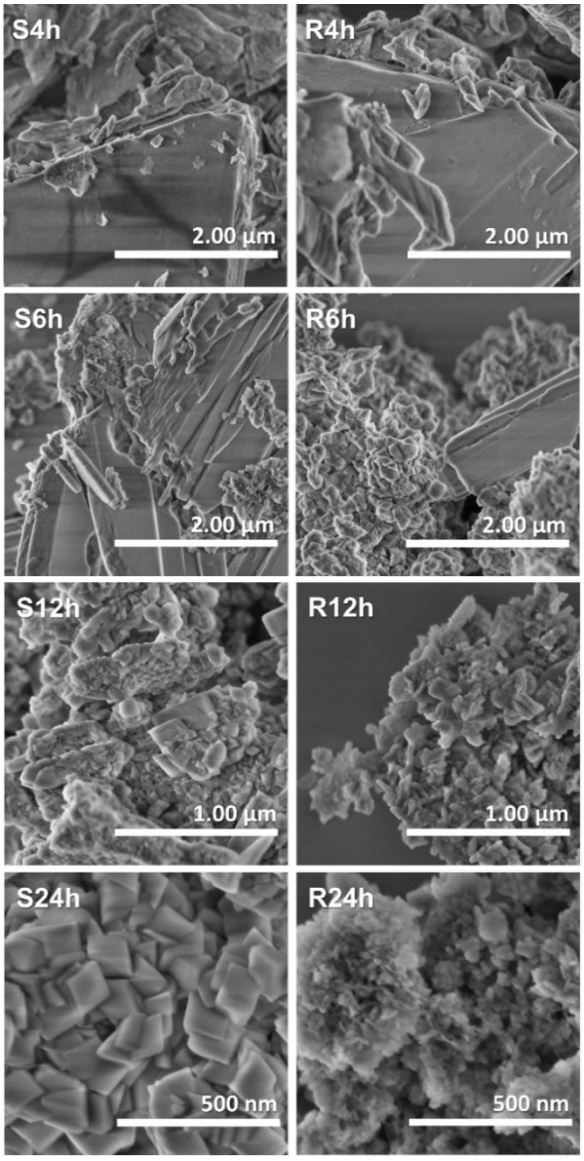

Figure 25. SEM images of samples synthesized with different reaction time under static conditions for S4h, S6h, S12h, and S24h, and rotating synthesis conditions for R4h, R6h, R12h, and R24h.

The microstructure of the obtained samples is influenced by their phase composition, selected synthesis conditions, and reaction time. Observing the micrographs, it is evident that the S4h, S6h, R4h, and R6h samples consist of two distinct phases, as they exhibit two different types of particles. In the S4h sample, large plate-like crystals of DCPD with a smooth surface are observed, ranging in size from approximately 2 to 3 μm. These platy crystals are found to be covered by smaller volumetric particles of CSH that possess a rough surface [143,146]. The S6h sample displays tiny volumetric particles of Mg-WH along with plate-like crystals of DCPA [24,132,147].

Upon increasing the synthesis time to 12 hours, the morphological features of the S12h sample undergo significant changes. The plate-like crystals disappear, and rhombohedral particles of Mg-WH with varying levels of agglomeration become predominant, ranging in size from 25 to 350 nm. The morphology of the S24h nanopowder, obtained under the same conditions, remains largely unchanged; however, the level of particle agglomeration and particle size (ranging from 30 to 350 nm) increases. In static conditions, particles have a higher tendency to agglomerate or cluster together, leading to the formation of larger crystals instead of individual particles. Moreover, initially, the S12h sample shows a distribution of particles with varying sizes, including both small and large Mg-WH nanoparticles. SEM images disclose an increase in the size of Mg-WH particles for the S24h sample might be attributed to the Ostwald ripening – a phenomenon observed in certain systems where small particles dissolve while larger ones grow over time [148]. Notably, the S24h sample exhibits remarkably smooth nanoparticles with well-defined faces and edges, indicating improved crystal perfection compared to earlier stages of synthesis. This can be attributed to the extended synthesis time, which allows for a more complete reaction, affecting the order of atomic arrangement, and the potential removal of secondary phases. During the synthesis of Mg-WH nanopowders under rotating conditions, the initial stage of the synthetic procedure (sample R4h) resulted in the formation of smooth surface platy crystals of DCPD, which were larger than 3 μm, along with rough surface volumetric particles of CSH. The R6h sample exhibited tiny volumetric particles of Mg-WH in addition to plate-like crystals of DCPA [24,132,147]. Upon extending the treatment time to 12 hours, the platy crystals of DCPD disappeared, and the Mg-WH rhombohedral particles became the dominant phase under rotating conditions [24,132]. SEM measurements of the R12h sample revealed the formation of particles ranging in size from 15 to 75 nm. As the synthesis time increased further, the morphology of the Mg-WH particles and their degree of

aggregation were maintained, but there was a slight increase (see Table 4) in individual particle size.

In conclusion, the SEM results obtained are consistent with the findings from XRD analysis and FT-IR spectroscopy. Considering these results, a proposed the scheme of the formation of Mg-WH using the dissolution-precipitation method under static and rotating conditions is depicted in Figure 26. The formation of Mg-WH under rotating conditions occurs more rapidly than under static conditions. Additionally, the duration of synthesis does not significantly influence the crystallite size of the synthesized Mg-WH under static conditions. However, the continuous shaking of the reaction vessel during rotating conditions has a significant impact on crystallite growth. According to the XRD and SEM results, both the crystallite and particle size of Mg-WH increase with an increasing synthesis time from 12 h to 24 h when performed under rotating conditions.

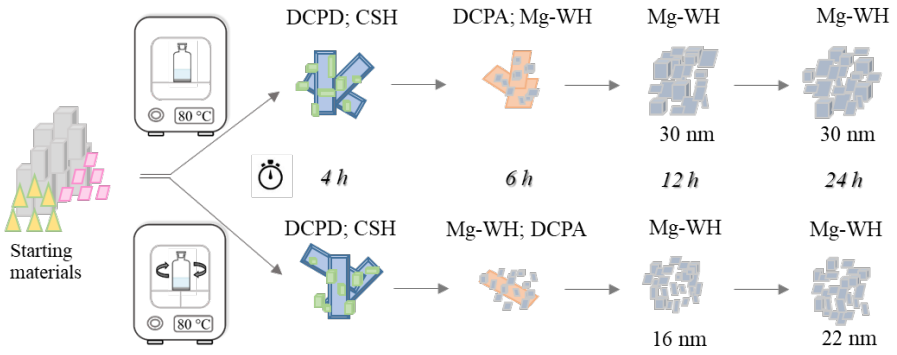

Figure 26. Schematic representation of the formation of Mg-WH nanoparticles using the dissolution-precipitation method under static and rotating conditions.

4. CONCLUSIONS

1. Mg-WH samples with different contents of magnesium (nominal Ca/Mg molar ratio equal to 15, 12, 10, 8, 6, and 4) were successfully synthesized from brushite by a dissolution-precipitation method. The chemical composition, the morphology of synthesized material was adjusted by the Ca/Mg molar ratio in the initial synthesis solution. No other secondary phases due to a varied amount of the Ca^{2+} and Mg^{2+} ions were observed in the XRD patterns of products with Ca/Mg ratio from 12 to 4. However, the presence of a small amount of CDHA was determined in the Ca/Mg = 15 specimen. The lattice parameters *a* and *c* of synthesized compounds increased with increasing the Ca/Mg molar ratio in the initial reaction solution or decreasing the magnesium content in WH structure. The XRD results were fully supported by the FT-IR spectroscopy results. SEM imaging showed a dependence of surface morphology on magnesium content, while TEM analysis revealed variations in particle size and shape with magnesium content.

2. The formation of Mg-WH powder during the environmentally friendly dissolution-precipitation synthesis at 80 °C under static and rotating conditions was elucidated. It was found that the target phase was derived from an initial powder of gypsum through formation of several intermediate products within 12 h. The FT-IR spectra confirmed the presence of sulphate, phosphate, and hydrogen phosphate groups in the early stages of synthesis, while the characteristic bands of the Mg-WH phase became predominant as the synthesis progressed. The synthesis under rotating conditions favors formation of smaller (16 nm) Mg-WH crystals with respect to the sample synthesized under static conditions (30 nm). Rietveld refinement of the 12 h and 24 h samples confirmed small changes in lattice parameters, magnesium occupancy, and lattice volume; however, the synthesis conditions (static *vs*. rotating) influenced structural parameters as well as the crystallite size and crystallinity of the Mg-WH samples more significantly. The findings demonstrate the influence of reaction time and synthesis conditions on the formation, composition, structural and microstructural parameters of the Mg-WH phase, providing insights into the synthesis procedure and control of the properties of the resulting material.

SUMMARY IN LITHUANIAN

ĮVADAS

Kaulas – tai natūralus nuolat atsinaujinantis 3D organinis-neorganinis nanokompozitas, sudarytas iš kolageno fibrilių ir žemo kristališkumo neorganinių medžiagų nanodalelių. Pagrindinis neorganinis komponentas sudarantis stuburinių mineralizuotą kaulinio audinio dalį yra kalcio deficitinis hidroksiapatitas, kuris iš dalies praturtintas CO_3^{2-}, Mg^{2+}, Sr^{2+}, F^-, HPO_4^{2-} jonais. Nors natūralus kaulas turi stiprų savaiminio atsinaujinimo ir gijimo gebėjimą, yra ligų ir būklių, tokių kaip osteoporozė, navikai, traumos ir kiti veiksniai, galintys sukelti kaulų defektus, viršijančius savaiminį organizmo atsinaujinimo pajėgumą. Tokiems pacientams reikalingas išorinis intervencinis gydymas, padedantis sugydyti ir (arba) atkurti kaulą. Dirbtiniai implantai, kurių struktūrinė ir cheminė sudėtis panaši į natūralaus kaulinio audinio, gali būti perspektyvūs žinduolių kietųjų audinių funkcijų atkūrime, pakeitime, palaikyme arba praturtinime. Šie dirbtiniai pakaitalai gaminami įvairiausių formų: miltelių, granulių, tankių arba porėtų karkasų, bioaktyvių dangų pavidalu. Šios medžiagos kliniškai naudojamos kaip dirbtiniai kaulo pakaitalai dėl jų gebėjimo skatinti naujo kaulo susidarymą palaipsniui pakeičiant kaulo defekto vietoje implantuotą medžiagą. Kalcio fosfatai (CP) yra žinomi kaip puikūs transplantatai, atsižvelgiant į jų puikų biologinį suderinamumą su žmogaus organizmu, kontroliuojamą biologinį skaidumą, osteolaidumą, bioaktyvumą ir kaulinio audinio integraciją į implantą. Todėl regeneracinės medicinos srityje yra didelė sintetinių CP paklausa.

Biologinis CP keramikos elgesys (biologinis skaidumo greitis, osteolaidumas, biologinis aktyvumas) ir mechaninės savybės labai priklauso nuo pasirinkto sintezės metodo, kuris, savo ruožtu, daro įtaką CP fazinei sudėčiai, grynumui, kristališkumui, dalelių dydžiui, morfologijai ir, galiausiai, dirbtinių implantų biomedicininėms savybėms. Dėl šios priežasties sintezės metodo pasirinkimas yra labai svarbus gaminant medžiagas, naudojamas biomedicinoje. Iki šiol buvo atrasta daug aukštatemperatūrių sintezės metodų, leidžiančių susintetinti įvairias CP medžiagas. Tačiau tokiais sintezės metodais pagaminta keramika pasižymi itin aukštu kristališkumu, skirtingai nei žemoje temperatūroje susiformavusio natūralaus kaulo. Be to, kai kurių termiškai nestabilių CP fazių negalima susintetinti aukštoje temperatūroje. Nustatyta, kad biomedžiagos, gautos vykdant sintezę žemoje temperatūroje, pasižymi geresniu biosuderinamumu nei įprastinė biokeramika. Šlapieji cheminės sintezės metodai, pvz.: zolių-gelių, hidroterminė, solvaterminė,

mikroemulsijos ir nusodinimo, leidžia tolygiai pasiskirstyti pradiniams komponentams ir CP medžiagų sintezę vykdyti palyginti žemoje temperatūroje. Žematemperatūris sintezės metodas, naudojamas žemo kristališkumo CP medžiagoms gauti, per fazių transformaciją, pagrįstą tirpinimo-nusodinimo reakcija, yra vienas iš būdų, kaip paruošti biokeramiką, kurios fizikinės ir cheminės savybės būtų panašios į kaulinio apatito savybes. Šiame metode, vyksta laipsniškas pirmtako tirpimas ir norimo produkto nusodinimas. Tirpinimo-nusodinimo sintezė yra atsikartojantis, nebrangus ir aplinkai nekenksmingas metodas. Sintezės procesas lengvai kontroliuojamas, todėl produktams galima suteikti norimas fizines ir chemines savybes.

Magnio vitlokitas (Mg-WH: $Ca_{18}Mg_2(HPO_4)_2(PO_4)_{12}$) yra CP, kuriame magnio jonai iš dalies pakeičia kalcio jonus. Mg-WH gebėjimas susidaryti tirpaluose, kuriuose yra magnio, kalcio ir fosforo jonų šaltiniai, esant temperatūrai, atitinkančiai fiziologines sąlygas, rodo, kad jis gali dalyvauti įvairiuose biologiniuose ir patologiniuose procesuose. Pastarąjį dešimtmetį Mg-WH buvo minimas kaip vienas iš pagrindinių žinduolių kaulinio audinio neorganinių komponentų (kartu su jau minėtu apatito struktūros; tačiau tuo neseniai buvo suabejota). Nepaisant diskusijų šiuo klausimu, magnio jonai yra žinomi kaip labiausiai atsakingi už įvairius gyvybiškai svarbius procesus žmogaus organizme. Jie įeina į kaulinio audinio sudėtį, dalyvauja raumenų funkcijose, nervų sistemos veikloje, ir daugelyje fermentinių procesų. Nustatyta, kad magnio jonai skatina kaulų formavimąsi ir užkerta kelią osteoklastų aktyvumui. Įrodyta, kad magniu pakeisti CP padidina biokeramikos skaidumą, todėl jie labiau tinka laikinam pakeitimui arba laipsniškam pakeitimui naujai suformuotu kauliniu audiniu. Įrodyta, kad sintetinis Mg-WH, naudojamas kaip kaulų pakaitalas, skatina kaulų formavimąsi, skatina osteogeninę diferenciaciją ir stabdo osteoklastų aktyvumą fiziologinėmis sąlygomis. Nors Mg-WH dalis ir pasiskirstymas kauluose vis dar yra tyrimų ir diskusijų stadijoje, tačiau stebimas nuolatinis mokslinės bendruomenės susidomėjimas šiuo magnio turinčiu CP.

Mg-WH yra termiškai nestabilus junginys, kadangi jo struktūroje yra vandenilio fosfato (HPO_4^{2-}) grupė. Įprasti aukštatemperatūriai sintezės metodai gali sukelti šio CP skilimą; todėl jam pagaminti naudojami žematemperatūriai sintezės metodai. Mg-WH struktūros junginiai buvo susintetinti naudojant hidroterminį, nusodinimo, solvaterminį, tirpinimo-nusodinimo metodus. Buvo įrodyta, kad tirpalo pH, sintezės temperatūra, kaitinimo trukmė, sendinimo trukmė ir pradinių medžiagų lašinimas į reakcijos mišinį greitis, veikia grynos Mg-WH fazės susidarymą, o

menkiausias bet kurio iš šių parametrų pokytis, gali sukelti nepageidaujamų termodinamiškai stabilių priemaišinių CP fazių susidarymą.

Šio ***darbo tikslas*** – ištirti Mg-WH susidarymą bei fazinius virsmus naudojant brušitą (dikalcio fosfato dihidratą, $CaHPO_4 \cdot 2H_2O$, DCPD) ir gipsą (kalcio sulfato dihidratą, $CaSO_4 \cdot 2H_2O$) pradinėmis medžiagomis, taikant žematemperatūrį tirpinimo-nusodinimo sintezės metodą, bei optimizuoti sintezės sąlygas taip, kad gebėti kontroliuoti gautų miltelių cheminę sudėtį, kristališkumą ir morfologiją, siekiant panaudoti juos kaulinių audinių regeneracijoje.

Tyrimo užduotys:

• nustatyti Mg-WH fazinį grynumą, Ca/Mg molinį santykį, kristalografinius parametrus, funkcines grupes ir morfologiją esant skirtingiems Ca ir Mg moliniams santykiams pradiniame reakcijos tirpale;

• ištirti Mg-WH susidarymą vandeninėje terpėje iš gipso, kai sintezės metu magnio ir fosfato jonai yra statinėmis arba rotacinėmis sąlygomis.

Pirmoje tyrimo dalyje pagrindinis dėmesys skiriamas Mg-WH miltelių sintezei iš brušito, į reakcijos mišinį pridedant skirtingą magnio šaltinio kiekį. Buvo siekta susintetinti skirtingą Ca/Mg molinį santykį turintį Mg-WH, kuris, kaip manoma, galėtų pasižymėti skirtingomis biologinėms savybėms. Antroji tyrimo dalis skirta fazinių virsmų, sintetinant Mg-WH iš gipso statinėmis ir rotacinėmis sąlygomis, tyrimui. Pažymėtina, kad abi pasirinktos pradinės medžiagos yra netoksiškos, lengvai prieinamos, o tirpinimo-nusodinimo sintezės metodas pasižymi paprastumu, efektyvumu ir yra draugiškas aplinkai. Šis tiriamasis darbas yra svarbus siekiant ne tik padidinti supratimą apie fazinius virsmus vykstančius Mg-WH sintezės metu, bet ir turėti įrankį kuriuo galima kontroliuoti šio CP grynumą, cheminę sudėtį, kristališkumą ir mikrostruktūrą.

GINAMIEJI TEIGINIAI

1. Mg-WH cheminė sudėtis, morfologija ir dalelių dydis priklauso nuo Ca/Mg molinio santykio pradiniame reakcijos tirpale. Vienfaziai bandiniai gali būti gauti tirpinimo-nusodinimo metodu iš brušito, kai pradinis Ca/Mg santykis svyruoja nuo 4 iki 12. Didėjant Ca/Mg moliniam santykiui pradiniame reakcijos tirpale arba mažėjant magnio kiekiui WH struktūroje, gautų junginių gardelės parametrai *a* ir *c* didėja.

2. Mg-WH fazės susidarymas vykdant tirpinimo-nusodinimo sintezę iš pradinių gipso miltelių 80 °C temperatūroje statinėmis ir rotacinėmis sąlygomis vyksta dėka kelių tarpinių produktų susidarymo. Sintezė rotacinėmis sąlygomis palanki susidaryti mažesniems Mg-WH kristalams,

palyginti su bandiniu, susintetintu statinėmis sąlygomis. 24 Val. trunkančios sintezės mėginių gardelės parametrai, magnio padėties užimtumas ir gardelės tūris pakinta. Sintezės sąlygos (statinės ir rotacinės) įtakoja struktūrinius parametrams, taip pat Mg-WH bandinių kristalitų dydį ir kristališkumą.

DISERTACIJOS SANDARA

Disertacija parašyta anglų kalba, ją sudaro šios dalys: įvadas, santrumpos, literatūros apžvalga, eksperimentinė dalis, tyrimų rezultatai bei jų aptarimas, išvados, santrauka lietuvių kalba, cituojamų literatūros šaltinių sąrašas, publikacijų sąrašas, konferencijų sąrašas, padėka. Darbe pateiktos 5 lentelės ir 26 paveikslai. Bendra darbo apimtis 106 lapai. Darbe cituojami 146 mokslinės literatūros šaltiniai.

1. LITERATŪROS APŽVALGA

Literatūros apžvalgoje pirmiausia yra supažindinama su kauliniu audiniu, jo struktūra ir atsinaujinimo mechanizmu (poskyris 1.1). Sekančioje dalyje apžvelgiamos regeneracinėje medicinoje naudojamomis biomedžiagos ir aprašomos darbo tyrimo objekto Mg-WH pagrindinės savybės (poskyris 1.2.). Poskyryje 1.3 supažindinama su kalcio fosfatų sintezės būdais, plačiau aprašomas darbo metu taikytas tirpinimo-nusodinimo sintezės metodas bei apžvelgiami Mg-WH sintezės būdai.

2. EKSPERIMENTO METODIKA

Šiame skyriuje aprašyti eksperimente naudoti reagentai ir tirpalai, mėginių sintezės, mėginių apibūdinimui naudota įranga ir analizės metodika. Poskyryje 2.1 surašyti mėginių sintezei ir jų analizei naudoti reagentai, nurodant jų grynumą, koncentraciją ir gamintoją. Skyrelyje 2.2.1 aprašyta Mg-WH miltelių sintezė iš brušito, į reakcijos mišinį pridedant skirtingą magnio šaltinio kiekį. Skyrelyje 2.2.2 aprašyta Mg-WH mėginių, skirtų fazinių virsmų tyrimui, sintezės iš gipso eiga. Paskutinis 2.3 poskyris skirtas susintetintų mėginių apibūdinimui ir analizei naudotos įrangos bei matavimų sąlygų aprašymui.

3. REZULTATAI IR JŲ APTARIMAS

3.1. Mg-WH miltelių su skirtingu magnio kiekiu sintezė apibūdinimas

Tirpinimo-nusodinimo sintezės metu iš brušito ($CaHPO_4 \cdot 2H_2O$), fosforo rūgšties ($H_3PO_4(aq)$) ir skirtingo kiekio magnio acetato tetrahidrato ($Mg(CH_3COO)_2 \cdot 4H_2O$) susintetintas Mg-WH. Siekiant ištirti gautų miltelių fazinę ir cheminę sudėtį, struktūrines savybes bei morfologiją, ir įvertinti magnio jonų kiekio pradiniame reakcijos tirpale įtaką sintetinamam produktui, jie tirti skirtingais analizės metodais,.

1a paveiksle pavaizduoti susintetintų Mg-WH miltelių XRD, pradiniame reakcijos mišinyje esant skirtingam Ca/Mg santykiui. Mg-WH kristalizuojasi sudarydamas romboedrinę kristalinę gardelę, o difrakcijos smailės priskirtinos R3c (# 161) erdvinei grupei (ICDD #00-070-2064). Nepaisant skirtingo Ca/P santykio pradiniame reakcijos mišinyje, visuose gautų mėginių XRD matyti WH kristalinei struktūrai būdingos smailės. Mėginių, kurių Ca/Mg santykis kito nuo 4 iki 12, difraktogramose nepastebėta jokių priemaišinių antrinių CP fazių. Papildomos mažo intensyvumo smailės ties $2\theta \approx 31{,}73°$ ir $2\theta \approx 32{,}20°$, priklausančios CDHA (ICDD #00-046-0905), matomos tik Ca/Mg = 15 mėginio difraktogramoje. Svarbu pažymėti, kad padidinus magnio jonų koncentraciją pradiniame reakcijos mišinyje, tai yra sumažinus Ca/Mg santykį, analizuotų bandinių difrakcijos smailės pasislenka didesnių difrakcijos kampų link, o tai, galimai, atsitinka dėl Mg-WH kristalinės gardelės sumažėjimo. 1 paveikslo b dalyje pavaizuota pagrindinė (0 2 10) difrakcijos smailė, esanti ties $2\theta \approx 31°$. Smailės padėtis slenkasi į mažesnių 2θ kampų pusę pradiniame reakcijos mišinyje didinant Ca/Mg santykį. Tai vyksta dėl Mg-WH kristalinės gardelės sumažėjimo, kurį galima paaiškinti tuo, kad šešiakoordinuoto Ca^{2+} jono spindulys yra 1,00 Å, o šešiakoordinuoto Mg^{2+} joninis spindulys yra tik 0,72 Å.

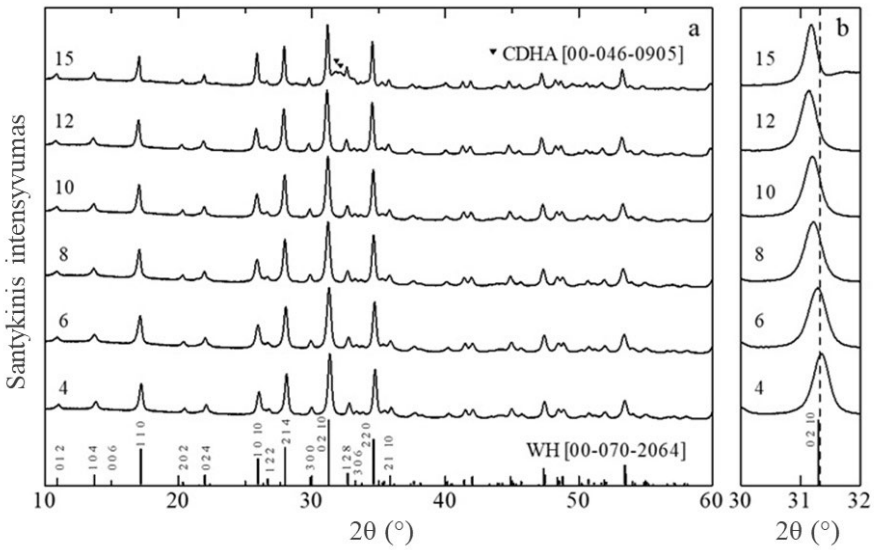

1 pav. a) Susintetintų Ca/Mg = 4, 6, 8, 10, 12 ir 15 mėginių XRD; b) pavaizduota išdidinta (0 2 10) difrakcijos smailės sritis.

Siekiant nustatyti struktūrinius junginių parametrus, atliktas vienfazių Mg-WH bandinių (Ca/Mg = 4, 6, 8, 10 ir 12) XRD duomenų Rietveldo patikslinimas *FullProf* programa. Tikslinimo metu Mg-WH struktūrai būdingos difrakcijos smailės priskirtos R3c (#161) erdvinei grupei. 2a ir 2b paveiksluose pavaizduoti vienfazių bandinių gardelės parametrai, keičiantis Ca ir Mg moliniam santykiui pradiniame reakcijos tirpale, ir keičiantis magnio moliniam kiekiui procentais (Mg/(Mg + Ca)), apskaičiuotam pagal tikslinimo metu nustatytą Ca^{2+} ir Mg^{2+} kristalografinių padėčių užimtumą. Akivaizdu, kad didėjant magnio koncentracijai pradiniame sintezės mišinyje, *a* ir *c* gardelės parametrai mažėjo, nes didėjo magnio kiekis WH struktūroje (žiūrėti 1 lentelę).

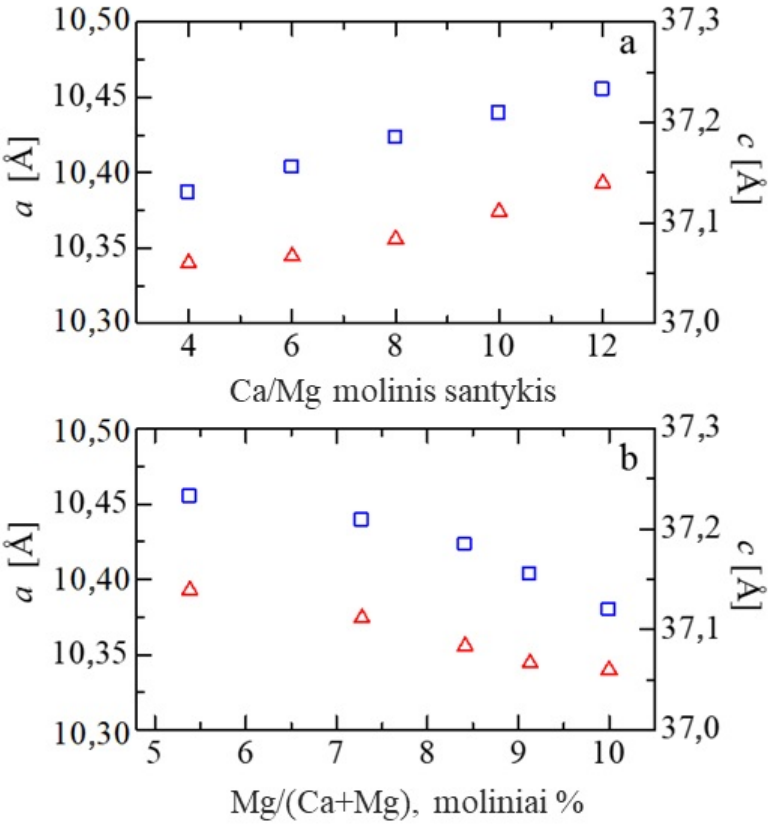

2 pav. A dalyje *a* (raudoni trikampiai) ir *c* (mėlyni kvadratai) gardelės parametrų, priklausomybė nuo Ca ir Mg molinio santykio pradiniame reakcijos tirpale. B dalyje *a* (raudoni trikampiai) ir *c* (mėlyni kvadratai) gardelės parametrų priklausomybė nuo apskaičiuotų Mg/(Mg + Ca) santykių, moliniais procentais.

Lentelė 1. Struktūros patikslinimo rezultatai, Ca/Mg = 12, 10, 8, 6 ir 4 mėginių.

Pradinis Ca/Mg molinis santykis	**Nustatytas Ca/Mg molinis santykis**	**Nustatytas Mg/(Ca+Mg), moliniais procentais**	***a*, Å**	***c*, Å**
4	9,00(0)	9,99(9)	10,3401(1)	37,1301(1)
6	9,95(5)	9,12(9)	10,3445(8)	37,1554(3)
8	10,8(8)	8,41(6)	10,3558(6)	37,1847(1)
10	12,7(4)	7,27(9)	10,3743(2)	37,2090(4)
12	17,5(7)	5,38(4)	10,3930(8)	37,2326(7)

Ca/Mg santykis susintetintoje WH struktūroje sumažėjo nuo 17,6 (Ca/Mg = 12 bandinys) iki 9,0 (Ca/Mg = 4), o tuo pat metu tų pačių bandinių magnio molinė procentinė dalis padidėjo nuo 5,3 (Ca/Mg = 12) iki 10 (Ca/Mg = 4). Gauti rezultatai rodo, kad pradiniame reakcijos mišinyje buvęs magnis nevisiškai įsiterpė į sintetinamo junginio struktūrą.

Susintetintų mėginių kristalitų dydžiai apskaičiuoti pagal pagrindinės (0 2 10) difrakcinės smailės išplatėjimą ir Šererio formulę. Apskaičiuota, kad mėginių kristalitų dydžiai svyravo nuo 29 nm (Ca/Mg = 15 mėginyje) iki 25 nm (Ca/Mg = 4 mėginyje).

2 lentelėje pateiktas iš ICP-OES cheminės analizės rezultatų apskaičiuotas Ca/Mg molinis santykis ir magnio molinė procentinė dalis susintetintuose WH milteliuose. Nustatyta, Ca/Mg santykis susintetintoje WH struktūroje sumažėjo nuo 10,4 (Ca/Mg = 12 bandinys) iki 5,33 (Ca/Mg = 4), o Mg^{2+} jonų kiekis susintetintuose mėginiuose padidėjo nuo 8,74 (Ca/Mg = 12 bandinys) iki 15,8 (Ca/Mg = 4 bandinys) molinių procentų, nepaisant to, kad XRD duomenys rodė, kad susintetinti bandiniai yra vienfaziai. Kadangi nustatyta, kad sintezės metu ne visas magnis įsiterpia į sintetinamos medžiagos gardelę, galime daryti prielaidą, kad mėginiuose gali būti tam tikra antrinė magnio turinti CP fazė, kuri tikėtina yra amorfinė arba jos kiekis yra nereikšmingas, mažesnis už XRD aptikimo ribą.

Lentelė 2. Ca/Mg = 4, 6, 8, 10 ir 12 mėginių ICP-OES analizės rezultatai.

Pradinis Ca/Mg molinis santykis	Nustatytas Ca/Mg molinis santykis	Nustatytas Mg/(Ca+Mg), moliniais %
4	5,33	15,8
6	6,06	14,2
8	6,53	13,3
10	7,82	11,3
12	10,4	8,74

Susintetinti mėginiai ištirti FT-IR spektroskopijos metodu, o rezultatai pateikti 3 pav. Plati absorbcijos juosta 1200 – 800 cm^{-1} srityje sudaryta iš kelių persidengiančių smailių. Siekiant nustatyti tikslias smailių padėtis, FT-IR spektrai išskaidyti į atskiras smailes, naudojant Gauso matematinę funkciją (4 pav.). Spektrai $\nu_{3,1}$ PO_4^{3-} srityje nesiskiria tarp visų išmatuotų mėginių: stebimos absorbcijos smailės ties 1135 cm^{-1}, 1097 cm^{-1}, 1066 cm^{-1}, 1011 cm^{-1}, 987 cm^{-1} ir 960 cm^{-1} puikiai atitinka užfiksuotas Jang *et al*. 930 – 800 Cm^{-1} sritis buvo išskirta į tris dedamąsias (913 cm^{-1}, 884 cm^{-1} ir 860 cm^{-1}), Ca/Mg = 10, 12, 15 mėginių atveju, ir du komponentus (919 cm^{-1} ir 891 cm^{-1}), Ca/Mg

= 4, 6, 8 mėginių atveju. Minėti virpesiai priskirti vandenilio fosfato grupės P–O–H ryšio virpesiams. Absorbcijos smailė ties 919 cm^{-1} yra priskirtina P–O–H ryšio, esančiam Mg-WH struktūroje, tempimo modai. Įdomu pastebėti, kad Ca/Mg = 15 mėginio atveju ši juosta pasislenka į žemesnes bangas, tai yra į 913 cm^{-1}. Taip galimai atsitinka dėl CDHA fazės, prieš tai aptiktos atliekant Ca/Mg = 15 mėginio XRD analizę, mėginyje įtakos. Absorbcijos juosta užfiksuota ties 860 cm^{-1} kartu su papildoma komponente ties 1175 cm^{-1} irgi priskirtinos CDHA fazei. Smailės užfiksuotos ties 884 cm^{-1} (Ca/Mg = 10, 12, 15 mėginiuose) ir 891 cm^{-1} (Ca/Mg = 4, 6, 8 mėginiuose) sukėlė prielaidą, kad mėginiuose gali būti karbonatinio hidroksiapatito (CO_3-Ap), tačiau tuo atveju būtų stebimos virpesių juostos 1400 – 1550 cm^{-1} intervale. Verta paminėti, kad juostos (884 cm^{-1} ir 891 cm^{-1}) gali būti susijusios su monetito ($CaHPO_4$) faze, nors XRD nebuvo matyti šios fazės atspindžių. Absorbcijos esant 640 – 500 cm^{-1} ir 430 cm^{-1} atitinka fosfatų $\nu_4(PO_4^{3-})$ ir $\nu_2(PO_4^{3-})$ lenkimo modas.

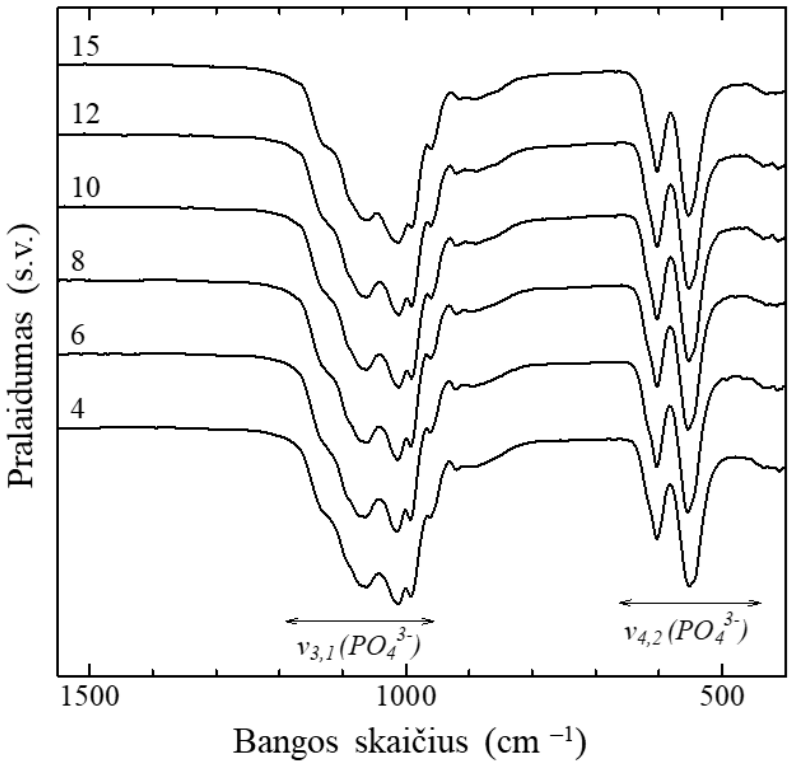

3 pav. Susintetintų mėginių Ca/Mg = 4 – 15 FT-IR spektrai.

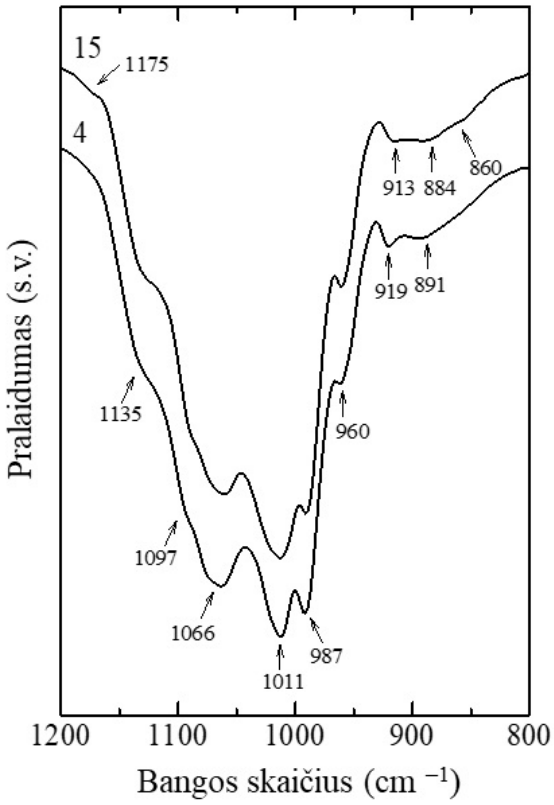

4 pav. Ca/Mg = 4 ir Ca/Mg = 15 mėginių FT-IR spektrai.

Susintetintų Mg-WH mėginių, turinčių skirtingą Ca ir Mg molinį santykį, SEM nuotraukos pateiktos 5 paveiksle. Kaip ir buvo tikėtasi, susintetintų produktų paviršiaus morfologija priklauso nuo magnio kiekio susintetinamame Mg-WH. Nuotraukose matyti, kad susidaro romboedrinių, heksagoninių ir sferinių nanodalelių, kurių dydis svyruoja nuo ~10 iki – 100 nm. Ca/Mg = 15 mėginio paviršiuje yra lazdelių formos dalelių, priskirtinų CDHA fazei (5a ir 5e pav.). Ca/Mg = 12 bandinys (5b ir 5f pav.) sudarytas iš ~150 nm dydžio monodispersinių romboedrinių WH dalelių. Mišrios sferinės-romboedrinės dalelės (mažesnės nei 20 nm) susidarė Ca/Mg = 4 bandinyje (5d ir 5h pav.). Iš SEM nuotraukų matyti, kad didėjantis Mg kiekis WH struktūroje, sukelia susidarančio produkto dalelių dydžio mažėjimą ir aglomeraciją. Atrodytų, kad šie rezultatai prieštarauja XRD metodu gautiems rezultatams, tačiau labai gerai žinoma, kad XRD rezultatai leidžia apskaičiuoti kristalitų dydį, o SEM – dalelių (kristalitų aglomeratų) dydį, todėl šių dydžių palyginimas ne visada galimas.

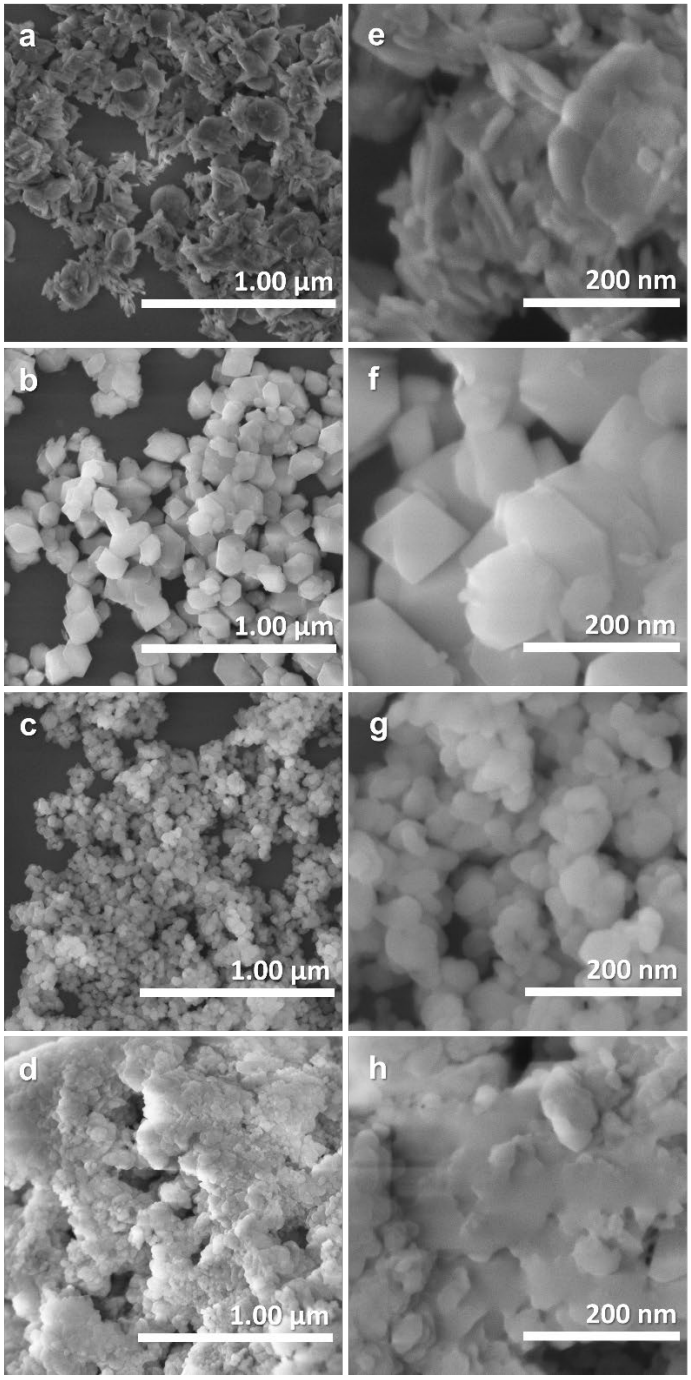

5 pav. Miltelių, susintetitų esant skirtingam Ca/Mg moliniam santykiui pradiniame reakcijos tirpale, SEM vaizdai: (a), (e) Ca/Mg = 15; (b), (f) Ca/Mg = 12; (c), (g) Ca/Mg = 8; and (d), (h) Ca/Mg = 4.

Tikslesnis atrinktų mėginių (Ca/Mg = 15, Ca/Mg = 12; Ca/Mg = 8 ir Ca/Mg = 4) dalelių dydis bei forma buvo nustatyti naudojant TEM, o gauti vaizdai pateikti 6 paveiksle. Iš nuotraukos pateiktos 6a paveiksle matyti, kad Ca/Mg = 15 mėginys yra sudarytas iš dviejų fazių, ką jau anksčiau patvirtino XRD, FTIR ir SEM. Heksagoninio WH dalelių dydis svyravo nuo ~30 iki 230 nm intervale (vidutinis dydis yra ~120 nm), o lazdelių pavidalo CDHA dalelės ~45 nm. Heksagoninės ir romboedrinės formos dalelės, kurių dydis yra maždaug 110 nm (atskirų dalelių dydis svyravo ~22 – 230 nm intervale), susidarė Ca/Mg = 12 mėginyje (6b pav.). Kaip ir tikėtasi, WH struktūros susintetintų produktų dalelių forma ir dydis priklauso nuo magnio kiekio susintetintame WH. Toliau didėjant magnio kiekiui WH struktūroje gautos mažesnio dydžio netaisyklingos, neapibrėžtos formos dalelės tapo mažesnės (žr. 6c ir 6d pav. atitinkamai Ca/Mg = 8, Ca/Mg = 4 mėginiams). Ca/Mg = 8 mėginio (6c pav.) TEM nuotrauka atskleidžia, kad susidarė ~40 nm dydžio dalelės (atskirų dalelių dydis svyruoja nuo ~10 iki 70 nm), o Ca/Mg = 4 mėginio (6d pav.) mėginį sudarė ~30 nm dydžio dalelės (atskirų dalelių dydis svyravo nuo ~15 iki 60 nm).

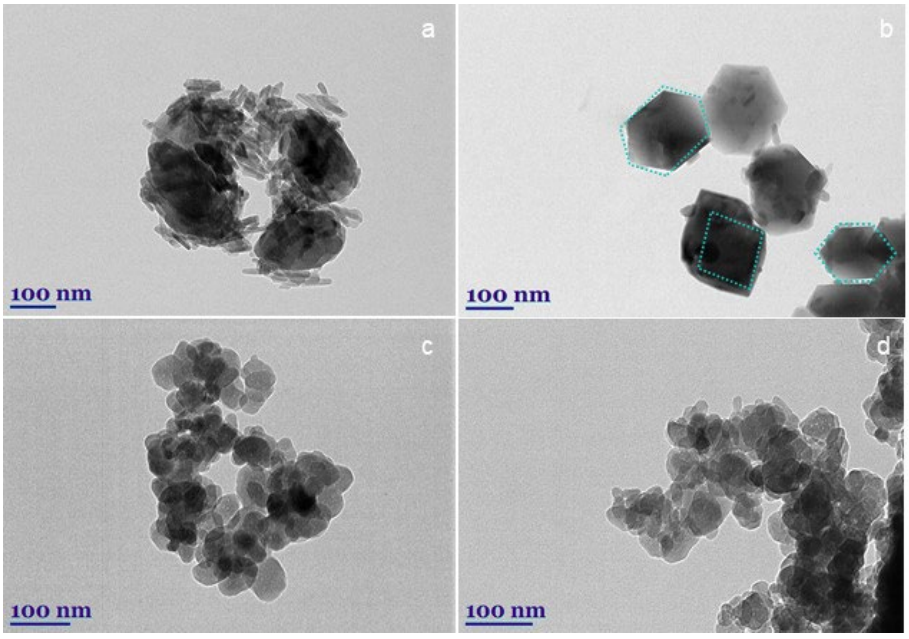

6 pav. Susintetintų miltelių, paruoštų pradiniame reakcijos tirpale esant skirtingam Ca/Mg moliniam santykiui, TEM nuotraukos: (a) Ca/Mg = 15; (b) Ca/Mg = 12; (c) Ca/Mg = 8; and (d) Ca/Mg = 4.

3.2. Faziniai virsmai sintetinant Mg-WH iš gipso statinėmis ir rotacinėmis sąlygomis

Tirpinimo-nusodinimo sintezės metu iš gipso ($CaSO_4 \cdot 2H_2O$), magnio acetato tetrahidrato ($Mg(CH_3COO)_2 \cdot 4H_2O$) ir natrio divandenilio fosfato (NaH_2PO_4) ir dinatrio vandenilio fosfato (Na_2HPO_4) buvo susintetintas Mg-WH. Sintezė buvo vykdoma skirtingą laiko tarpą statinėmis ir rotacinėmis sąlygomis, siekiant nustatyti fazinius virsmus susidarant Mg-WH fazei. Mg-WH fazės formavimasis buvo stebimas lyginant produktų, sintetintų 4 val., 6 val., 12 val. ir 24 val. esant 80 °C temperatūrai, difraktogramas (7 pav. pavaizduoti XRD gauti tiriant bandinius, kurių sintezė buvo vykdoma statinėmis sąlygomis, o XRD 8 pav. gauti tiriant bandinius, kurių sintezė buvo vykdoma rotacinėms sąlygomis).

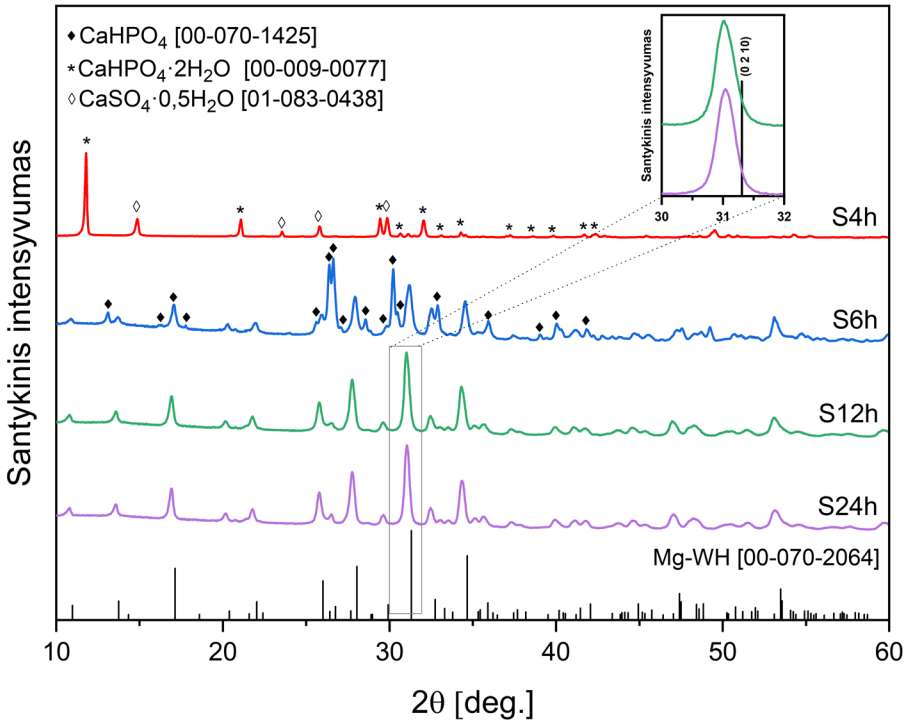

7 pav. Bandinių, susintetintų statinėmis sąlygomis, XRD. Intarpe išdidinta S12h ir S24h bandinių (0 2 10) difrakcijos smailės sritis.

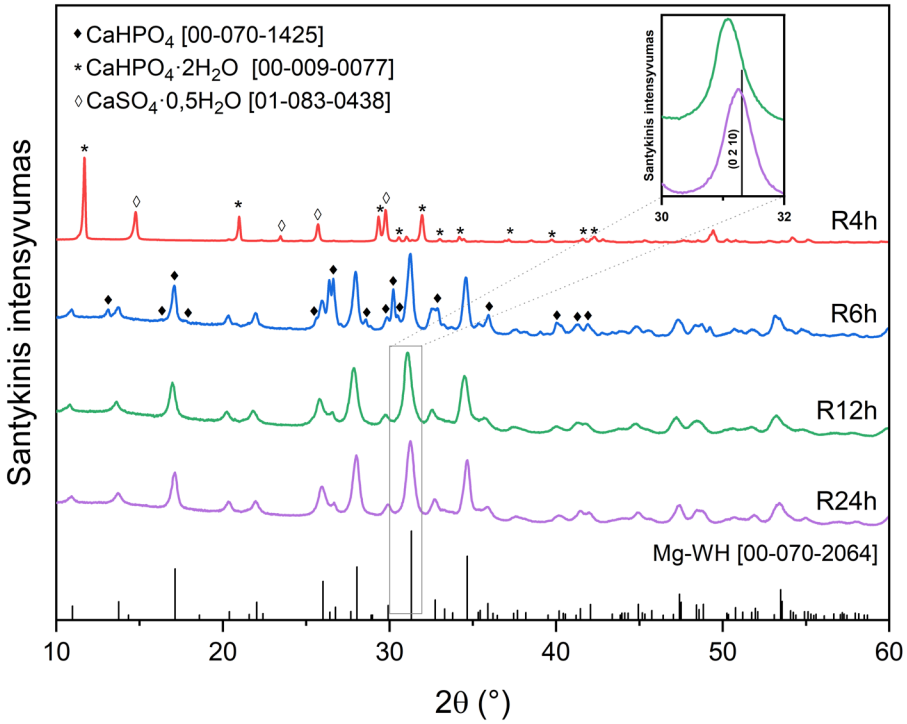

8 pav. Bandinių, susintetintų statinėmis sąlygomis, XRD. Intarpe išdidinta S12h ir S24h bandinių (0 2 10) difrakcijos smailės sritis.

Po 4 val. sintezės nepriklausomai nuo sąlygų (statinių ar rotacinių), susintetintų mėginių difraktogramos atitiko kalcio sulfato hemihidrato ($CaSO_4 \cdot 0{,}5H_2O$, CSH; ICDD #01-083-0438) ir DCPD (ICDD #00-009-0077) mišinį. CSH susidarymas vyksta dėl dalinės gipso dehidratacijos, o ne dėl jo tirpimo. Gipsas, net ir aukštoje temperatūroje, yra mažiau tirpus nei CSH (viena iš pagrindinių tirpinimo-nusodinimo sintezės sąlygų yra ta, kad pirmtako tirpumas turėtų būti didesnis nei nusėdančio produkto tirpumas). Tuo tarpu DCPD susidarymas vyksta dėka CSH tirpimo (tuo metu į reakcijos tirpalą tiekiami Ca^{2+} jonai) ir reakcijos tirpale jau esančių vandenilio fosfato jonų reakcijos su susidarančiais Ca^{2+} jonais. DCPD esant apytiksliai neutraliam pH yra metastabili fazė, naudojama pirmtaku kitiems CP medžiagoms sintetinti. Pagal Ostvaldo stadijų taisyklę pradžioje nusėda mažiausiai termodinamiškai stabili fazė, kuri vėliau transformuojasi į stabilesnę. Vadinasi, vandeninėje terpėje DCPD gali virsti stabilesniu CP, pav., kalcio hidroksiapatitu (HAp, $Ca_{10}(PO_4)_6(OH)_2$), oktakalcio fosfatu ($Ca_8H_2(PO_4)_6 \cdot 5H_2O$) arba jų mišiniu, todėl reakcijos sistema turi būti papildomai stabilizuota, siekiant išvengti nepageidaujamų antrinių fazių

susidarymo. Reikia pabrėžti, kad magnio jonų buvimas reakcijos tirpale neleidžia DCPD virsti šiais termodinamiškai stabiliais CP net esant padidinto pH sąlygomis.

Reakcijai vykstant toliau, antras reikšmingas produkto sudėties pokytis pastebėtas po 6 val. esant tiek statinėms, tiek rotacinėms sintezės sąlygoms. Gautame mėginyje aptiktos difrakcijos smailės, atitinkančios bevandenį kalcio vandenilio fosfatą (DCPA, $CaHPO_4$; ICDD #00-070-1425) ir Mg-WH fazę (ICDD #00-070-2064). Manoma, kad tirpesnis DCPD virto mažiau tirpiu DCPA, kuris virto Mg-WH. Tikėtina, kad 6 val. sintetintame mėginyje susidarius DCPA fazei, sumažėjo reakcijos tirpalo pH ($Ca^{2+}(aq) + H_2PO_4^-(aq) \rightarrow CaHPO_4(k) + H^+(aq)$) ir jis tapo tinkamas Mg-WH fazei nusodinti, nes gerai žinoma, kad Mg-WH fazė nusėda esant magnio jonų pertekliui tirpale ir silpnai rūgštiniam pH. Nustatyta, kad S6h mėginį sudarė 60 masės % DCPA bei 40 masės % Mg-WH, tuo tarpu, R6h mėginį nors kokybiškai sudarė tos pačios sudedamosios dalys, tačiau Mg-WH fazė buvo pagrindinė – 55 % masės, DCPA komponentas sudarė 45 masės %. Taigi, sukimasis kartu su reakcijos suspensijos maišymu (rotacinės sąlygos) galimai padidino pradinių ir tarpinių produktų tirpumą, darė įtaką gautų medžiagų dalelių dydžiui, galimai susidarant greičiau reaguojantiems tarpiniams produktams, kas lėmė skirtingą Mg-WH fazės susidarymo greitį.

Galiausiai, kai reakcijos laikas buvo pratęstas iki 12 val., DCPA fazė abiejuose tirtuose bandiniuose (S12h ir R12h) išnyko. Mg-WH kristalizuojasi sudarydamas romboedrinę kristalinę gardelę, kurios parametrai $a = b =$ 10,350(5) Å, c = 37,085(12) Å ir $\alpha = \beta = 90°$, $\gamma = 120°$ (R3c (# 161) erdvinė grupė). Visos XRD tyrimo metu užfiksuotos difrakcijos smailės sutapo su Mg-WH (ICDD #00-070-2064) fazei būdingais atspindžiais. Taigi, taikant aprašytą sintezės būdą, buvo gauti vienfaziai Mg-WH struktūros S12h ir R12h bandiniai. Reikėtų pažymėti, kad atidžiai sulyginus mėginių XRD ir standartą pastebėta, kad S12h ir R12h bandinių ir standarto 2θ smailių padėtys nevisiškai sutampa. Susintetintų S12h ir R12h bandinių XRD smailės pasislinkusios mažesnių 2θ kampų link (išdidinti XRD vaizdai su atspindžiu nuo pagrindinės (0 2 10) plokštumos parodyti 7 ir 8 paveikslų intarpuose). S12h mėginyje minėtas atspindys užfiksuotas ties $2\theta = 31{,}01°$, R12h mėginyje ties $2\theta = 31{,}07°$, o intensyviausia etalono smailė ties $2\theta = 31{,}31°$. Difrakcijos smailės poslinkis mažesnių 2θ kampų link reiškia, kad susintetintų mėginių tarpplokštuminis atstumas skiriasi nuo standarto, o tai rodo, kad S12h ir R12h mėginių katijoninių padėčių užimtumas kristalinėje gardelėje gali būti skirtingas nei standarto.

Siekdami išsiaiškinti, kokią įtaką produkto sendinimas turi Mg-WH fazės grynumui, morfologijai ir struktūriniams parametrams, sintezės laikas pratęstas dar 12 val. Gautuose 24 val. trukmės bandinių (S24h ir R24h) difraktogramose nebuvo jokių pašalinių smailų, tik priskirtinos Mg-WH fazei. Pastebėtina, kad pagrindinė (0 2 10) smailė S24h mėginyje užfiksuota ties 2θ = 31,04°, R24h mėginyje – ties 2θ = 31,26°.

Žinoma, kad Mg-WH struktūros CP gali būti gauti šiek tiek skirtingo Ca ir Mg santykio nei aprašo jo cheminė formulė ($Ca_{18}Mg_2(HPO_4)_2(PO_4)_{12}$). Darbe parodyta, kad susintetintų Mg-WH bandinių *a* ir *c* gardelės parametrai didėja didėjant Ca ir Mg moliniam santykiui pradiniame reakcijos tirpale (mažėjant magnio kiekiui WH struktūroje). Tai buvo paaiškinta Mg^{2+} jono, kurio spindulys lygus 0,72 Å, pakeitimu didesnio joninio spindulio Ca^{2+} (1,00 Å) jonu, kuris lėmė gardelės parametrų padidėjimą. Siekiant patvirtinti susintetintų S12h, R12h, S24h ir R24h mėginių grynumą ir įvertinti jų struktūrinius parametrus, atliktas Rietveldo struktūros patikslinimas naudojant *FullProf* programą (9 pav. pateikta S12h mėginio patikslinta XRD). Apskaičiuoti S12h, R12h, S24h ir R24h mėginių struktūriniai duomenys apibendrinti 3 lentelėje.

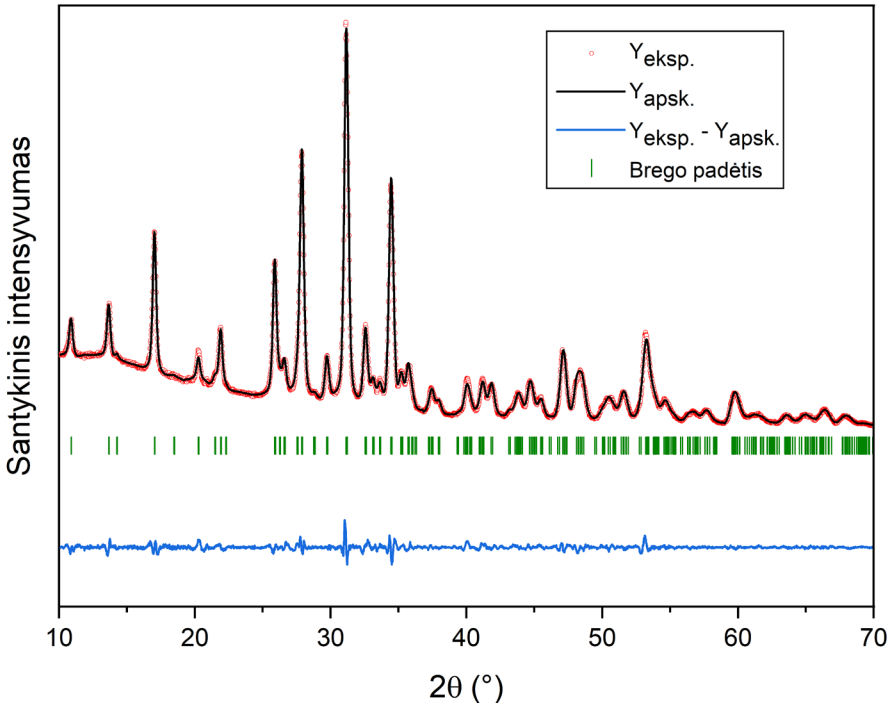

9 pav. Rietveldo metodu patikslinta S12h mėginio XRD.

Lentelė 3. S12h, S24h, R12h ir R24h bandinių struktūriniai duomenys.

Sample	S12h	S24h	R12h	R24h
***a*, Å**	10,406(7)	10,397(2)	10,352(6)	10,351(9)
***c*, Å**	37,216(9)	37,178(8)	37,170(7)	37,151(2)
Cell volume, Å^3	3490,5(6)	3480,5(9)	3450,1(1)	3447,7(9)
Occ (Ca)	0,167(3)	0,138(4)	0,037(7)	0,021(4)
Occ (Mg)	0,166(3)	0,195(4)	0,295(7)	0,312(4)
R_p	2,61	2,38	2,05	2,45
R_{wp}	3,42	3,16	2,64	3,20
χ^2	2,84	2,40	1,71	2,54
Kristalitų dydis, nm	30	30	16	22
Klistališkumas (amorfiškumas), %	61 (39)	67 (33)	54 (46)	58 (42)

3 lentelėje pateikti skaičiavimų rezultatai rodo, kad kristalinės gardelės parametrai, magnio padėties užimtumas ir gardelės tūris pakito labai nežymiai, prailginus sintezės laiką iki 24 val. Svarbu pažymėti, kad šie parametrai gerokai skiriasi, kai lyginami bandiniai, susintetinti skirtingomis sąlygomis. Pažymėtina, kad esant maišymui (rotacinės sąlygos), buvo gauti daugiau magnio WH struktūroje turintys mėginiai. Kaip matyti iš 3 lentelėje pateiktų rezultatų, statinėmis sąlygomis (sintezė vykstanti be maišymo) susintetinti mėginiai sudaryti iš didesnių kristalitų bei pasižymi didesniu kristališkumu, nepaisant to, kad Mg-WH susidarymo greitis statinėmis sąlygomis buvo mažesnis. Rotacinėmis sąlygomis Mg-WH kristalizacijos centrų susidarymas vyko sparčiau nei statinėse sąlygose, todėl R12h ir R24h susidariusios medžiagos sudarytos iš mažesnių kristalitų. Pažymėtina, kad mėginio kristališkumas gali būti kontroliuojamas parenkant sintezės sąlygas.

Funkcinėms grupėms susintetintuose mėginiuose nustatyti, buvo naudojama FT-IR spektroskopija. FT-IR spektrai rodo, kad mėginiuose S4h ir R4h yra sulfato (SO_4^{2-}), fosfato (PO_4^{3-}) ir vandenilio fosfato (HPO_4^{2-}) jonų (žr. 10 pav. mėginiams, gautiems statinėmis sąlygomis, ir 11 pav. mėginiams, gautiems rotacinėmis sąlygomis). Juostos, esančios maždaug ties 1150 – 1090 cm^{-1}, priklauso SO_4^{2-} ir PO_4^{3-} grupių, esančių CSH ir DCPD fazių kristalinėje struktūroje, ν_3 modoms. Smailės, esančios ties 1006 cm^{-1} ir 985 cm^{-1}, atitinka minėtų grupių S-O ir P-O ν_1 modas. Tuo tarpu smailės, kurių centrai yra ties 872 cm^{-1} ir 789 cm^{-1}, gali būti priskirtos atitinkamai HPO_4^{2-} grupei, esančiai DCPD struktūroje. Juostos 660 – 595 cm^{-1} ir 463 cm^{-1} gerai atitinka sulfato jone esančio S–O ryšio ν_4 ir ν_2 modas, o 574 cm^{-1} petys ir 522 cm^{-1} juosta

siejami su DCPD struktūroje esančios HPO_4^{2-} grupės O–P–O(H) ryšio lenkimo modomis.

Mėginių sintetintų 6 val. FT-IR spektruose, nepriklausomai nuo sintezės sąlygų, yra tik PO_4^{3-} ir HPO_4^{2-} grupėms būdingos absorbcijos juostos. Gautuose mėginiuose nebėra jokių sulfato grupės požymių. Iš spektrų matyti, kad dėl ilgesnio sintezės laiko pasikeitė gautų bandinių fazinė sudėtis Smailės ties 1130 cm^{-1}, 1068 cm^{-1}, 1015 cm^{-1} ir petys ties 1010 cm^{-1} priskiriami ν_3, o juosta ties 954 cm^{-1} atitinka PO_4^{3-} grupės, esančios DCPA ir Mg-WH kristalinėse struktūrose, ν_1 virpesius. Juosta ties 1190 cm^{-1} gali būti susijusi su P–O–(H) ryšio, esančios Mg-WH struktūroje, lenkimo moda. Įdomu pastebėti, kad S6h mėginio FT-IR spektre yra gana plati juosta su dviem maksimumais ties 887 cm^{-1} ir 866 cm^{-1}, priskiriama HPO_4^{2-} grupės P-O(H) ryšio tempimo virpesiams. Taip yra todėl, kad dvifaziame bandinyje yra dvi skirtingos kristalografinės vandenilio fosfato jonų aplinkos (S6h bandinį sudarė 60 % masės DCPA ir 40 % masės Mg-WH fazės, o R6h bandinį – 45 % masės DCPA ir 55 % masės Mg-WH komponentas). Absorbcijos ties 602 cm^{-1}, 550 cm^{-1} ir 465 cm^{-1} atitinka ν_4 (P–O) ir ν_2 (O–P–O) ryšių, esančių PO_4^{3-} ir HPO_4^{2-} grupėse, modas.

Vienfazio Mg-WH susidarymą 12 val. ir 24 val. sintetintuose mėginiuose patvirtina ir FT-IR spektrai, rodantys, kad mėginiuose yra tik PO_4^{3-} ir HPO_4^{2-} grupėms būdingi virpesiai. Petys ties 1190 cm^{-1} susijęs su P–O–H ryšio, esančio Mg-WH struktūroje, absorbcija. Smailės ties 1130 cm^{-1}, 1068 cm^{-1}, 1015 cm^{-1}, 1010 cm^{-1} (petys) ir 954 cm^{-1} atsiranda dėl P–O ryšio ν_3 ir ν_1 virpesių. Juostų ties 604 cm^{-1}, 550 cm^{-1} ir 465 cm^{-1} buvimą lemia P-O ryšio lenkiamieji ν_4 ir ν_2 virpesiai PO_4^{3-} ir HPO_4^{2-} grupėse. Plati juosta, kurios centras yra ties 868 cm^{-1}, yra P–O–H ryšio, esančio Mg-WH kristalinėje struktūroje, absorbcija. Pastebėtina, kad mėginių R12h ir R24h, gautų rotacinėmis sąlygomis FT-IR spektrų smailės ir juostos yra labiau suapvalintos nei gautų statinėmis sąlygomis, kas susiję su jų mažesniu kristališkumu palyginti su S12h ir S24h.

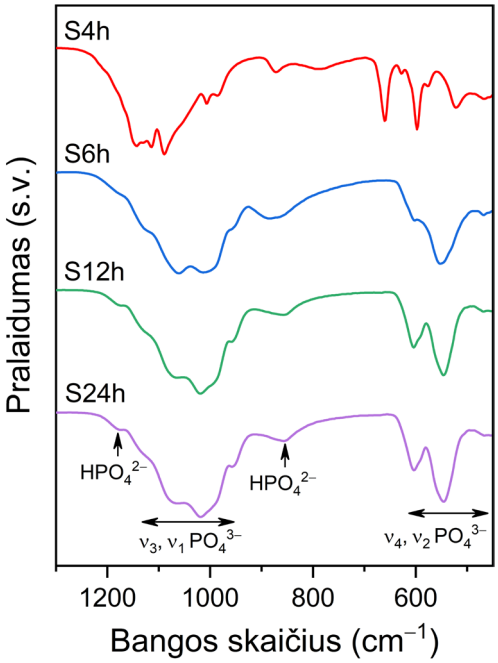

10 pav. S4h – S24h mėginių FT-IR spektrai.

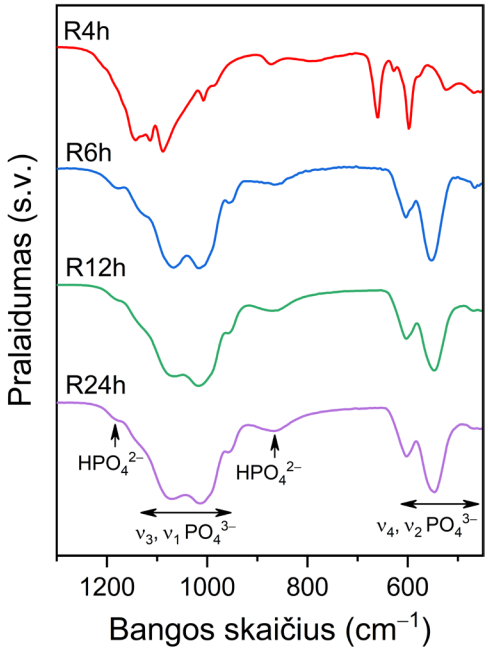

11 pav. R4h – R24h mėginių FT-IR spektrai.

S4h – S24h ir R4h – R24h mėginių, gautų sintetinant Mg-WH nanomiltelius žemoje temperatūroje skirtingomis sąlygomis, SEM nuotraukos pateiktos 12 pav.

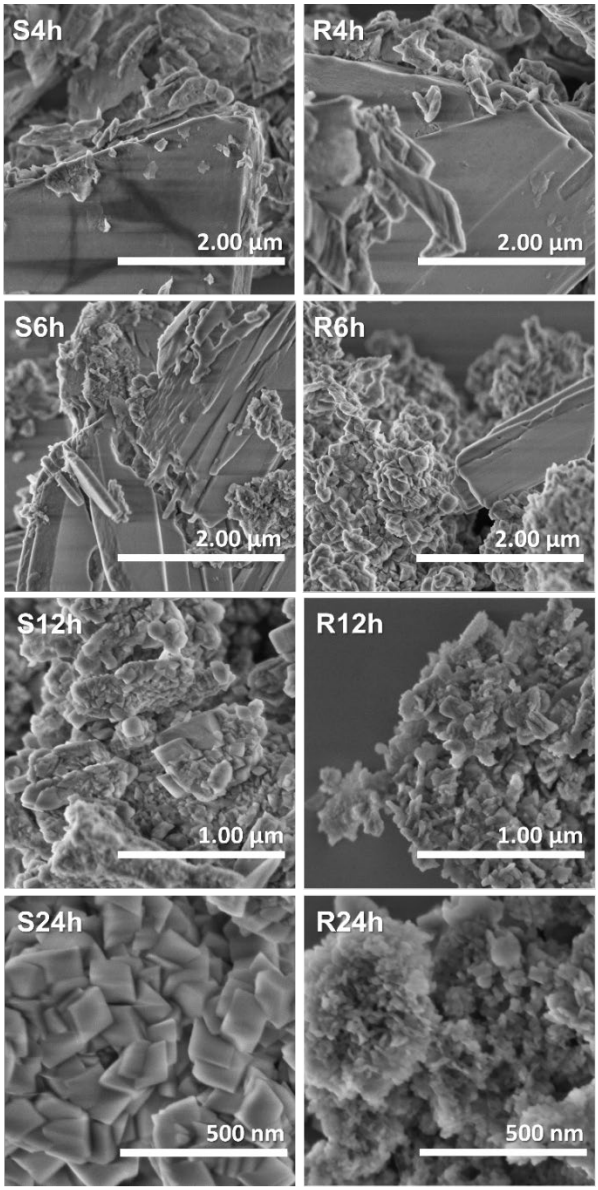

12 pav. S4h – S24h ir R4h – R24h pavyzdžių SEM nuotraukos.

Akivaizdu, kad gautų mėginių mikrostruktūra priklauso nuo jų fazinės sudėties, pasirinktų sintezės sąlygų ir reakcijos laiko. S4h, S6h, R4h ir R6h

mėginių SEM nuotraukose matyti dviejų skirtingų tipų dalelių, kas atitinka dvi skirtingas kristalines fazes identifikuotas XRD tyrimo metu. S4h mėginyje matomi plokšti, lygaus paviršiaus DCPD kristalai, kurių dydis svyruoja maždaug nuo 2 iki 3 µm. Šiuos plokščius kristalus dengia mažesnio dydžio šiurkštaus paviršiaus CSH dalelės. S6h mėginyje kartu su plokščiais DCPA kristalais matomi nedideli Mg-WH kristalitų aglomeratai. Prailginus sintezės laiką iki 12 valandų, S12h mėginio morfologinės savybės gerokai pasikeitė. Mėginį sudarė tik romboedriniai 25 iki 350 nm dydžio Mg-WH kristalai. S24h mėginio morfologija iš esmės nesikeitė, tačiau 30 iki 350 nm dydžio aglomeruotų kristalų paviršius tapo lygesnis. Morfologinius Mg-WH pokyčius galima paaiškinti pailgėjusiu sintezės laiku, kuris turėjo įtakos atomų išsidėstymo gardelėje ir galimam antrinių fazių pašalinimui. Vykdant Mg-WH nanomiltelių sintezę rotacinėmis sąlygomis, pradiniame sintezės etape (mėginys R4h) taip pat susidarė lygaus paviršiaus plokštieji daugiau už 3 µm dydžio DCPD kristalai bei nelygaus paviršiaus CSH kristaliniai dariniai. R6h mėginyje be plokščiųjų DCPA kristalų susidarė smulkūs 15 − 75 nm Mg-WH aglomeratai. Toliau ilgėjant sintezės laikui, Mg-WH kristalų morfologija ir jų agregacija išliko, tačiau šiek tiek padidėjo atskirų kristalinių darinių dydis. Apibendrinant galima teigti, kad gauti SEM rezultatai atitinka XRD analizės ir FT-IR spektroskopijos rezultatus.

Atsižvelgiant į rezultatus, siūloma Mg-WH susidarymo schema taikant tirpinimo-nusodinimo metodą statinėmis ir rotacinėmis sąlygomis pavaizduota 14 paveiksle. Mg-WH susidarymas rotacinėmis sąlygomis vyksta greičiau nei statinėmis sąlygomis. Be to, sintezės trukmė neturi didelės įtakos susintetinto Mg-WH kristalitų dydžiui statinėmis sąlygomis, bet turi rotacinėmis sąlygomis. Didėjant sintezės trukmei nuo 12 val. iki 24 val., kai sintezė vykdoma rotacinėmis sąlygomis, didėja Mg-WH kristalitų, ir jų aglomeratų dydis.

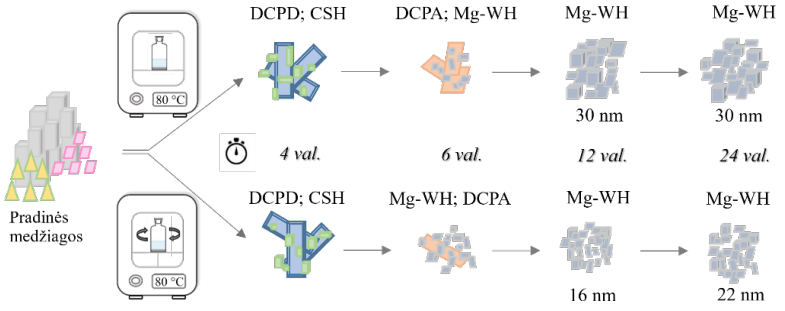

13 pav. Mg-WH susidarymo schema tirpinimo-nusodinimo sintezės metu, esant statinėmis ir rotacinėms sąlygoms.

IŠVADOS

1. Mg-WH bandiniai su skirtingu magnio kiekiu buvo susintetinti iš brušito tirpinimo-nusodinimo metodu. Nustatyta, kad susintetintos medžiagos cheminė sudėtis, morfologija priklauso nuo Ca/Mg molinio santykio pradiniame sintezės tirpale. XRD analizė atskleidė, kad produktuose, kurių Ca/Mg santykis svyruoja nuo 12 iki 4, antrinių fazių nėra. Cheminė sudėtis ir morfologija buvo kontroliuojami pradinio sintezės tirpalo Ca/Mg santykiu. Padidinus Ca/Mg santykį arba sumažinus magnio kiekį, gardelės parametrai buvo didesni. SEM nuotraukos atskleidė paviršiaus morfologijos priklausomybę nuo magnio kiekio struktūroje, o TEM analizė parodė dalelių dydžio ir formos skirtumus atsižvelgiant į magnio kiekį.
2. Grynas Mg-WH mėginys susintetintas iš gipso miltelių tirpinimo-nusodinimo metodu esant 80 °C temperatūrai statinėmis ir rotacinėmis sąlygomis, pradžioje susidarant tarpiniams sintezės produktams. FT-IR spektrai ankstyvuosiuose sintezės etapuose atskleidė sulfato, fosfato ir vandenilio fosfato grupių tarpiniuose reakcijos junginiuose buvimą, kol galiausiai po 12 val. sintezės ėmė vyrauti Mg-WH fazei būdingos juostos. 12 val. ir 24 val. bandinių Rietveldo struktūros patikslinimas atskleidė nedidelius gardelės parametrų, magnio užimtumo ir gardelės tūrio pokyčius, tačiau sintezės sąlygos (statinės ir rotacinės) turėjo didesnę įtaką struktūriniams parametrams, taip pat Mg-WH bandinių kristalitų dydžiui ir kristališkumui. Gauti rezultatai rodo reakcijos laiko ir sintezės sąlygų įtaką Mg-WH fazės formavimuisi, jos sudėčiai, struktūriniams ir mikrostruktūriniams parametrams.

REFERENCES

[1] E.A.B. Hughes, T.E. Robinson, D.B. Bassett, S.C. Cox, L.M. Grover, Critical and diverse roles of phosphates in human bone formation, J Mater Chem B 7 (2019) 7460–7470. https://doi.org/10.1039/c9tb02011j.

[2] M.J. Yaszemski, R.G. Payne, W.C. Hayes, R. Langer, A.G. Mikos, Evolution of bone transplantation: molecular, cellular and tissue strategies to engineer human bone, Biomaterials 17 (1996) 175–185. https://doi.org/https://doi.org/10.1016/0142-9612(96)85762-0.

[3] M. Langer, A. Pacureanu, H. Suhonen, Q. Grimal, P. Cloetens, F. Peyrin, X-Ray Phase Nanotomography Resolves the 3D Human Bone Ultrastructure, PLoS One 7 (2012). https://doi.org/10.1371/journal.pone.0035691.

[4] H.Y. Lin, Y.K. Huang, P.Y. Hsu, W.H. Tuan, M. Naito, Sintering of degradable bone substitutes at room temperature, Ceram Int 47 (2021) 21714–21720. https://doi.org/10.1016/j.ceramint.2021.04.185.

[5] S. Von Euw, Y. Wang, G. Laurent, C. Drouet, F. Babonneau, N. Nassif, T. Azaïs, Bone mineral: new insights into its chemical composition, Sci Rep 9 (2019). https://doi.org/10.1038/s41598-019-44620-6.

[6] C. Gao, S. Peng, P. Feng, C. Shuai, Bone biomaterials and interactions with stem cells, Bone Res 5 (2017). https://doi.org/10.1038/boneres.2017.59.

[7] H. Qu, Additive manufacturing for bone tissue engineering scaffolds, Mater Today Commun 24 (2020). https://doi.org/10.1016/j.mtcomm.2020.101024.

[8] X. Liu, Y. Miao, H. Liang, J. Diao, L. Hao, Z. Shi, N. Zhao, Y. Wang, 3D-printed bioactive ceramic scaffolds with biomimetic micro/nano-HAp surfaces mediated cell fate and promoted bone augmentation of the bone–implant interface in vivo, Bioact Mater 12 (2022) 120–132. https://doi.org/10.1016/j.bioactmat.2021.10.016.

[9] M. Bohner, B.L.G. Santoni, N. Döbelin, β-tricalcium phosphate for bone substitution: Synthesis and properties, Acta Biomater 113 (2020) 23–41. https://doi.org/10.1016/j.actbio.2020.06.022.

[10] M.F. Pittenger, C.L. Kerr, Stem cells, in: Tissue Engineering, Third Edition, Elsevier, 2022: pp. 13–69. https://doi.org/10.1016/B978-0-12-824459-3.00002-0.

[11] K.M. Pawelec, A.A. White, S.M. Best, Properties and characterization of bone repair materials, in: Bone Repair Biomaterials: Regeneration and Clinical Applications, Second Edition, Elsevier, 2018: pp. 65–102. https://doi.org/10.1016/B978-0-08-102451-5.00004-4.

[12] D. Damm, K. Kostka, C. Weingärtner, J.T. Wagner, L. Rojas-Sánchez, S. Gensberger-Reigl, V. Sokolova, K. Überla, M. Epple, V. Temchura, Covalent coupling of HIV-1 glycoprotein trimers to biodegradable calcium phosphate nanoparticles via genetically encoded aldehyde-tags, Acta Biomater 140 (2022) 586–600. https://doi.org/10.1016/j.actbio.2021.12.022.

[13] D. Huang, B. He, P. Mi, Calcium phosphate nanocarriers for drug delivery to tumors: Imaging, therapy and theranostics, Biomater Sci 7 (2019) 3942–3960. https://doi.org/10.1039/c9bm00831d.

[14] S. Diallo-Garcia, D. Laurencin, J.M. Krafft, S. Casale, M.E. Smith, H. Lauron-Pernot, G. Costentin, Influence of magnesium substitution on the basic properties of hydroxyapatites, Journal of Physical Chemistry C 115 (2011) 24317–24327. https://doi.org/10.1021/jp209316k.

[15] H. Urch, M. Vallet-Regi, L. Ruiz, J.M. Gonzalez-Calbet, M. Epple, Calcium phosphate nanoparticles with adjustable dispersability and crystallinity, J Mater Chem 19 (2009) 2166–2171. https://doi.org/10.1039/b810026h.

[16] K. Ishikawa, E. Garskaite, A. Kareiva, Sol–gel synthesis of calcium phosphate-based biomaterials—A review of environmentally benign, simple, and effective synthesis routes, J Solgel Sci Technol 94 (2020) 551–572. https://doi.org/10.1007/s10971-020-05245-8.

[17] Q. Li, C. Feng, Q. Cao, W. Wang, Z. Ma, Y. Wu, T. He, Y. Jing, W. Tan, T. Liao, J. Xing, X. Li, Y. Wang, Y. Xiao, X. Zhu, X. Zhang, Strategies of strengthening mechanical properties in the osteoinductive calcium phosphate bioceramics, Regen Biomater 10 (2023). https://doi.org/10.1093/rb/rbad013.

[18] K. Ishikawa, Y. Miyamoto, A. Tsuchiya, K. Hayashi, K. Tsuru, G. Ohe, Physical and histological comparison of

hydroxyapatite, carbonate apatite, and β-tricalcium phosphate bone substitutes, Materials 11 (2018). https://doi.org/10.3390/ma11101993.

[19] A. Kizalaite, V. Klimavicius, V. Balevicius, G. Niaura, A.N. Salak, J.C. Yang, S.H. Cho, T. Goto, T. Sekino, A. Zarkov, Dissolution-precipitation synthesis and thermal stability of magnesium whitlockite, CrystEngComm 25 (2023) 4370–4379. https://doi.org/10.1039/d3ce00602f.

[20] J.Di. Pasteris, A mineralogical view of apatitic biomaterials, American Mineralogist 101 (2016) 2594–2610. https://doi.org/10.2138/am-2016-5732.

[21] H. Nagai, M. Kobayashi-Fujioka, K. Fujisawa, G. Ohe, N. Takamaru, K. Hara, D. Uchida, T. Tamatani, K. Ishikawa, Y. Miyamoto, Effects of low crystalline carbonate apatite on proliferation and osteoblastic differentiation of human bone marrow cells, J Mater Sci Mater Med 26 (2015). https://doi.org/10.1007/s10856-015-5431-5.

[22] K. Ishikawa, Bone substitute fabrication based on dissolution-precipitation reactions, Materials 3 (2010) 1138–1155. https://doi.org/10.3390/ma3021138.

[23] I. Grigoraviciute-Puroniene, Y. Tanaka, V. Vegelyte, Y. Nishimoto, K. Ishikawa, A. Kareiva, A novel synthetic approach to low-crystallinity calcium deficient hydroxyapatite, Ceram Int 45 (2019) 15620–15623. https://doi.org/10.1016/j.ceramint.2019.05.072.

[24] A. Kizalaite, I. Grigoraviciute-Puroniene, D.R.C. Asuigui, S.L. Stoll, S.H. Cho, T. Sekino, A. Kareiva, A. Zarkov, Dissolution-precipitation synthesis and characterization of zinc whitlockite with variable metal content, ACS Biomater Sci Eng 7 (2021) 3586–3593. https://doi.org/10.1021/acsbiomaterials.1c00335.

[25] F.A. Shah, Magnesium whitlockite – omnipresent in pathological mineralisation of soft tissues but not a significant inorganic constituent of bone, Acta Biomater 125 (2021) 72–82. https://doi.org/10.1016/j.actbio.2021.02.021.

[26] M. Wang, J. Yao, S. Shen, C. Heng, Y. Zhang, T. Yang, X. Zheng, A scaffold with zinc-whitlockite nanoparticles accelerates bone reconstruction by promoting bone differentiation and angiogenesis, Nano Res 16 (2023) 757–770. https://doi.org/10.1007/s12274-022-4644-4.

[27] K. Bavya Devi, V. Lalzawmliana, M. Saidivya, V. Kumar, M. Roy, S. Kumar Nandi, Magnesium Phosphate Bioceramics for Bone Tissue Engineering, Chemical Record 22 (2022). https://doi.org/10.1002/tcr.202200136.

[28] H.D. Kim, H.L. Jang, H.Y. Ahn, H.K. Lee, J. Park, E. seo Lee, E.A. Lee, Y.H. Jeong, D.G. Kim, K.T. Nam, N.S. Hwang, Biomimetic whitlockite inorganic nanoparticles-mediated in situ remodeling and rapid bone regeneration, Biomaterials 112 (2017) 31–43. https://doi.org/10.1016/j.biomaterials.2016.10.009.

[29] L. Stipniece, K. Salma-Ancane, N. Borodajenko, M. Sokolova, D. Jakovlevs, L. Berzina-Cimdina, Characterization of Mg-substituted hydroxyapatite synthesized by wet chemical method, Ceram Int 40 (2014) 3261–3267. https://doi.org/10.1016/j.ceramint.2013.09.110.

[30] G.-C. Li, P. Wang, C.-B. Liu, Hydrothermal synthesis of whitlockite, JOURNAL OF INORGANIC MATERIALS-BEIJING- 32 (2017) 1128–1132.

[31] C. Qi, F. Chen, J. Wu, Y.J. Zhu, C.N. Hao, J.L. Duan, Magnesium whitlockite hollow microspheres: A comparison of microwave-hydrothermal and conventional hydrothermal syntheses using fructose 1,6-bisphosphate, and application in protein adsorption, RSC Adv 6 (2016) 33393–33402. https://doi.org/10.1039/c6ra00775a.

[32] A. Kizalaite, V. Klimavicius, J. Versockiene, E. Lastauskiene, T. Murauskas, R. Skaudzius, T. Yokoi, M. Kawashita, T. Goto, T. Sekino, A. Zarkov, Peculiarities of the formation, structural and morphological properties of zinc whitlockite (Ca18Zn2(HPO4)2(PO4)12) synthesized via a phase transformation process under hydrothermal conditions, CrystEngComm 24 (2022) 5068–5079. https://doi.org/10.1039/d2ce00497f.

[33] P. Melnikov, D.M. de Albuquerque, T.A. Naves, L.C.S. de Oliveira, Synthesis and characterization of zinc-containing whitlockite Ca10Zn10H2(PO4)14 for orthopedic applications, Mater Lett 231 (2018) 198–200. https://doi.org/10.1016/j.matlet.2018.08.051.

[34] H.L. Jang, H.K. Lee, K. Jin, H.Y. Ahn, H.E. Lee, K.T. Nam, Phase transformation from hydroxyapatite to the secondary

bone mineral, whitlockite, J Mater Chem B 3 (2015) 1342–1349. https://doi.org/10.1039/c4tb01793e.

[35] S. Batool, U. Liaqat, B. Babar, Z. Hussain, Bone whitlockite: synthesis, applications, and future prospects, Journal of the Korean Ceramic Society 58 (2021) 530–547. https://doi.org/10.1007/s43207-021-00120-w.

[36] C. Wang, K.J. Jeong, H.J. Park, M. Lee, S.C. Ryu, D.Y. Hwang, K.H. Nam, I.H. Han, J. Lee, Synthesis and formation mechanism of bone mineral, whitlockite nanocrystals in tri-solvent system, J Colloid Interface Sci 569 (2020) 1–11. https://doi.org/10.1016/j.jcis.2020.02.072.

[37] A.C. Tas, Transformation of Brushite (CaHPO4·2H2O) to Whitlockite (Ca9Mg(HPO4)(PO4)6) or Other CaPs in Physiologically Relevant Solutions, Journal of the American Ceramic Society 99 (2016) 1200–1206. https://doi.org/10.1111/jace.14069.

[38] Y. Liu, D. Luo, T. Wang, Hierarchical Structures of Bone and Bioinspired Bone Tissue Engineering, (2016). https://doi.org/10.1002/smll.201200042.

[39] R. Karpiński, Ł. Jaworski, P. Czubacka, CC-BY 4.0) THE STRUCTURAL AND MECHANICAL PROPERTIES OF THE BONE, 2017. http://jteme.pl.

[40] J. Dj, B. Baha, J. Tadros, Bone structure: from cortical to calcium, n.d. https://nursinglecture.com/histology-of-bone/with.

[41] J. Jeong, J.H. Kim, J.H. Shim, N.S. Hwang, C.Y. Heo, Bioactive calcium phosphate materials and applications in bone regeneration, Biomater Res 23 (2019). https://doi.org/10.1186/s40824-018-0149-3.

[42] S. V. Dorozhkin, M. Epple, Biological and medical significance of calcium phosphates, Angewandte Chemie - International Edition 41 (2002) 3130–3146. https://doi.org/10.1002/1521-3773(20020902)41:17<3130::AID-ANIE3130>3.0.CO;2-1.

[43] K. Ishikawa, K. Hayashi, Carbonate apatite artificial bone, Sci Technol Adv Mater 22 (2021) 683–694. https://doi.org/10.1080/14686996.2021.1947120.

[44] R.Zapanta. LeGeros, Calcium phosphates in oral biology and medicine, Karger, 1991.

[45] J.C. Elliott, Calcium Phosphate Biominerals, Rev Mineral Geochem 48 (2002) 427–453. https://doi.org/10.2138/rmg.2002.48.11.

[46] M. Razavi, M.H. Fathi, M. Meratian, Fabrication and characterization of magnesium–fluorapatite nanocomposite for biomedical applications, Mater Charact 61 (2010) 1363–1370. https://doi.org/https://doi.org/10.1016/j.matchar.2010.09.008.

[47] A. Talal, S.K. Hamid, M. Khan, A.S. Khan, 1 - Structure of biological apatite: bone and tooth, in: A.S. Khan, A.A. Chaudhry (Eds.), Handbook of Ionic Substituted Hydroxyapatites, Woodhead Publishing, 2020: pp. 1–19. https://doi.org/https://doi.org/10.1016/B978-0-08-102834-6.00001-X.

[48] Adler C.P, Bones and Bone Tissue, 2000.

[49] D.J. Hadjidakis, I.I. Androulakis, Bone remodeling, in: Ann N Y Acad Sci, Blackwell Publishing Inc., 2006: pp. 385–396. https://doi.org/10.1196/annals.1365.035.

[50] A.M. Brokesh, A.K. Gaharwar, Inorganic Biomaterials for Regenerative Medicine, ACS Appl Mater Interfaces 12 (2020) 5319–5344. https://doi.org/10.1021/acsami.9b17801.

[51] A.R. Toibah, I. Sopyan, M. Hamdi, S. Ramesh, Development of magnesium-doped biphasic calcium phosphatethrough sol-gel method, in: 4th Kuala Lumpur International Conference on Biomedical Engineering 2008: BIOMED 2008 25–28 June 2008 Kuala Lumpur, Malaysia, Springer, 2008: pp. 314–317.

[52] S.M. Naga, A.M. Hassan, M. Awaad, A. Killinger, R. Gadow, A. Bernstein, M. Sayed, Forsterite/nano-biogenic hydroxyapatite composites for biomedical applications, Journal of Asian Ceramic Societies 8 (2020) 373–386. https://doi.org/10.1080/21870764.2020.1743416.

[53] M. Nabiyouni, T. Brückner, H. Zhou, U. Gbureck, S.B. Bhaduri, Magnesium-based bioceramics in orthopedic applications, Acta Biomater 66 (2018) 23–43. https://doi.org/10.1016/j.actbio.2017.11.033.

[54] S. Yoshizawa, A. Brown, A. Barchowsky, C. Sfeir, Magnesium ion stimulation of bone marrow stromal cells enhances osteogenic activity, simulating the effect of magnesium alloy degradation, Acta Biomater 10 (2014) 2834–2842. https://doi.org/10.1016/j.actbio.2014.02.002.

[55] M. Shahrezaee, M. Raz, S. Shishehbor, F. Moztarzadeh, F. Baghbani, A. Sadeghi, K. Bajelani, F. Tondnevis, Synthesis of Magnesium Doped Amorphous Calcium Phosphate as a Bioceramic for Biomedical Application: In Vitro Study, Silicon 10 (2018) 1171–1179. https://doi.org/10.1007/s12633-017-9589-y.

[56] S. Kannan, A.F. Lemos, J.H.G. Rocha, J.M.F. Ferreira, Characterization and mechanical performance of the Mg-stabilized β-Ca3(PO4)2 prepared from Mg-substituted Ca-deficient apatite, Journal of the American Ceramic Society 89 (2006) 2757–2761. https://doi.org/10.1111/j.1551-2916.2006.01158.x.

[57] H.M. Frost, Skeletal structural adaptations to mechanical usage (SATMU): 2. Redefining Wolff's law: the remodeling problem, Anat Rec 226 (1990) 414–422.

[58] W. Liang, X. Wu, Y. Dong, X. Chen, P. Zhou, F. Xu, Mechanical stimuli-mediated modulation of bone cell function—implications for bone remodeling and angiogenesis, Cell Tissue Res 386 (2021) 445–454. https://doi.org/10.1007/s00441-021-03532-6.

[59] M.R. Senra, M. de F. Vieira Marques, Synthetic polymeric materials for bone replacement, Journal of Composites Science 4 (2020). https://doi.org/10.3390/jcs4040191.

[60] C. Shi, Z. Yuan, F. Han, C. Zhu, B. Li, Polymeric biomaterials for bone regeneration, Ann Jt 1 (2016) 27–27. https://doi.org/10.21037/aoj.2016.11.02.

[61] M.P. Lutolf, J.L. Lauer-Fields, H.G. Schmoekel, A.T. Metters, F.E. Weber, G.B. Fields, J.A. Hubbell, Synthetic matrix metalloproteinase-sensitive hydrogels for the conduction of tissue regeneration: Engineering cell-invasion characteristics, 2003. www.pnas.orgcgidoi10.1073pnas.0737381100.

[62] M.M. Stevens, H.F. Qanadilo, R. Langer, V.P. Shastri, A rapid-curing alginate gel system: Utility in periosteum-derived cartilage tissue engineering, Biomaterials 25 (2004) 887–894. https://doi.org/10.1016/j.biomaterials.2003.07.002.

[63] B.G. Elmegreen, Dark matter in galactic collisional debris, Science (1979) 316 (2007) 1132–1133. https://doi.org/10.1126/science.1143506.

[64] M. Stevens, Biomaterials for Bone Tissue Engineering, Materials Today - MATER TODAY 11 (2008) 18–25. https://doi.org/10.1016/S1369-7021(08)70086-5.

[65] V. Liu Tsang, S.N. Bhatia, Three-dimensional tissue fabrication, Adv Drug Deliv Rev 56 (2004) 1635–1647. https://doi.org/10.1016/j.addr.2004.05.001.

[66] W.G. Koh, A. Revzin, M. V. Pishko, Poly(ethylene glycol) hydrogel microstructures encapsulating living cells, Langmuir 18 (2002) 2459–2462. https://doi.org/10.1021/la0115740.

[67] H. Zhou, J.G. Lawrence, S.B. Bhaduri, Fabrication aspects of PLA-CaP/PLGA-CaP composites for orthopedic applications: A review, Acta Biomater 8 (2012) 1999–2016. https://doi.org/https://doi.org/10.1016/j.actbio.2012.01.031.

[68] A. Salama, Recent progress in preparation and applications of chitosan/calcium phosphate composite materials, Int J Biol Macromol 178 (2021) 240–252. https://doi.org/10.1016/j.ijbiomac.2021.02.143.

[69] C.J. Pérez, P. Eisenberg, C. Bernal, E. Pérez, Mechanical evaluation of polylactic acid (PLA) based composites reinforced with different calcium phosphates, Mater Res Express 5 (2018). https://doi.org/10.1088/2053-1591/aadb5b.

[70] E. Garskaite, L. Alinauskas, M. Drienovsky, J. Krajcovic, R. Cicka, M. Palcut, L. Jonusauskas, M. Malinauskas, Z. Stankeviciute, A. Kareiva, Fabrication of a composite of nanocrystalline carbonated hydroxyapatite (cHAP) with polylactic acid (PLA) and its surface topographical structuring with direct laser writing (DLW), RSC Adv 6 (2016) 72733–72743. https://doi.org/10.1039/c6ra11679e.

[71] M. Furko, K. Balázsi, C. Balázsi, Calcium Phosphate Loaded Biopolymer Composites—A Comprehensive Review on the Most Recent Progress and Promising Trends, Coatings 13 (2023). https://doi.org/10.3390/coatings13020360.

[72] R. O'Neill, H.O. McCarthy, E.B. Montufar, M.P. Ginebra, D.I. Wilson, A. Lennon, N. Dunne, Critical review: Injectability of calcium phosphate pastes and cements, Acta Biomater 50 (2017) 1–19. https://doi.org/10.1016/j.actbio.2016.11.019.

[73] W. Wang, K.W.K. Yeung, Bone grafts and biomaterials substitutes for bone defect repair: A review, Bioact Mater 2 (2017) 224–247. https://doi.org/10.1016/j.bioactmat.2017.05.007.

[74] W. Habraken, P. Habibovic, M. Epple, M. Bohner, Calcium phosphates in biomedical applications: Materials for the future?, Materials Today 19 (2016) 69–87. https://doi.org/10.1016/j.mattod.2015.10.008.
[75] Bioceramics global report, (n.d.).
[76] Mg_whitlockite, (n.d.).
[77] S.K. Ahsan, Metabolism of magnesium in health and disease., J Indian Med Assoc 95 (1997) 507–510.
[78] J.P. Berry, P. Galle, P. Henoc, G. Lagrue, Crystalloid nature of mineral deposits in Bowman's capsule of the human glomerulus. Study by X-ray microanalysis and electron microdiffraction., Pathol Biol (Paris) 25 (1977) 37–41.
[79] J. Jeong, J.H. Kim, J.H. Shim, N.S. Hwang, C.Y. Heo, Bioactive calcium phosphate materials and applications in bone regeneration, Biomater Res 23 (2019) 4. https://doi.org/10.1186/s40824-018-0149-3.
[80] N. Eliaz, N. Metoki, Calcium phosphate bioceramics: A review of their history, structure, properties, coating technologies and biomedical applications, Materials 10 (2017). https://doi.org/10.3390/ma10040334.
[81] R. Karalkeviciene, E. Raudonyte-Svirbutaviciene, A. Zarkov, J.C. Yang, A.I. Popov, A. Kareiva, Solvothermal Synthesis of Calcium Hydroxyapatite via Hydrolysis of Alpha-Tricalcium Phosphate in the Presence of Different Organic Additives, Crystals (Basel) 13 (2023). https://doi.org/10.3390/cryst13020265.
[82] I. Grigoraviciute-Puroniene, K. Tsuru, E. Garskaite, Z. Stankeviciute, A. Beganskiene, K. Ishikawa, A. Kareiva, A novel wet polymeric precipitation synthesis method for monophasic β-TCP, Advanced Powder Technology 28 (2017) 2325–2331. https://doi.org/10.1016/j.apt.2017.06.014.
[83] H.R. Reis, A. Gilsonnkhangg, Advances in Experimental Medicine and Biology 1250 Biomimicked Biomaterials Advances in Tissue Engineering and Regenerative Medicine, n.d. http://www.springer.com/series/5584.
[84] O. Suzuki, Y. Shiwaku, R. Hamai, Octacalcium phosphate bone substitute materials: Comparison between properties of biomaterials and other calcium phosphate materials, Dent Mater J 39 (2020) 187–199. https://doi.org/10.4012/dmj.2020-001.

[85] S. V. Dorozhkin, Synthetic amorphous calcium phosphates (ACPs): Preparation, structure, properties, and biomedical applications, Biomater Sci 9 (2021) 7748–7798. https://doi.org/10.1039/d1bm01239h.

[86] I. Lodoso-Torrecilla, J.J.J.P. van den Beucken, J.A. Jansen, Calcium phosphate cements: Optimization toward biodegradability, Acta Biomater 119 (2021) 1–12. https://doi.org/10.1016/j.actbio.2020.10.013.

[87] Y. Yang, H. Wang, H. Yang, Y. Zhao, J. Guo, X. Yin, T. Ma, X. Liu, L. Li, Magnesium-Based Whitlockite Bone Mineral Promotes Neural and Osteogenic Activities, ACS Biomater Sci Eng 6 (2020) 5785–5796. https://doi.org/10.1021/acsbiomaterials.0c00852.

[88] D. Zeng, L. Xia, W. Zhang, H. Huang, B. Wei, Q. Huang, J. Wei, C. Liu, X. Jiang, Maxillary Sinus Floor Elevation Using a Tissue-Engineered Bone with Calcium-Magnesium Phosphate Cement and Bone Marrow Stromal Cells in Rabbits, Tissue Eng Part A 18 (2011) 870–881. https://doi.org/10.1089/ten.tea.2011.0379.

[89] H.L. Jang, K. Jin, J. Lee, Y. Kim, S.H. Nahm, K.S. Hong, K.T. Nam, Revisiting whitlockite, the second most abundant biomineral in bone: Nanocrystal synthesis in physiologically relevant conditions and biocompatibility evaluation, ACS Nano 8 (2014) 634–641. https://doi.org/10.1021/nn405246h.

[90] F. Capitelli, F. Bosi, S.C. Capelli, F. Radica, G. Della Ventura, Neutron and xrd single-crystal diffraction study and vibrational properties of whitlockite, the natural counterpart of synthetic tricalcium phosphate, Crystals (Basel) 11 (2021) 1–19. https://doi.org/10.3390/cryst11030225.

[91] V. Campana, G. Milano, E. Pagano, M. Barba, C. Cicione, G. Salonna, W. Lattanzi, G. Logroscino, Bone substitutes in orthopaedic surgery: from basic science to clinical practice, J Mater Sci Mater Med 25 (2014) 2445–2461. https://doi.org/10.1007/s10856-014-5240-2.

[92] S. V. Dorozhkin, Calcium orthophosphate-based biocomposites and hybrid biomaterials, in: J Mater Sci, 2009: pp. 2343–2387. https://doi.org/10.1007/s10853-008-3124-x.

[93] Y.Z. Jin, G. Bin Zheng, H.L. Jang, K.M. Lee, J.H. Lee, Whitlockite Promotes Bone Healing in Rabbit Ilium Defect Model, J Med Biol Eng 39 (2019) 944–951. https://doi.org/10.1007/s40846-019-00471-0.

[94] W.B. Lee, C. Wang, J.H. Lee, K.J. Jeong, Y.S. Jang, J.Y. Park, M.H. Ryu, U.K. Kim, J. Lee, D.S. Hwang, Whitlockite Granules on Bone Regeneration in Defect of Rat Calvaria, ACS Appl Bio Mater 3 (2020) 7762–7768. https://doi.org/10.1021/acsabm.0c00960.

[95] H.D. Kim, H.L. Jang, H.Y. Ahn, H.K. Lee, J. Park, E. seo Lee, E.A. Lee, Y.H. Jeong, D.G. Kim, K.T. Nam, N.S. Hwang, Biomimetic whitlockite inorganic nanoparticles-mediated in situ remodeling and rapid bone regeneration, Biomaterials 112 (2017) 31–43. https://doi.org/10.1016/j.biomaterials.2016.10.009.

[96] X. Lin, Fabrication of calcium carbonate monolith by carbonation of calcium hydroxide compact, Arch BioCeram Res 3 (2003) 83–88.

[97] K. Ishikawa, S. Matsuya, X. Lin, Z. Lei, T. Yuasa, Y. Miyamoto, Fabrication of low crystalline B-type carbonate apatite block from low crystalline calcite block, n.d.

[98] H. Wakae, A. Takeuchi, K. Udoh, S. Matsuya, M.L. Munar, R.Z. LeGeros, A. Nakasima, K. Ishikawa, Fabrication of macroporous carbonate apatite foam by hydrothermal conversion of α-tricalcium phosphate in carbonate solutions, J Biomed Mater Res A 87 (2008) 957–963. https://doi.org/10.1002/jbm.a.31620.

[99] X. Lin, S. Matsuya, M. Nakagawa, Y. Terada, K. Ishikawa, Effect of molding pressure on fabrication of low-crystalline calcite block, J Mater Sci Mater Med 19 (2008) 479–484. https://doi.org/10.1007/s10856-006-0028-7.

[100] K. Fujisawa, K. Akita, N. Fukuda, K. Kamada, T. Kudoh, G. Ohe, T. Mano, K. Tsuru, K. Ishikawa, Y. Miyamoto, Compositional and histological comparison of carbonate apatite fabricated by dissolution–precipitation reaction and Bio-Oss®, J Mater Sci Mater Med 29 (2018). https://doi.org/10.1007/s10856-018-6129-2.

[101] Y. Sugiura, M.L. Munar, K. Ishikawa, Fabrication of octacalcium phosphate foam through phase conversion and its histological evaluation, Mater Lett 212 (2018) 28–31. https://doi.org/10.1016/j.matlet.2017.10.051.

[102] V.K. Kaliannagounder, N.P.M.J. Raj, A.R. Unnithan, J. Park, S.S. Park, S.J. Kim, C.H. Park, C.S. Kim, A.R.K. Sasikala, Remotely controlled self-powering electrical stimulators for

osteogenic differentiation using bone inspired bioactive piezoelectric whitlockite nanoparticles, Nano Energy 85 (2021). https://doi.org/10.1016/j.nanoen.2021.105901.

[103] S. Batool, Z. Hussain, U. Liaqat, M. Sohail, Solid-state synthesis and process optimization of bone whitlockite, Ceram Int 48 (2022) 13850–13854. https://doi.org/10.1016/j.ceramint.2022.01.267.

[104] D. Zhou, C. Qi, Y.X. Chen, Y.J. Zhu, T.W. Sun, F. Chen, C.Q. Zhang, Comparative study of porous hydroxyapatite/chitosan and whitlockite/chitosan scaffolds for bone regeneration in calvarial defects, Int J Nanomedicine 12 (2017) 2673–2687. https://doi.org/10.2147/IJN.S131251.

[105] S.Y. Stefanovich, B.I. Lazoryak, A.M. Antipin, A.S. Volkov, A.I. Evdokimov, O.A. Gurbanova, O. V. Dimitrova, D. V. Deyneko, Crystal structures of biocompatible Mg-, Zn-, and Co-whitlockites synthesized via one-step hydrothermal reaction, Z Kristallogr Cryst Mater 238 (2023) 301–309. https://doi.org/10.1515/zkri-2023-0016.

[106] T. Roisnel, J. Rodríguez-Carvajal, J. Gonzalez-Platas, WinPLOTR, a graphic tool for powder diffraction, Laboratoire Léon Brillouin (CEA/CNRS), CEA-Saclay 91191 (2001).

[107] J. Rodr\'{\i}quez-Carvajal, T. Roisnel, Line Broadening Analysis Using FullProf*: Determination of Microstructural Properties, in: European Powder Diffraction EPDIC 8, Trans Tech Publications Ltd, 2004: pp. 123–126. https://doi.org/10.4028/www.scientific.net/MSF.443-444.123.

[108] H. Cheng, R. Chabok, X. Guan, A. Chawla, Y. Li, A. Khademhosseini, H.L. Jang, Synergistic interplay between the two major bone minerals, hydroxyapatite and whitlockite nanoparticles, for osteogenic differentiation of mesenchymal stem cells, Acta Biomater 69 (2018) 342–351. https://doi.org/10.1016/j.actbio.2018.01.016.

[109] R.D. Shannon, Revised effective ionic radii and systematic studies of interatomic distances in halides and chalcogenides, Acta Crystallographica Section A 32 (1976) 751–767. https://doi.org/10.1107/S0567739476001551.

[110] I. UIIah, L. Cao, W. Cui, Q. Xu, R. Yang, K. lai Tang, X. Zhang, Stereolithography printing of bone scaffolds using biofunctional calcium phosphate nanoparticles, J Mater Sci Technol 88 (2021) 99–108. https://doi.org/10.1016/j.jmst.2021.01.062.

[111] L. Vegard, Die konstitution der mischkristalle und die raumfüllung der atome, Zeitschrift Für Physik 5 (1921) 17–26.
[112] R. Jenkins, R.L. Snyder, Introduction to X-ray Powder Diffractometry (Volume 138)., Wiley Online Library, 1996.
[113] E. Garskaite, K.A. Gross, S.W. Yang, T.C.K. Yang, J.C. Yang, A. Kareiva, Effect of processing conditions on the crystallinity and structure of carbonated calcium hydroxyapatite (CHAp), CrystEngComm 16 (2014) 3950–3959. https://doi.org/10.1039/c4ce00119b.
[114] H.L. Jang, G. Bin Zheng, J. Park, H.D. Kim, H.R. Baek, H.K. Lee, K. Lee, H.N. Han, C.K. Lee, N.S. Hwang, J.H. Lee, K.T. Nam, In Vitro and In Vivo Evaluation of Whitlockite Biocompatibility: Comparative Study with Hydroxyapatite and β-Tricalcium Phosphate, Adv Healthc Mater 5 (2016) 128–136. https://doi.org/10.1002/adhm.201400824.
[115] C. Stähli, J. Thüring, L. Galea, S. Tadier, M. Bohner, N. Döbelin, Hydrogen-substituted β-tricalcium phosphate synthesized in organic media, Acta Crystallogr B Struct Sci Cryst Eng Mater 72 (2016) 875–884. https://doi.org/10.1107/S2052520616015675.
[116] Z. Zyman, A. Goncharenko, D. Rokhmistrov, M. Epple, Nanocrystalline calcium-deficient hydroxyapatite prepared by a microwave-assisted solvent-free reaction, Materwiss Werksttech 42 (2011) 154–157. https://doi.org/10.1002/mawe.201100749.
[117] G. Cama, B. Gharibi, M.S. Sait, J.C. Knowles, A. Lagazzo, S. Romeed, L. Di Silvio, S. Deb, A novel method of forming micro- and macroporous monetite cements, J Mater Chem B 1 (2013) 958–969. https://doi.org/10.1039/c2tb00153e.
[118] R.G. Carrodeguas, S. De Aza, α-Tricalcium phosphate: Synthesis, properties and biomedical applications, Acta Biomater 7 (2011) 3536–3546. https://doi.org/https://doi.org/10.1016/j.actbio.2011.06.019.
[119] T. Konishi, S. Watanabe, HYDROTHERMAL TRANSFORMATION OF CALCIUM HYDROGEN PHOSPHATE DIHYDRATE INTO MAGNESIUM WHITLOCKITE, 2021.
[120] Y. Kobayashi, A. Nishikata, T. Tanase, M. Konno, Size Effect on Crystal Structures of Barium Titanate Nanoparticles Prepared by a Sol-Gel Method, 2004.

[121] G. Mestl, B. Herzog, R. Schlögl, H. Knözinger, Mechanically activated MoO3. 1. Particle size, crystallinity, and morphology, Langmuir 11 (1995) 3027–3034.

[122] H. Jensen, J.H. Pedersen, J.E. Jørgensen, J.S. Pedersen, K.D. Joensen, S.B. Iversen, E.G. Søgaard, Determination of size distributions in nanosized powders by TEM, XRD, and SAXS, J Exp Nanosci 1 (2006) 355–373. https://doi.org/10.1080/17458080600752482.

[123] V. Uvarov, I. Popov, Metrological characterization of X-ray diffraction methods at different acquisition geometries for determination of crystallite size in nano-scale materials, Mater Charact 85 (2013) 111–123. https://doi.org/10.1016/j.matchar.2013.09.002.

[124] R. Štulajterová, Ľ. Medvecký, Effect of calcium ions on transformation brushite to hydroxyapatite in aqueous solutions, Colloids Surf A Physicochem Eng Asp 316 (2008) 104–109. https://doi.org/10.1016/j.colsurfa.2007.08.036.

[125] J. Zhang, W. Zhang, L. Wang, In Situ Observation of Dicalcium Phosphate Monohydrate Formation and Phase Transformation, Journal of Physical Chemistry B 126 (2022) 4881–4888. https://doi.org/10.1021/acs.jpcb.2c01627.

[126] R.A. Van Santen, The Ostwald step rule, J Phys Chem 88 (1984) 5768–5769. https://doi.org/10.1021/j150668a002.

[127] A.D. Ter Braake, P.T. Tinnemans, C.M. Shanahan, J.G.J. Hoenderop, J.H.F. De Baaij, Magnesium prevents vascular calcification in vitro by inhibition of hydroxyapatite crystal formation, Sci Rep 8 (2018). https://doi.org/10.1038/s41598-018-20241-3.

[128] T. Konishi, S. Watanabe, COPPER WHITLOCKITE SYNTHESIZED VIA HYDROTHERMAL TRANSFORMATION OF CALCIUM HYDROGEN PHOSPHATE DIHYDRATE, 2022.

[129] Q. Ruan, Y. Zhu, Y. Zeng, H. Qian, J. Xiao, F. Xu, L. Zhang, D. Zhao, Ultrasonic-irradiation-assisted oriented assembly of ordered monetite nanosheets stacking, Journal of Physical Chemistry B 113 (2009) 1100–1106. https://doi.org/10.1021/jp809494f.

[130] H. Shi, F. He, J. Ye, Synthesis and structure of iron- and strontium-substituted octacalcium phosphate: Effects of ionic charge and radius, J Mater Chem B 4 (2016) 1712–1719. https://doi.org/10.1039/c5tb02247a.

[131] C. Calvo, J. Ito, W.K. Sabine, Crystal Structure of Synthetic Mg-Whitlockite, Cal 8Mg,H,(P0, 1974.

[132] A. Afonina, A. Kizalaite, A. Zarkov, A. Drabavicius, T. Goto, T. Sekino, A. Kareiva, I. Grigoraviciute-Puroniene, Synthesis of whitlockite nanopowders with different magnesium content, Ceram Int 48 (2022) 32125–32130. https://doi.org/10.1016/j.ceramint.2022.07.152.

[133] J.P. Zuniga, S.K. Gupta, M. Abdou, Y. Mao, Effect of Molten Salt Synthesis Processing Duration on the Photo- and Radioluminescence of UV-, Visible-, and X-ray-Excitable La2Hf2O7:Eu3+ Nanoparticles, ACS Omega 3 (2018) 7757–7770. https://doi.org/10.1021/acsomega.8b00987.

[134] M. Tomellini, Kinetics of dissolution-precipitation reaction at the surface of small particles: Modelling and application, J Mater Sci 47 (2012) 804–814. https://doi.org/10.1007/s10853-011-5858-0.

[135] C. Zhang, F. Liu, F. Wang, H. Li, F. Zeng, Y. Ma, L. Wang, Crystallization process and nucleation kinetics of Mg2+//SO42-, NO3-H2O system, Water Science and Technology 80 (2019) 950–960. https://doi.org/10.2166/wst.2019.341.

[136] S. Bouhlassa, F. Salhamen, A. Elyahyaoui, Calcium sulphate hydrates formation in aqueous sulpho-phosphoric media containing rare earth impurity beyond 80 °C, Fluid Phase Equilib 423 (2016) 93–100. https://doi.org/10.1016/j.fluid.2016.04.016.

[137] D. Navarro da Rocha, L.R. de O. Cruz, J.B. de Campos, J.L. dos Santos, R.L.S.B. Marçal, D.Q. Mijares, R.M. Barbosa, P.G. Coelho, M.H. Prado da Silva, Bioactivity of strontium-monetite coatings for biomedical applications, Ceram Int 45 (2019) 7568–7579. https://doi.org/10.1016/j.ceramint.2019.01.051.

[138] M.M. Mirković, T.D.L. Pašti, A.M. Došen, M. Čebela, A.A. Rosić, B.Z. Matović, B.M. Babić, Adsorption of malathion on mesoporous monetite obtained by mechanochemical treatment of brushite, RSC Adv 6 (2016) 12219–12225. https://doi.org/10.1039/c5ra27554g.

[139] S. Mirkiani, A.S. Mesgar, Z. Mohammadi, M. Matinfar, Synergetic reinforcement of brushite cements by monetite/apatite whisker-like fibers and carboxymethylcellulose, Materialia (Oxf) 21 (2022). https://doi.org/10.1016/j.mtla.2022.101329.

[140] D. Lee, P.N. Kumta, Chemical synthesis and stabilization of magnesium substituted brushite, Materials Science and Engineering C 30 (2010) 934–943. https://doi.org/10.1016/j.msec.2010.04.007.
[141] S. Mandel, A.C. Tas, Brushite (CaHPO4·2H2O) to octacalcium phosphate (Ca8(HPO4)2(PO4)4·5H2O) transformation in DMEM solutions at 36.5 °C, Materials Science and Engineering C 30 (2010) 245–254. https://doi.org/10.1016/j.msec.2009.10.009.
[142] C. Stähli, J. Thüring, L. Galea, S. Tadier, M. Bohner, N. Döbelin, Hydrogen-substituted β-tricalcium phosphate synthesized in organic media, Acta Crystallographica Section B 72 (2016) 875–884. https://doi.org/10.1107/S2052520616015675.
[143] M.S. Djošić, V.B. Mišković-Stanković, Z.M. Kačarević-Popović, B.M. Jokić, N. Bibić, M. Mitrić, S.K. Milonjić, R. Jančić-Heinemann, J. Stojanović, Electrochemical synthesis of nanosized monetite powder and its electrophoretic deposition on titanium, Colloids Surf A Physicochem Eng Asp 341 (2009) 110–117. https://doi.org/10.1016/j.colsurfa.2009.03.046.
[144] J. Vecstaudza, M. Gasik, J. Locs, Amorphous calcium phosphate materials: Formation, structure and thermal behaviour, J Eur Ceram Soc 39 (2019) 1642–1649. https://doi.org/10.1016/j.jeurceramsoc.2018.11.003.
[145] F. Barrère, C.M. Van Der Valk, R.A.J. Dalmeijer, C.A. Van Blitterswijk, K. De Groot, P. Layrolle, In vitro and in vivo degradation of biomimetic octacalcium phosphate and carbonate apatite coatings on titanium implants, J Biomed Mater Res A 64 (2003) 378–387. https://doi.org/10.1002/jbm.a.10291.
[146] L. Fu, W. Xia, T. Mellgren, M. Moge, H. Engqvist, Preparation of High Percentage <i>α</i>-Calcium Sulfate Hemihydrate via a Hydrothermal Method, J Biomater Nanobiotechnol 08 (2017) 36–49. https://doi.org/10.4236/jbnb.2017.81003.
[147] $ S Jinawath, D. Polchai, M. Yoshimura, Low-temperature, hydrothermal transformation of aragonite to hydroxyapatite, n.d. www.elsevier.com/locate/msec.
[148] T. Sugimoto, Preparation of monodispersed colloidal particles, Adv Colloid Interface Sci 28 (1987) 65–108. https://doi.org/https://doi.org/10.1016/0001-8686(87)80009-X.

AKNOWLEGEMENTS

I would like to thank everyone who has helped me with this work. First, I would like to thank **Prof. habil. Dr. A. Kareiva**, for giving me the opportunity to come and study, and the biggest thank you for giving me the most wonderful supervisor **Assoc. Prof. Dr. Inga Grigoravičiūtė**. For my supervisor, I would like to give a special and most sincere thank you. She has guided and helped me during my scientific work not only in scientific matters, but also with her endless attention and support in difficult situations. It was only thanks to her support and help that I did not give up. I would also like to thank everyone who helped me in this journey.

I would also like to thank my **Parents**, especially my mother, who has helped me immensely in looking after my little daughter so that I could study. Also, to my daughter **Sofija** and my husband **Miroslavas** for their patience, support and dedication.

LIST OF PUBLICATIONS AND ATTENDED CONFERENCES

Publications in Journal

1. Anastasija Afonina, Agne Kizalaite, Aleksej Zarkov, Audrius Drabavicius, Tomoyo Goto, Tohru Sekino, Aivaras Kareiva, Inga Grigoraviciute-Puroniene: „Synthesis of whitlockite nanopowders with different magnesium content“, Ceramics International, Volume 48, Issue 21, 1 November 2022, Pages 32125-32130, https://doi.org/10.1016/j.ceramint.2022.07.152.
2. Anastasija Afonina, Aurimas Dubauskas, Vytautas Klimavicius, Aleksej Zarkov, Aivaras Kareiva, Inga Grigoraviciute ”Phase Transformations During the Dissolution-Precipitation Synthesis of Magnesium Whitlockite Nanopowders from Gypsum”. Ceramics International, Volume 49, Issue 23, Part A, 1 December 2023, Pages 38157-38164, https://doi.org/10.1016/j.ceramint.2023.09.146.

Attended Conferences

1. A. Afonina, G. Antanaitis, I. Grigoraviciute, A. Kareiva. *Low-Temperature Synthesis of Magnesium Whitlockite Nanopowder Under Static and Rotating Conditions*. Chemistry and Chemical Technology 2023 (CCT-2023), Vilnius, Lithuania, 10 March 2023.
2. A. Afonina, I. Grigoraviciute, A. Kareiva. *Investigation of Phase Transformations in the Low Temperature Synthesis of Magnesium Whitlockite*. Functional Inorganic Materials (FIM 2022), Vilnius, Lithuania, 6-8 October 2022.
3. A. Afonina, I. Grigoraviciute-Puroniene, A. Kareiva. *Low-temperature synthesis and characterization of magnesium whitlockite powder*. Advanced materials and technologies, Palanga, Lithuania, 23-27 August 2021.
4. A. Afonina, I. Grigoraviciute-Puroniene, A. Kareiva. *Low-temperature synthesis of carbonated hydroxyapatite*. Chemistry and chemical technology 2021 (CCT-2021), Vilnius, Lithuania, 21 September 2021.
5. A. Afonina, I. Grigoraviciute-Puroniene, A. Kareiva. *Low-Temperature Synthesis of Iron Doped Whitlockite Powders*. Nanostuctured bioceramics materials (NBCM 2020), Vilnius, Lithuania, 1-3 December 2020.

CURICULLUM VITAE

Vardas, pavardė	Anastasija Afonina
Gimimo metai	1989 m.
Gyvenama vieta	Vilnius, Lietuva
El. paštas	anastasija0810@gmail.com
Šeimyninė padėtis	ištekėjusi, dukra

Išsilavinimas:

2017 – dabar	Vilniaus universitetas, Chemijos ir geomokslų fakultetas, Doktorantūros studijos.
2012 – 2014	Vilniaus universitetas, Chemijos fakultetas, Magistro studijos, chemija. Papildoma informacija: studijų specializacija – analizinė chemija.
2008 – 2012	Vilniaus universitetas, Chemijos fakultetas, Bakalauro studijos, chemija. Papildoma informacija: studijų specializacija – analizinė chemija.
1996 – 2008	Vilniaus Karoliniškių gimnazija

Darbo patirtis:

2012 – dabar	Lietuvos teismo ekspertizės centras. Vyriausioji ekspertė, narkotinių ir psichotropinių medžiagų kvalifikacija. Gautos tyrimui medžiagos įvertinimas, mėginių paruošimas tyrimui. Tyrimų atlikimas naudojant dujų chromatografus su masių sprektrometriniais detektoriais, dujų chromatografus su liepsnos jonizaciniais detektoriais, bei skysčių chromatografu su masių spektrometriniu detektoriumi. Atliktų tyrimų rezultatų pateikimas užsakovams.
2011 – 2012	UAB „Kepimo vizija“. Pardavėja

	Darbas su kasos aparatu, kasos knygos pildymas, klientų aptarnavimas, tvarkos priežiūra, prekių išdėliojimas, darbas su kavos aparatu.
2011/09 – 2011/10	FTMC Chemijos institutas Katalizės skyrius. Praktikantė.
Kalbiniai įgūdžiai:	Lietuvių: gimtoji Anglų: B1 lygis. Rusų: kalbėjimas – puikiai, rašyba – puikiai.

NOTES

Vilniaus universiteto leidykla
Saulėtekio al. 9, III rūmai, LT-10222 Vilnius
El. p. info@leidykla.vu.lt, www.leidykla.vu.lt
bookshop.vu.lt, journals.vu.lt
Tiražas 15 egz.